Aus der

Klinik für Orthopädie und Unfallchirurgie

Klinikum der Ludwig-Maximilians-Universität München

Primary Fixation and Bone Density Assessments in Total Shoulder Arthroplasty

Dissertation

zum Erwerb des Doktorgrades der Humanbiologie

an der Medizinischen Fakultät der

Ludwig-Maximilians-Universität München

vorgelegt von

Daniel Ritter

aus

Balingen

2025

Mit Genehmigung der Medizinischen Fakultät der

Ludwig-Maximilians-Universität München

Erstes Gutachten:	*Prof. Dr. Matthias Woiczinski*
Zweites Gutachten:	Prof. Dr. Steffen Peldschus
Drittes Gutachten:	Prof. Dr. Guillaume Landry

Dekan:	Prof. Dr. med. Thomas Gudermann
Tag der mündlichen Prüfung:	26.05.2025

Affidavit

LUDWIG-
MAXIMILIANS-
UNIVERSITÄT
MÜNCHEN

Promotionsbüro
Medizinische Fakultät

Affidavit

Ritter, Daniel

Surname, first name

I hereby declare, that the submitted thesis entitled:

Primary Fixation and Bone Density Assessments in Total Shoulder Arthroplasty

is my own work. I have only used the sources indicated and have not made unauthorised use of services of a third party. Where the work of others has been quoted or reproduced, the source is always given.

I further declare that the dissertation presented here has not been submitted in the same or similar form to any other institution for the purpose of obtaining an academic degree.

Munich, 26.05.2025

place, date

Daniel Ritter

Signature doctoral candidate

Confirmation of congruency

LUDWIG-MAXIMILIANS-UNIVERSITÄT MÜNCHEN

Promotionsbüro
Medizinische Fakultät

Confirmation of congruency between printed and electronic version of the doctoral thesis

Ritter, Daniel

Surname, first name

I hereby declare, that the submitted thesis entitled:

Primary Fixation and Bone Density Assessments in Total Shoulder Arthroplasty

is congruent with the printed version both in content and format.

Munich, 26.05.2025

place, date

Daniel Ritter

Signature doctoral candidate

Table of Contents

Abbreviations

aTSA - Anatomic total shoulder arthroplasty

RSA - Reverse shoulder arthroplasty

CT - Computed tomography

BMD - Bone mineral density

HU - Hounsfield unit

AUC - Area under curve

ROC - Receiver operating characteristic curve

XAI - Explainable artificial intelligence

Publication List

1. Bachmaier S, DiFelice GS, Sonnery-Cottet B, Douoguih WA, Smith PA, Pace LJ, et al. Treatment of Acute Proximal Anterior Cruciate Ligament Tears-Part 1: Gap Formation and Stabilization Potential of Repair Techniques. Orthop J Sports Med 2020;8(1):2325967119897421. doi:10.1177/2325967119897421

2. Bachmaier S, DiFelice GS, Sonnery-Cottet B, Douoguih WA, Smith PA, Pace LJ, et al. Treatment of Acute Proximal Anterior Cruciate Ligament Tears-Part 2: The Role of Internal Bracing on Gap Formation and Stabilization of Repair Techniques. Orthop J Sports Med 2020;8(1):2325967119897423. doi:10.1177/2325967119897423

3. Bachmaier S, Flury M, Lichtenberg S, Schwyzer H-K, Anderl W, Denard PJ, et al. Postpreparation peri-implant humeral bone density and fixation strength vary based on design in stemless reverse shoulder arthroplasty. Seminars in Arthroplasty: JSES 2021;31(4):677-87. doi:10.1053/j.sart.2021.04.005

4. Bachmaier S, Krych AJ, Smith PA, Herbort M, Ritter D, LaPrade RF, et al. Primary Fixation and Cyclic Performance of Single-Stitch All-Inside and Inside-Out Meniscal Devices for Repairing Vertical Longitudinal Meniscal Tears. Am J Sports Med 2022;50(10):2705-13. doi:10.1177/03635465221107086

5. Bachmaier S, Smith PA, Hammoud S, Ritter D, Hauck O, Wijdicks CA. Stabilization and Gap Formation of Adjustable Versus Fixed Primary ACL Repair With Internal Brace: An in Vitro Full-Construct Biomechanical Cadaveric Study. Orthop J Sports Med 2023;11(9):23259671231201462. doi:10.1177/23259671231201462

6. Ritter D, Hachem A-I, Scheibel M, Raiss P, Denard PJ, Campagnoli A, et al. Primary Stability and Bone Contact Loading Evaluation of Suture and Screw based Coracoid Graft Fixation for Anterior Glenoid Bone Loss. The American Journal of Sports Medicine 2023. doi:10.1177/03635465231188976

1. Contribution to Publications I, II, III

- Conceptualization: Formulation or evolution of research goals and aims.
- Data Curation: Management activities to produce metadata, scrub data, and maintain research data (including software code) for initial use and later re-use.
- Formal Analysis: Application of statistical, mathematical, computational, or other formal techniques to analyze or synthesize study data.
- Investigation: Conducting the research and investigation process, specifically performing the experiments, or data/evidence collection.
- Methodology: Development or design of methodology.
- Software: Programming, software development; designing computer programs; implementation of the computer code and supporting algorithms; testing of existing code components.
- Writing – Original Draft: Preparation, creation and presentation of the published work, specifically writing the initial draft, including substantial translation.

2. Introduction

2.1 Shoulder Arthroplasty

Total shoulder arthroplasty has historically shown good results in replacing the glenohumeral joint with a humeral and glenoid component. While osteoarthritis is the most common indication for reconstructing the joint in its anatomic fashion, reverse shoulder arthroplasty is commonly the choice of treatment for indications concerning the rotator cuff and the range of motion of the shoulder joint. By inverting the joint's humeral and glenoid ball-socket architecture, the activation of the rotator cuff and deltoid muscles improve postoperative range of motion and clinical results.[1] Recently, the humeral components in reverse shoulder arthroplasty (RSA) and anatomic total shoulder arthroplasty (aTSA) underwent significant design changes.[2, 3]

2.1.1 Anatomic Total Shoulder Arthroplasty

In an effort to reduce stem-related complications when restoring the function of the glenohumeral joint, humeral components have seen a trend of shortening the stem length. The transition towards short-stem and stemless designs aims to reduce complications associated with intraoperative periprosthetic fracture, proximal humeral bone loss due to stress shielding, and significant bone loss in revision surgery.[4-7] However, bone resorptions still occur from unphysiological proximal humeral bone loading which also depend on the design of the prosthesis. Impacted stemless and short stem designs result in bone resorptions, particularly in the medial calcar region,[7-12] while a cortical supporting design fixed with a hollow screw instead showed bone stock reductions in the greater tuberosity region.[13, 14] The short-term clinical impact of stress shielding is minimal,[8, 13-16] however, long-term effects may affect survival time, clinical outcomes, bone loss in revision cases, and periprosthetic fractures.[17]

While the stemless designs reduce these complications, the fixation of the stemless components may rely more on the bone quality in the metaphysis of the humerus. A poor bone stock with reduced bone mineral density (BMD) is associated with unstable humeral implant fixation and at higher risk for complications in aTSA.[18-20] As humeral components are mainly loaded in a compression state, stemless implants with sufficient primary support are increasingly used in a wider range of bone quality. Nevertheless, large meta-analyses revealed significantly increased complication rates in patients with poorer bone densities. [21-23] As mechanical loading affects the behavior of autologous trabecular and cortical bone, in addition to primary stability measurements, the measurement of bone deformations help to understand humeral implant-bone loading.[24-26] The bone deformations explicitly evaluated in the medial calcar area could demonstrate the differences between implant designs and types and, therefore, to assess deviations compared to the cortical based load transmission known from physiological load transfer patterns in the proximal humerus.[27-29] Biomechanical data of the effect of variable bone densities on the primary stability and the differing load transmissions are lacking but may significantly affect osseointegration and bone resorption in the proximal humerus.[30] Biologic and postoperative factors such as bony ingrowth or polyethylene wear and the respective effects on the implant behavior cannot be investigated in biomechanical and imaging studies. Nevertheless, to understand potential causes for stress shielding and implant micromotion, biomechanical investigations are valuable to analyze the time-zero post-operative implant behavior at the implant-bone interface.

2.1.2 Reverse Shoulder Arthroplasty

The effect of variable bone densities and the use of stemless humeral components in RSA becomes more critical, as shear loads are added to the biomechanical loading situation of the humeral component. [31-33] Nevertheless, the transition to stemless designs is ongoing while stemmed humeral implants show good long-term results with a low humeral loosening rate. Stress shielding and stem-related bone adaptions using these implants remain common complications. Particularly the humeral implant sizing was shown to affect the incidence of stress shielding.[11, 34] While more voluminous humeral implants resulted in significantly increased stress shielding rates, lowering the implant sizes resulted in limited primary stability and subsidence and tilt of the implant postoperatively.[35] Due to the more demanding loading pattern in reverse shoulder arthroplasty, the primary fixation plays a critical role. Primary fixation stability is further affected by poor bone quality, which has additional effects on the choice of treatment and cementation technique.[19, 36-38]

A higher incidence of osteoporosis with 26.2% in RSA patients was shown by Casp et al. which correlates with the higher age in these patients.[19] The osteoporosis rates in shoulder arthroplasty are expected to rise due to the increasing number of older adults undergoing these procedures, highlighting the demand for preoperative identification of patients with a low bone quality.[37, 39]

Additional complications resulting from poor bone quality are known for the glenoid side in shoulder arthroplasty. In fact, implant loosening and acromion stress fractures are associated with poor bone densities, especially in higher degree lateralized and shifted center of rotation of the glenohumeral joint.[4-7, 19] While lateralization improves the clinical outcomes in RSA patients, higher shear loads at the glenoid-implant interface require optimized fixation capabilities. In order to preserve the glenoid bone from extensive reaming, glenoid baseplate augmentations offer eased lateral offsets allowing for the correction of the glenoid inclination and retroversion.[40, 41] Currently bony or metal augmented baseplates are mainly used. The bony augmentation procedure allows for bone preservation or even formation but bone graft and fixation may require a higher bone density.[42] To reduce the influence of variability of the bone density, graft shape and fixation metal augments may be preferrable in case the bone density cannot be assessed preoperatively.

Mainly demographic patient and clinical assessment data are used for the treatment selection and assessment of the risk for complications, even though imaging procedures with unused bone density information are routinely performed for these patients.[43] A preoperative bone assessment therefore may pay off to support the surgeons' decision process, especially with regard to the use of stemless implants, commonly used lateralization in RSA, and an increase of osteoporotic patients. Incorporation of this information into a preoperative planning tool may represent a valuable tool in the clinical surrounding.

2.2 Preoperative Imaging

Preoperative planning with computed tomography (CT) imaging has become a common tool for assessing glenoid and humeral morphology. These CT data may also offer the ability to provide objective measurements of the bone mineral density. [21-23, 44] However, challenges remain in consistently quantifying gray scale information originating from various scanners, defining relevant regions of interest, and objective classification of the patients' bone quality.

2.2.1 CT-based Parameters

In reverse and anatomic total shoulder arthroplasty, the patient's bone density is known to affect the treatment decision and complication rates.[19] Preoperative CT data therefore may offer improved risk stratification to detect patients with potentially poor bone densities. The final bone quality assessment is currently performed intraoperatively by the 'thumb test'. After resection of the humeral head, the surgeon compresses the humeral cancellous bone and assesses if the bone quality is adequate for stemless implant fixation.[45, 46] However, this subjective measure showed poor performance (48% accuracy) in recognizing poor bone quality in shoulder arthroplasty patients.[22] Manual calculation in single CT slices, such as the deltoid tuberosity index and circular metaphyseal measured Hounsfield Unit (HU) densities have been reported to provide value for predicting the ability to place a stemless device or highly lateralized and augmented glenoid baseplates.[21-23, 44, 47]

In case a stemless device is contraindicated, stem sizing poses the subsequent question.[48] As introduced previously, the sizing and implantation of different volumes into the humeral canal allows for the risk analysis for implant subsidence or stress shielding of the bone. Filling ratio calculation of the implant in dependence to the humeral canal result in quantifiable ratios allowing for the assessment of the intended stem size before surgery. Volumetric canal fill calculation showed promising results in predicting stress shielding caused bone resorptions in short and standard stemmed RSA, [34] however the effects on primary fixation were not evaluated in a full construct setting, yet. Additionally, inconsistent HU scales in a clinical setting make multicentric canal segmentations and filling ratio calculations more difficult.

The use of the HU scale from CT scans and two dimensional measurements have demonstrated high variability due to the use of different devices, exposure parameters, differing position of the measurement, and variable mass inside and outside the field of view.[49, 50] Patient-specific calibration of the grayscale values on a bone mineral density scale have been reported to reduce inaccuracies.[51-53] To set a baseline for differing scales of retrospectively gathered CT scans, patient-specific air-muscle-fat calibration helps to reduce outliers and unwanted variability.[51-53] In combination with three-dimensional implantation relevant regions of interest, more informative features could be extracted from clinical preoperative CT scans comparable to imaging studies in non-clinical settings.[32, 54]

2.2.2 Preoperative Classification

The high subjectivity and variability in currently used bone assessment methods depend on differing surgeon’s experience of the minimal force applied and differing bone areas.[21] First studies used objective univariate prediction analyses to assess the classification capability using x-rays and two-dimensional regions of interest as input data.[21] These statistical models performed with moderate-to-good accuracy when predicting poor bone density.[23] Additional to the tuning and training of predictive models, potential for optimization can be found in feature extraction methods. Improving the integrity and quality of the input variables for statistical modelling generally can be achieved by procedures to improve data consistency, for example through previously described patient specific calibration and the use of three-dimensional regions interest.

Predictive models are often used for group classification based on specified input variables. Conventional statistical models can be improved by adapting these models as tailored solutions for the problems to be solved. Generally, these machine learning models require labeled or unlabeled data sets to respectively classify or cluster them into distinct subgroups. A labeled data set allows to train a model using the input parameters marked with the respective ground true labels (Supervised), e.g. treatment decisions. If no data labels are present, the data can be separated into subgroups in multidimensional data space based on specified distance measures, variance, or distributions (Unsupervised).

As no osteoporosis screening is commonly performed in shoulder arthroplasty, the surgeon's decision could represent a potential prediction aim, for example to predict implantation of a stemless humeral implant originally determined by a positive thumb test. As a high subjectivity is hidden in such labels, unsupervised machine learning algorithms using unlabeled data can improve the objectivity of respective predictions. The performance of these predictions is assessed by applying the programmed model independently in training and testing data sets. Supervised models allow for comparison with the ground true label in the data set, while unsupervised models can be assessed regarding intra- and intercluster quality measures. A comparison to conventional statistical methods can deliver additional understanding, if the classification or clustering algorithm works adequately. To support the users of such models the field of explainable artificial intelligence (XAI) focuses on the explainability of predicted decisions. [55, 56] A breakdown of the impact of respective variables on the overall model or a demonstration of a single prediction and respective contribution of the variables help to reduce the black box characteristics of these applications. Additionally, these insights provide information of the performance of the model and can be used for another optimization iteration. Trained and tested models including an explanation of the decision could provide preoperative suggestions to surgeons treating patients with potentially poor bone quality.

2.3 Research Questions and Aims

This work focuses on the investigation of preoperative imaging and primary stability in anatomic and reverse total shoulder arthroplasty and suggests opportunistic applications in routinely performed imaging procedures. The utility of preoperative CT imaging to assess the bone density and morphology in aTSA and RSA cohorts and the effects on primary stability and bone loading were analyzed in five studies (Figure 1). Applying these approaches in a preoperative planning process may provide an objective prediction tool to improve preoperative planning criteria to alert the surgeons for upcoming patients at risk for complications.

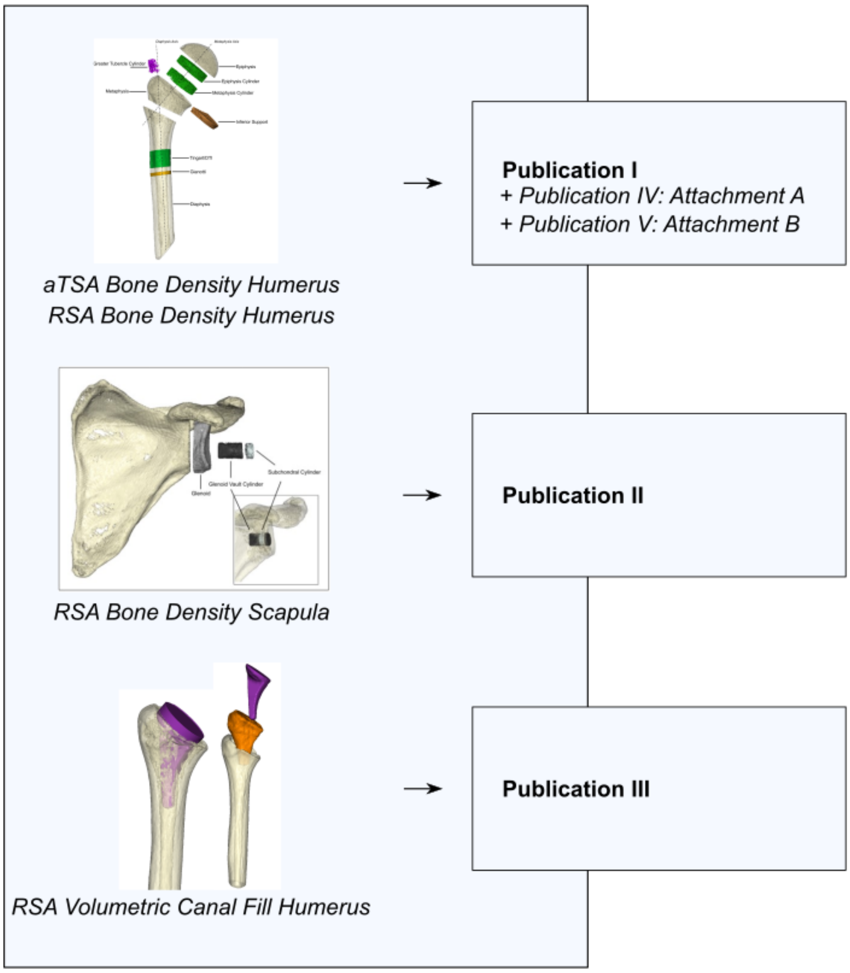

Figure 1 Schematic overview of the sub studies in this work. CT based bone density assessments including machine learning based predictions combined with biomechanical testing resulted in the five publications for this dissertation.

Within the first study, the use of patient-specific calibration in combination with three-dimensional bone volumes was validated in cadaveric CT scans. Significantly improved accuracy in retrospective bone density analyses resulted from more consistent input data for objective bone density quantification. Standardization of the gray scale allowed for significant reduction of unwanted biases and variance. In comparison to multiple imaging studies in clinical [21-23, 44, 57] and non-clinical settings, [32, 43, 54, 58] this work focuses on the variations in multicentric data with the primary goal to improve the use of quantified bone densities.

Application of the bone density classifications on CT scans of cadaveric specimens in the additional studies four and five (Attachment A& B) and the subsequent biomechanical testing showed that preoperatively analyzed bone densities have significant effects on the time-zero biomechanical behavior of respective implants. A cortical rim-supported stemless implant effectively maintains proximal bone loading across variable bone densities compared to a press-fit short stem implant. A context of XAI was included within this study to reduce the black box characteristic of the prediction model.[55, 56]

Further biomechanical investigations in study two and three of this work in combination with preoperative analyzable bone parameters demonstrated significant effects on the primary stability and bone loading when using short and standard stemmed humeral implants and differently augmented glenoid baseplates. Lower humeral canal fill ratios are at higher risk for implant subsidence but increased proximal humeral bone loading similarly to the native humeral bone, in this specific loading setup and implant design. On the glenoid side, higher degree of augmentations showed increased micromotions particularly when associated with lower bone densities and a bone graft augmentation.

All approaches have in common that preoperative CT imaging provided objective classifications or quantifications using the respective implantation-relevant regions of interest. Prospective validation studies or intraoperative verification may allow a clinical implementation of the concepts of these studies to improve preoperative planning tools. These studies combined the benefits of various approaches by using patient-specific calibration to recalibrate multicentric CT scans [51-53], using standardized three-dimensional density analyses [32, 43, 54, 57, 58] and the prediction using machine learning tools [59].

3. Zusammenfassung

Hintergrund: Die präoperative Auswertung von CT-Daten hat signifikante Einflüsse auf die Patientenversorgung und potenzielle spätere Komplikationen bei Schulterarthroplastik Patienten. Eine objektive Klassifizierung der Knochenparameter und die Auswirkungen auf das biomechanische und postoperative Verhalten verschiedener Implantattypen können im präoperativen Entscheidungsprozess des Chirurgen unterstützen. Ziel dieser Studien war es, objektive und konsistente Knochendichteanalysen durchzuführen und die Auswirkungen auf das biomechanische Verhalten von Implantaten zu bewerten.

Methoden: Die Auswertung der CT-Bilddaten umfasste Genauigkeits- und Zuverlässigkeitsanalysen der jeweiligen Parameter, sowie die retrospektive Anwendung in einer multizentrischen CT-Bilddatenbank aus klinischen Kohorten. CT-Scans von Schulterpräparaten wurden mit Mikro-CT-Daten, kalibrierten CT-Daten und postoperativen Röntgenbildern verifiziert. Diese Methoden wurden retrospektiv auf klinische aTSA- (n=150) und RSA-Kohorten (n=345) angewendet. Maschinelles Lernen wurde eingesetzt, um konventionelle statistische Modelle zu verbessern, indem Cluster- und Klassifizierungsalgorithmen verwendet wurden, um präoperative CT-Daten in niedrige und hohe Knochendichten einzuteilen. In biomechanischen Studien wurden die Schulterkadaver zyklisch belastet und in Korrelation zu den präoperative Bilddaten ausgewertet. Die humeralen Implantationen umfassten die Einbringung eines schaftlosen anatomischen Implantats und unterschiedliche Schaftgrößen mit respektiven Knochenkanalfüllverhältnissen sowie verschiedene Augmentierungsmethoden auf der glenoidalen Seite. Zur räumlichen Auswertung der Mikrobewegung der Implantate und zur Quantifizierung kortikaler Knochendeformationen wurden optische Messungen während zyklischen Belastungen durchgeführt.

Ergebnisse: Die Bildverarbeitung und die patientenspezifische Kalibrierung der klinischen CT-Bilder zeigten eine gute bis ausgezeichnete Genauigkeit für die zylindrische Spongiosadichte sowie der volumetrischen Auswertung des Knochenkanals (Intraklassen-Korrelationskoeffizienten >0,75). Die patientenspezifische Kalibrierung standardisierte die Dichtevariablen und ermöglichte damit einen Mehrfachvergleich der multizentrischen Daten. RSA-Patienten wiesen eine signifikant geringere Knochendichte auf als zuvor untersuchte Patienten mit anatomischer Arthroplastik. Die Klassifizierung der RSA-Knochenqualität zeigte im Vergleich zur konventionellen Statistik im Trainings- (Genauigkeit=91,2 %; AUC=0,967) und Testdatensatz (Genauigkeit=90,5 %; AUC=0,958) eine verbesserte Vorhersagegenauigkeit. Biomechanische Stabilität und dynamische Knochenbelastung korrelierten mit den präoperativen CT-Daten. Größere Schaftgrößen resultierten in höherer Stabilität, aber reduzierte ebenfalls die Krafteinleitung im proximalen Humerus. Auf der glenoidalen Seite korrelierten niedrigere Knochendichten mit höheren Mikrobewegung besonders bei der Nutzung eines Knochenaugments.

Schlussfolgerung: Die Auswertung präoperativer CT-Bildgebung resultierte in optimierten Methoden zur Bestimmung der Schaftgrößen und Augmentierungsmethoden, sowie in Klassifizierungen der Knochenqualität unter Verwendung objektiver Ansätze mit dreidimensionalen patientenspezifisch kalibrierter Ergebnisvariablen. Signifikante Auswirkungen auf die biomechanische Stabilität und die Lastübertragung wurden bei den jeweiligen Behandlungsoptionen nachgewiesen.

4. Abstract

Background: Preoperative image processing of CT data can improve planning and treatment of patients undergoing shoulder arthroplasty. Reproducible and objective methods are lacking, even though preoperative CT imaging is commonly performed for planning purposes. Objective evaluation of CT based bone parameters and the impact on biomechanical behavior of different implant types help to understand current clinical findings regarding bone resorptions and complications. The aims of these studies were to perform objective analyses of respective regions of interest to opportunistically use preoperative CT imaging and to evaluate the effects on biomechanical implant behavior.

Methods: The imaging-based approaches included accuracy and reliability analyses of the three-dimensional regions of interest and patient specific calibration, before the retrospective application in clinical cohorts of a multi centric CT image data base. Cadaveric clinical CT scans were compared to micro-CT data and comparatively evaluated with phantom calibrated scans as well as postoperative X-rays to verify these methods. Bone density methods were then retrospectively applied to clinical aTSA (n=150) and RSA (n=345) cohorts. Machine learning was used to improve conventional statistical models by using clustering and classification algorithms to categorize preoperative CT data into low and high bone densities. In biomechanical studies, shoulder cadavers were cyclically loaded and analyzed in correlation to the preoperative image data. The humeral implantations included a stemless anatomic implant and different stem sizes with respective canal filling ratios as well as different augmentation methods on the glenoid side. Optical measurements were performed during cyclic loading to spatially evaluate the micromotion of the implants and to quantify cortical bone deformations.

Results: Image processing and patient-specific calibration of the clinical CT images showed good to excellent accuracy for cylindrical cancellous bone density and volumetric evaluation of the humeral bone canal (intraclass correlation coefficients >0.75). The patient-specific calibration standardized the density variables and thus enabled a multiple comparison of multicentric data. RSA patients showed a significantly lower bone density than previously examined patients with anatomic arthroplasty. The classification of RSA bone quality showed improved prediction accuracy compared to conventional statistics in the training (accuracy=91.2 %; AUC=0.967) and test data set (accuracy=90.5 %; AUC=0.958). Biomechanical stability and dynamic bone loading correlated with the preoperative CT data. Larger stem sizes resulted in higher stability, but also reduced force transmission in the proximal humerus. On the glenoid side, lower bone densities correlated with higher micromotions particularly when using a bony increased offset.

Conclusion: The utility of preoperative CT imaging resulted in optimized methods for determining stem sizes and bone quality classifications using objective approaches with three-dimensional patient-specific calibrated outcome variables. Significant effects on biomechanical stability and load transfer were demonstrated for the respective treatment options. The application of these methods in the preoperative planning process may provide objective prediction tools to improve preoperative planning criteria to alert the surgeons for upcoming patients at risk for complications.

5. Publication I

Citation: Ritter, D; Denard, PJ; Raiss, P; Wijdicks, CA; Werner, BC; Bedi, A.; Müller, PE; Bachmaier, S; Machine Learning Models Can Define Clinically Relevant Bone Density Subgroups based on Patient Specific Calibrated CT Scans in Patients Undergoing Reverse Shoulder Arthroplasty. Journal of Shoulder and Elbow Surgery, doi:10.1016/j.jse.2024.07.006.

J Shoulder Elbow Surg (2024) ■, 1–11

ELSEVIER

Journal of Shoulder and Elbow Surgery

www.elsevier.com/locate/ymse

Machine learning models can define clinically relevant bone density subgroups based on patient-specific calibrated computed tomography scans in patients undergoing reverse shoulder arthroplasty

Daniel Ritter, MSc[a,b,*], Patrick J. Denard, MD[c], Patric Raiss, MD[d], Coen A. Wijdicks, PhD, MBA[a], Brian C. Werner, MD[e], Asheesh Bedi, MD[f], Peter E. Müller, MD[b], Samuel Bachmaier, MSc[a]

[a]*Department of Orthopedic Research, Arthrex, Munich, Germany*
[b]*Department of Orthopaedics and Trauma Surgery, Musculoskeletal University Center Munich (MUM), University Hospital, LMU, Munich, Germany*
[c]*Southern Oregon Orthopedics, Medford, OR, USA*
[d]*OCM Clinic, Munich, Germany*
[e]*Department of Orthopaedic Surgery, University of Virginia Health System, Charlottesville, VA, USA*
[f]*Department of Orthopaedic Surgery, University of Michigan, Ann Arbor, MI, USA*

Background: Reduced bone density is recognized as a predictor for potential complications in reverse shoulder arthroplasty (RSA). While humeral and glenoid planning based on preoperative computed tomography (CT) scans assist in implant selection and position, reproducible methods for quantifying the patients' bone density are currently not available. The purpose of this study was to perform bone density analyses including patient-specific calibration in an RSA cohort based on preoperative CT imaging. It was hypothesized that preoperative CT bone density measures would provide objective quantification of the patients' humeral bone quality.

Methods: This study consisted of 3 parts, (1) analysis of a patient-specific calibration method in cadaveric CT scans, (2) retrospective application in a clinical RSA cohort, and (3) clustering and classification with machine learning (ML) models. Forty cadaveric shoulders were scanned in a clinical CT and compared regarding calibration with density phantoms, air muscle, and fat (patient-specific) or standard Hounsfield unit. Postscan patient-specific calibration was used to improve the extraction of 3-dimensional regions of interest for retrospective bone density analysis in a clinical RSA cohort (n = 345). ML models were used to improve the clustering (Hierarchical Ward) and classification (support vector machine) of low bone densities in the respective patients.

Results: The patient-specific calibration method demonstrated improved accuracy with excellent intraclass correlation coefficients for cylindrical cancellous bone densities (intraclass correlation coefficient >0.75). Clustering partitioned the training data set into a high-density subgroup consisting of 96 patients and a low-density subgroup consisting of 146 patients, showing significant differences between these groups.

Institutional review board approval was not required for this cadaver study. Investigation performed at the Arthrex Department of Orthopedic Research, Munich, Germany.

*Reprint requests: Daniel Ritter, MSc, Department of Orthopedic Research, Arthrex GmbH, Erwin-Hielscher-Strasse 9, Munich 81249, Germany.
E-mail address: publications@arthrex.com (D. Ritter).

https://doi.org/10.1016/j.jse.2024.07.006

The support vector machine showed optimized prediction accuracy of low and high bone densities compared to conventional statistics in the training (accuracy = 91.2%; area under curve = 0.967) and testing (accuracy = 90.5%; area under curve = 0.958) data set.

Conclusion: Preoperative CT scans can be used to quantify the proximal humeral bone quality in patients undergoing RSA. The use of ML models and patient-specific calibration on bone mineral density demonstrated that multiple three-dimensional bone density scores improved the accuracy of objective preoperative bone quality assessment. The trained model could provide preoperative information to surgeons treating patients with potentially poor bone quality.

Level of evidence: Basic Science Study; Imaging and Computer Modeling

Keywords: Reverse shoulder arthroplasty; CT imaging; preoperative bone density; patient-specific calibration; un- and supervised machine learning; explainable machine learning

The presence of osteoporosis in patients undergoing reverse shoulder arthroplasty (RSA) results in significantly increased complication rates with earlier revision surgery, periprosthetic fractures, and acromion and scapular spine fractures.[6,14,21,27,32] An objective bone quality classification for these patients may be beneficial in addition to traditional intraoperative tactile bone investigation (thumb test) and 2-dimensional radiographic measurements (eg, Tingart score and Deltoid Tuberosity Index).[7,36,37] For surgical management, the knowledge of underlying low bone mineral density (BMD) is known to influence the surgeons' choice of implant, surgical technique, humeral stem sizing, and use of cementation.[4,6,2,47]

Mainly demographic and clinical predictors are currently taken into the preoperative assessment for risk stratification without considering quantitative data on BMD from preoperative computed tomography (CT) data.[31] In different anatomies, the three-dimensional (3D) modeling of CT attenuations allows for reliable identification of osteoporosis in routine preoperative CT scans.[40-43] In anatomic total shoulder arthroplasty (aTSA), density interpolations of 3D volumes including a threshold analysis and predictive modeling with machine learning (ML) resulted in good-to-excellent objective bone density classifications.[37] ML applications to predict clinical outcomes may be significantly improved by incorporating preoperative bone density variables, as osteoporosis is present in approximately 26% of RSA cases.[6,19,20,26,39]

Preoperative planning with CT imaging has become a common tool to assess implant positioning and the contact area in RSA patients. CT data may also offer the ability to provide objective measurements of the BMD before surgery.[8,15,22,45] However, gray scale values for density interpolation on the Hounsfield Unit (HU) scale from CT scans have demonstrated variability due to the use of different devices, exposure parameters, the position of the measurement, and the mass inside and outside the field of view.[11,29] Patient-specific calibration of the gray scale values on BMD values have been reported to reduce inaccuracies to optimize objective bone quality assessment.[10,44,49]

The purpose of this study was to perform bone density analyses including patient-specific calibration in an RSA cohort based on preoperative CT imaging. It was hypothesized that preoperative CT bone density measures would provide objective quantification of the patients' humeral bone quality.

Materials and methods

This is a retrospective diagnostic study to define clinically relevant subgroups based on bone densities and demographic data including an investigation in cadaveric CT scans beforehand. The study consisted of 3 parts, (1) validation of a patient-specific calibration method in cadaveric CT scans, (2) retrospective application in a clinical RSA cohort, and (3) clustering and classification with ML models (Fig. 1).

Feature extraction

Forty fresh-frozen cadaveric arm specimens (59.9 ± 5.6 years; body mass index: 22.0 ± 5.5, 17 females and 23 males) were procured (Science Care Inc., Phoenix, AZ, USA) and prepared for density analysis with the arms stored at −20°C. The cadaveric humeri were scanned with a voxel size of 0.6 mm (120 kVp and 80 mA) in a clinical CT scanner (Siemens SOMATOM Definition AS+, Siemens Healthcare GmbH, Erlangen, Germany). Gray scale values were converted into BMD [mgHA/cm3; HA - Hydroxyapatite] values using patient-specific calibration and HU values and compared to the ground true BMD scale based on the manufacturer's density phantoms. In addition to BMD values, the morphological parameter (bone volume [BV]/total volume [TV]) calculation of each volume of interest (VOI) was based on pixel counting methods using the respective BV of the TV. A custom image processing script (Matlab version 2023a; MathWorks, Natick, MA, USA) with segmentation and morphological image processing steps was created to investigate the CT scans of the cadaveric humeri and retrospective clinical CT scans. Bone model development was performed based on CT voxel data imported as a 4-dimensional point cloud (ie, [x, y, z mgHA/cm3]). Density variables were evaluated according to a previous work[37] and included the Tingart score[48] (*Tingart*), global bone portions of the epiphysis (*Epi_BMD*), metaphysis (*Meta_BMD* and *Meta_BV/TV*), and the entire humerus from the epiphysis down to the Tingart measuring point (*Global hydroxyapatite*). Implantation relevant VOIs included cancellous cylindric epiphysis

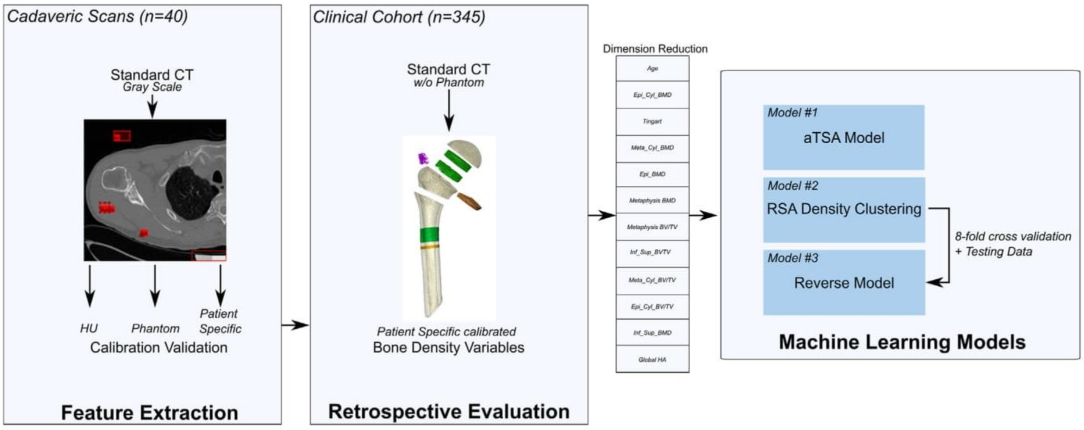

Figure 1 Schematic illustration of specimen allocation of the different examinations and structure of the analysis steps in terms of feature extraction in cadaveric scans, retrospective evaluation in a clinical cohort, and bone quality classification using machine learning models. *CT*, computed tomography; *HU*, Hounsfield Unit; *TSA*, total shoulder arthroplasty; *RSA*, reverse shoulder arthroplasty.

(*Epi_Cyl_BMD* and *Epi_Cyl_BV/TV*), cancellous cylindric metaphysis (*Meta_Cyl_BMD* and *Meta_Cyl_BV/TV*), and the inferior supporting bone (*Inferior Support BMD* and *Inferior Support BV/TV*).[37]

Retrospective evaluation

A retrospective review was performed on a multicenter database (Virtual Implant Positioning VIP, Arthrex Inc., Naples, FL, USA) of shoulder arthroplasties (345 patients; 71 ± 9 years; 172 females and 173 males) performed from December 2019 to December 2023. Inclusion criteria were: primary RSA, glenohumeral osteoarthritis and rotator cuff deficiency, a preoperative CT scan, and humeral fixation with either a press-fit standard-length stem (Univers Revers Total Shoulder System; Arthrex Inc.) or short stem (Univers Revers Apex Total Shoulder System; Arthrex Inc.) implant.

A total of 345 preoperative CT scans were identified from 157 different scanners/sites. To set a baseline for differing scales of the retrospectively gathered CT scans resulting from intra- and interscanner variations, patient-specific air-muscle-fat calibration was performed to interpolate the gray scales on BMD values recently reported with good functionality.[10,44,49] Therefore, air, fat and muscle gray values were used to linearly interpolate the CT data using the respective density scale [−840, −80, 30 mgHA/cm^3] to allow for improved application of the image processing steps on more consistent data. The reliability and accuracy of the patient-specific calibration was initially verified by applying the method on the cadaveric scans and compare them to ground true BMD-phantom calibrated values. Scanning parameters were defined according to specifications needed for the use of a planning software (Virtual Implant Positioning VIP, Arthrex Inc.) with resolutions below 0.6 mm (range 0.35-0.6 mm). The anonymized preoperative CT scans were evaluated using the custom image processing script. Based on the outcome variables, predictive models were developed using defined principal variables for objective bone quality classifications.

Machine learning models

The applications of trained ML models generally return predictions, in our study, for example, if caution is required due to poor bone density. The model of a previous study created in an aTSA cohort served as a comparison model (model 1) and was applied on the RSA training data set.[37] None of the cohorts showed differences in gender distribution (aTSA: 47% females, RSA Training: 50% females, RSA Testing: 50% females). In this work, models were created based on an RSA cohort (model 2 and model 3) and compared to each other and to a conventional statistical multivariate approach (Logistic Regression [LR]).

Outcome parameters for comparison included demographic and bone density data from available CT scans. According to the Scree plot, 5 parameters were found to be sufficient to define the statistical models describing 99% of the data variance. Variable selection was performed by choosing the variables with the highest descriptive value for each correlation clustered variables (Fig. 2, *A*) and served as principal variables for classifications and predictions (*Age*, *Epiphyseal Cylindrical BV/TV*, *Metaphyseal Cylindrical BV/TV*, *Epiphyseal Cylindrical BMD*, and *Inferior Support BMD*). Variables as input for the anatomic cohort prediction were defined by the respective model (Table I).[37]

The extracted bone density variables of the retrospective cohort served as unlabeled data set for the prediction models as no information about osteoporosis or respective treatment, medication, or other indicators were available. Additionally, the RSA treatment decision in this study does not imply any information about the bone density in this cohort, as only stemmed (short and standard stem) arthroplasties were available. Hence, patients were partitioned into distinct subgroups based on their bone density using unsupervised clustering. Clustering is a ML technique that outputs regions in the data space based on specified distance measure, variance, or distributions. This technique is often used for exploratory analysis, dimensionality reduction, and outlier removal. In this work, an ideal clustering assignment yields distinct subgroups, each associated with a different bone density

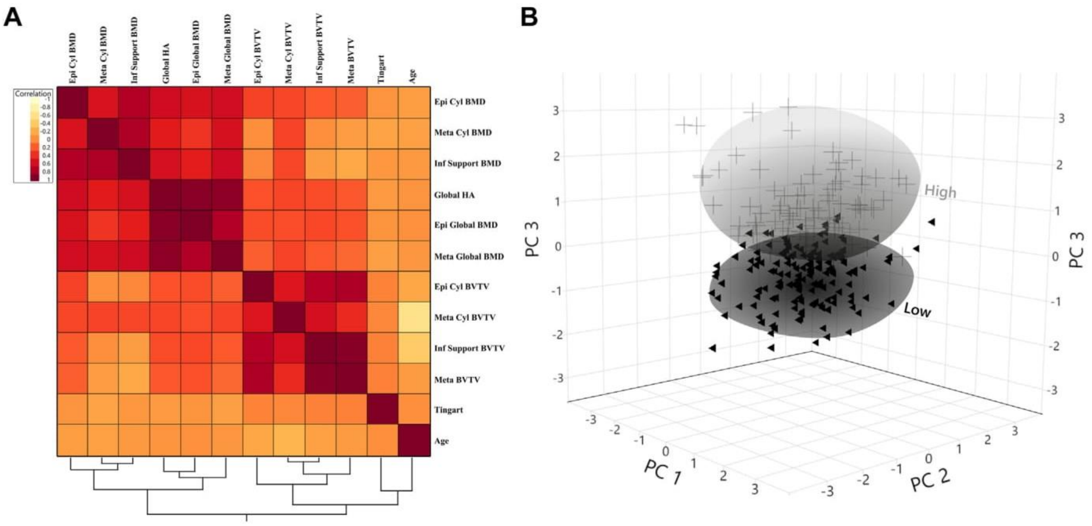

Figure 2 (**A**) Visualization of the outcome variables sorted according to correlation clusters for later variable selection and (**B**) cluster visualization of the principal components based on the unsupervised ML clustering results (model 2). *ML*, machine learning; *BMD*, bone mineral density; *PC*, principal components; *HA*, hydroxyapatit; *BVTV*, bone volume per total volume.

Table I Summary of the predictive models including the methods used, input data, and the targeted prediction

No. & name	1 anatomic	2 RSA density cluster	3 reverse
Model type	Application of supervised model	Unsupervised model	Supervised model
Methods	SVM	Hierarchical Ward	SVM Logistic regression (LR)
Data set	Training data	Training data	Training data (n = 242 ~ 70%) incl. 8-fold cross validation Testing data (n = 103 ~ 30%)
Short description	Application of classifier (anatomic)[37]	Defining RSA bone density clusters	Validated classification into RSA bone density clusters
Input variables	Defined by model: • Age • Epi_Cyl_BMD • Tingart • Meta_Cyl_BMD • Epi_BMD	From correlation clustering: • Age • Epi_Cyl_BMD • Epi_Cyl_BVTV • Meta_Cyl_BVTV • Inferior Support BMD	
Prediction	Anatomic treatment	Low- or high-BMD cluster	Low- or high-BMD cluster (validated & tested)

SVM, support vector machine; *BMD*, bone mineral density; *RSA*, reverse shoulder arthroplasty.

group. The Ward's minimum variance criterion was used in an agglomerative hierarchical clustering to determine the optimal number of clusters and cluster assignments.[18,23] The quality of clustering algorithms was assessed using internal validation metrics based on the partitions produced and the subjects within each cluster. We used the Silhouette, Gap, Davies-Bouldin, and Calinski-Harabasz criteria to select the best candidate clustering algorithm and number of clusters. A principal component analysis was performed to reduce the dimensions for each patient into a 3-dimensional coordinate system. Patients were then plotted in the resulting coordinate system consisting of the 3 principal components with their subgroup labels (Fig. 2, *B*).

The optimal clusters were refined for data labeling purposes using the distance between individual data points and cluster mean value to assign patients at the cluster boarder manually to the correct bone density cluster (semiautomated labeling).[30] Based on these labels we developed a supervised machine learning (SML) model to predict the likelihood that a future patient will fall in the high- or low-density

Table II Intraclass correlation coefficients to assess the accuracy of bone densities based on clinical CT scans and the use of different calibration methods

	Patient-specific vs. Phantom		HU vs. Phantom		Patient-specific vs. HU	
	ICC (CI 95%)	*P* value	ICC (CI 95%)	*P* value	ICC (CI 95%)	*P* value
Global BMD						
Epiphysis BMD	0.405 (0.164-0.999)	***.017***	*0.445 (0.245-0.999)*	.096	0.239 (0.025-0.627)	*.796*
Metaphysis BMD	0.329 (0.183-0.999)	***.012***	*0.316 (0.040-0.983)*	.664	0.308 (0.014-0.983)	*.136*
Metaphysis BV/TV	0.464 (0.180-0.999)	.176	*0.492 (0.013-0.998)*	***.010***	0.641 (0.877-0.999)	*.099*
Global HA	0.247 (0.212-0.999)	***.008***	*0.138 (0.037-0.991)*	.709	0.336 (0.014-0.984)	*.126*
VOIs:						
Meta_Cylinder BMD	0.871 (0.270-0.999)	***.014***	*0.599 (0.081-0.994)*	.572	0.850 (0.215-0.999)	***.012***
Meta_Cylinder BV/TV	0.792 (0.084-0.999)	***.031***	*0.761 (0.232-0.989)*	***.023***	0.820 (0.062-0.999)	***.021***
Epi_Cylinder BMD	0.871 (0.271-0.999)	***.014***	*0.599 (0.082-0.994)*	.571	0.406 (0.022-0.946)	*.076*
Epi_Cylinder BV/TV	0.838 (0.154-0.999)	***.015***	*0.795 (0.024-0.985)*	***.023***	0.814 (0.027-0.999)	***.023***
Inferior Support BMD	0.844 (0.380-0.999)	***.012***	*0.743 (0.457-0.841)*	***.019***	0.853 (0.233-0.999)	***.011***
Inferior Support BV/TV	0.753 (0.288-0.999)	***.047***	*0.565 (0.017-0.997)*	***.021***	0.682 (0.660-0.999)	*.080*
Scores:						
Tingart	0.241 (−0.112 to 0.887)	.180	*0.203 (0.083-0.879)*	.083	0.588 (0.023-0.937)	*.445*

BMD, bone mineral density; *BV/TV*, bone volume/total volume; *VOI*, volume of interest; *ICC*, intraclass correlation coefficient; *HU*, Hounsfield Unit; *CI*, confidential interval.
Italic bold values denotes *P* value < .5.

cluster using preoperative variables. ML models for group classification were created using a support vector machine (SVM) which is a SML model that is commonly used for pattern recognition, classification, and regression analysis. Hyperparameter tuning was performed using a Bayesian optimization method to tune kernel functions including a k-fold cross-validation ($k = 8$). The SML models were constructed in accordance with the transparent reporting of a multivariable prediction model for individual prognosis or diagnosis guidelines and the guidelines for developing and reporting ML models in biomedical research.[12,13,24]

Statistical analysis

The accuracy of the extracted features of the cadaveric clinical CT scans was analyzed by examining different calibration methods using intraclass correlation coefficients (ICCs). A 2-way random effects analysis for single measures is taken in the experiment and reliability is applied in a context of the absolute agreement of a single measure. ICCs greater than 0.75 were considered excellent, ICCs of 0.40-0.75 were considered to indicate moderate reliability, and ICCs of less than 0.40 was considered to indicate poor reliability.[17,25]

Statistical analysis of the retrospectively evaluated cohort included a 1-way analysis of variance with a Holm-Sidak post hoc test performed for significant pairwise analysis. Significance was defined as $P \leq .05$ and the power level was higher than 0.8 for these tests. No prior sample size calculation was performed, as no matching mean and standard deviation values were found for our outcome variables and methods. The Shapiro-Wilk and Brown-Forsythe tests were used to confirm each data set followed a normal distribution and equal variance, respectively. A nonparametric test (Kruskal-Wallis) was used for non-normal distributed data sets with unequal variances. Normal distributed heteroscedastic data sets did not appear in this study. For Kruskal-Wallis tests that found significance, Dunn's post hoc tests including Bonferroni correction were conducted to further analyze the differences.

All statistical analyses were performed using commercial software (JMP, version 17.0.0, JMP Statistical Discovery, Cary, NC, USA; and Matlab version 2023a, MathWorks, Natick, MA, USA).

Results

Feature extraction

Validation of the patient-specific calibration method demonstrated improved accuracy with excellent ICCs for specific BMD VOIs using patient-specific calibration compared to phantom calibrated cadaveric CT scans. The extracted features for standard HU values showed moderate ICCs (Table II).

Retrospective evaluation

The data sets of the retrospectively analyzed anatomic[37] and reverse cohort with respective parameters showed significant differences in age and bone density variables (Table III). The randomly separated training and testing data sets in the RSA cohort did not differ significantly (Table III).

Machine learning models

Clustering partitioned this cohort (training data set) into a high-density subgroup consisting of 96 patients and a low-density subgroup consisting of 146 patients. The optimal number of clusters ($n = 2$) was determined based on the optimization metrics shown in Table IV.

Table III Statistical comparison of the different patient cohorts (anatomic, RSA testing, RSA training)

	Anatomic[37] N = 150	Reverse - training N = 242	Reverse - testing N = 103	Reverse vs. anatomic *P* value	Reverse training vs. testing *P* value
Global BMD					
Epiphysis BMD	*393 ± 45*	*389 ± 42*	*395 ± 44*	.374	.491
Metaphysis BMD	*378 ± 43*	*373 ± 39*	*379 ± 43*	.224	.283
Metaphysis BV/TV	*0.35 ± 0.13*	*0.36 ± 0.15*	*0.35 ± 0.13*	.691	.685
Global HA	*428 ± 76*	*429 ± 92*	*425 ± 52*	.938	.992
VOIs:					
Meta_Cylinder BMD	*281 ± 41*	*271 ± 45*	*272 ± 34*	**.041**	.951
Meta_Cylinder BV/TV	*0.23 ± 0.09*	*0.19 ± 0.06*	*0.20 ± 0.06*	**.004**	.622
Epi_Cylinder BMD	*302 ± 36*	*293 ± 40*	*295 ± 40*	.109	.397
Epi_Cylinder BV/TV	*0.37 ± 0.14*	*0.34 ± 0.11*	*0.33 ± 0.11*	**<.001**	.865
Inferior Support BMD	*301 ± 48*	*303 ± 38*	*310 ± 32*	.151	.268
Inferior Support BV/TV	*0.34 ± .11*	*0.31 ± 0.14*	*0.31 ± 0.13*	**.024**	.148
Scores:					
Tingart	*3.2 ± 0.4*	*3.2 ± 0.5*	*3.2 ± 0.4*	.907	.913
Age	*69 ± 10*	*71 ± 8*	*71 ± 9*	**.006**	.948

BMD, bone mineral density; *BV/TV*, bone volume/total volume; *VOI*, volume of interest.
Italic and bold values denotes *P* value < .5.

Figure 2, *A* shows the measurements of the BMD and the morphological variables clustered according to correlation allowing for selection of representative variables for each correlation cluster resulting in the principal variables. Visualization of the 2 patient subgroups based on density clustering is shown in Figure 2, *B* in reduced 3 dimensionality. The eased visualization of the data sets shows patients with lower bone density as black triangles while the gray pluses denote higher density, with apparent partition between the 2 subgroups.

The classification results of the anatomic model and the RSA density clusters respectively showed significant differences between the low- and high-bone density clusters (Table V). Descriptive statistics of the respective classified groups did not differ significantly between model 1 and 2, even though 27% of the patients were differently classified (Table V Confusion Matrix).

The reverse classification (model 3) therefore served as validation for the created RSA density labels resulting in a significantly improved performance (accuracy = 91.2% and area under curve (AUC) = 0.967) compared to a conventional LR model (model LR: accuracy = 78.5%, Fig. 3, *A*). Figure 3, *A* shows the model performance in the testing data set (model 3: accuracy = 90.5 and AUC = 0.958).

The exemplary local interpretable model-agnostic explanation in Figure 3, *B* shows a patient assigned to a low bone density with an associated probability of 0.734. Features that supported this prediction included the BMD of inferior supporting and cancellous epiphyseal bone as well as the metaphyseal cylindrical BV/TV despite a relatively 'young' age and 'good' epiphyseal bone stock (Fig. 3, *B*).

Discussion

The most important finding of this study was that preoperative CT data analysis can objectively quantify the bone quality in the proximal humerus. The use of patient-specific calibration in combination with 3-dimensional VOIs significantly improved the accuracy in retrospective bone density analyses to provide a consistent input for objective bone density quantification. A ML algorithm showed excellent discriminant performance in a training (AUC = 0.967) and testing (AUC = 0.958) data set. Our study combined the strength of various recent approaches by applying systemic standardized 3D density analyses and the prediction and threshold analyses using ML tools in an RSA cohort.[3,5,31,34,35,37] The black box characteristic of ML and artificial intelligence applications was elucidated in this work by a breakdown of the decision for 1 exemplary patient.[13,16] These tools may help augment preoperative planning in RSA.

The prevalence of osteoporosis in the shoulder arthroplasty population is significant and expected to rise due to the increasing number of older adults undergoing these procedures, highlighting the importance of preoperative identification of patients with a low-bone quality.[2,9] Our study results correlate with the findings from Casp et al of a higher incidence of osteoporosis (26.2%) in RSA patients resulting in significant lower bone densities compared to an aTSA cohort with the same variables evaluated.[37] Daher et al. even recommended a artificial intelligence BMD measurement for high-risk orthopedic surgical candidates,[9] as there are currently no approaches to identify low-density RSA patients based on preoperative imaging data,

Table IV Internal validation statistics of ideal cluster numbers

Hierarchical Ward	2	3	4	5	6
Calinski-Harabasz	**223.8**	223.5	213.1	216.5	220.3
Davies-Bouldin	**0.77**	0.95	0.88	0.95	0.84
Gap	**0.97**	0.88	0.86	0.92	0.95
Silhouette	**0.69**	0.45	0.49	0.43	0.47

Bold indicates *P* value < .05.

Table V Mean values and statistical analysis of the density variables for patients assigned to high- or low-bone density group and differences in the classifications shown as a confusion matrix

	Model 1 (anatomic)			Model 2 (RSA density cluster)		
	High N = 99	Low N = 143	*P* value	High N = 96	Low N = 146	*P* value
Global BMD						
Epiphysis BMD	*417 ± 35*	*370 ± 35*	<***.0001***	*408 ± 41*	*378 ± 37*	<***.0001***
Metaphysis BMD	*394 ± 33*	*358 ± 36*	<***.0001***	*392 ± 35*	*360 ± 36*	<***.0001***
Metaphysis BV/TV	*0.37 ± 0.16*	*0.35 ± 0.14*	.382	*0.37 ± 0.13*	*0.35 ± 0.16*	.359
Global Humerus	*456 ± 82*	*411 ± 94*	***.002***	*446 ± 82*	*418 ± 96*	***.030***
VOIs:						
Meta_Cylinder BMD	*294 ± 44*	*256 ± 39*	<***.0001***	*298 ± 48*	*255 ± 34*	<***.0001***
Meta_Cylinder BV/TV	*0.19 ± 0.06*	*0.15 ± 0.05*	<***.0001***	*0.22 ± 0.06*	*0.14 ± 0.03*	<***.0001***
Epi_Cylinder BMD	*323 ± 33*	*275 ± 31*	<***.0001***	*325 ± 33*	*275 ± 31*	<***.0001***
Epi_Cylinder BV/TV	*0.36 ± 0.11*	*0.29 ± 0.10*	<***.0001***	*0.38 ± 0.11*	*0.28 ± 0.08*	<***.0001***
Inferior Support BMD	*327 ± 31*	*288 ± 31*	<***.0001***	*330 ± 34*	*288 ± 30*	<***.0001***
Inferior Support BV/TV	*0.34 ± 0.14*	*0.28 ± 0.13*	***.002***	*0.37 ± 0.14*	*0.27 ± 0.10*	<***.0001***
Scores:						
Tingart	*3.3 ± 0.5*	*3.1 ± 0.5*	.074	*3.2 ± 0.5*	*3.2 ± 0.4*	.896
Age	*71 ± 8*	*72 ± 8*	.492	*71 ± 8*	*72 ± 8*	.457
Confusion Matrix						

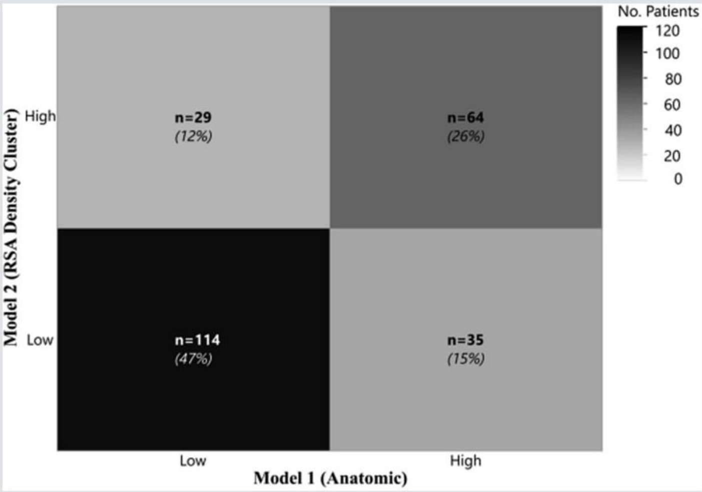

BMD, bone mineral density; *BV/TV*, bone volume/total volume; *VOI*, volume of interest; *RSA*, reverse shoulder arthroplasty.
Italic bold values denotes *P* value < .5.

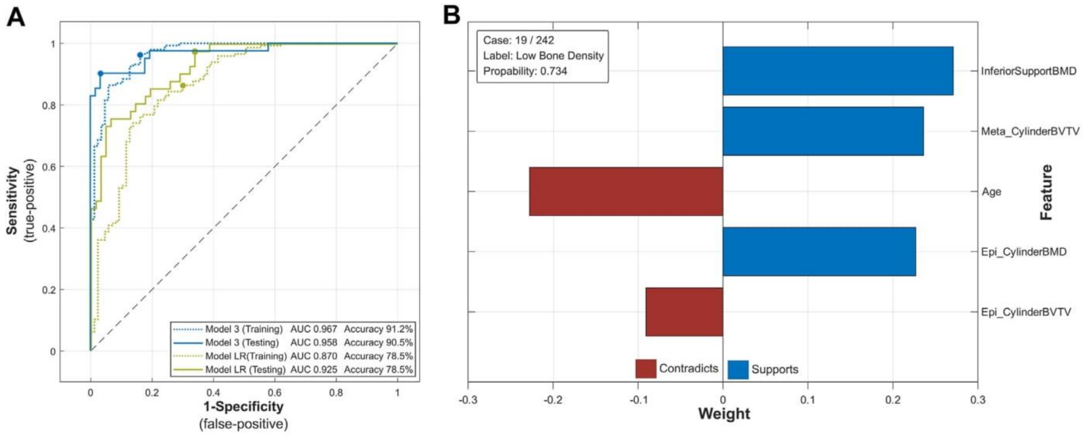

Figure 3 (**A**) Discrimination of the considered reverse model (model 3) showed comparable performance for training and testing data (no overfitting) while outperforming the conventional statistical model (logistic regression) including the model operating point allowing to create (**B**) local interpretable model-agnostic explanation for the predicted label output from the SML model for the selected patient number 19; this patient would receive a preoperative low bone density subgroup membership with a probability of 0.734 even though the patient was relatively 'young' (age 58 years, male) and the measured cylindrical epiphyseal bone stock (Epi_Cylinder_BVTV) was relatively 'good.' *SML*, supervised machine learning; *LR*, logistic regression; *BMD*, bone mineral density.

although there are several investigations for aTSA patients.[15,22,37] While there are several imaging studies available investigating the humeral bone density for stemless arthroplasty implications,[3,5,8,15,22,31,34,35,38,45] the primary goal of the current study was to improve the use of quantified bone densities based on CT data to alert the surgeon preoperatively for potential complications in RSA. Increased age, glenohumeral osteoarthritis, and rotator cuff deficiency in RSA cohorts are known to systematically influence the patients' bone density which is associated with acromial and scapular spine fractures, implant loosening, periprosthetic fracture, and revision surgery.[6,14,21,27,32] Glenoid-sided complications may be more correlated with the scapular bone density, but standard circular 2D HU measurements in the glenoid vault achieved only moderate accuracy in predicting bone density (AUC = 0.75),[46] whereas humeral bone density variables provided more accurate bone density classifications for the respective patients (AUC = 0.967). Especially for surgical management, low bone density influences the surgeons' choice of implant, surgical technique, stem sizing and use of cementation.[2,4,6,47] The objective classification model in this study may, therefore, support the surgeons' decision-making process, especially regarding the use of stemless implants in RSA and increasing bone density related complication rates. However, incorporation of glenoid bone density variables may improve predictions particularly for preoperative planning and potential complications at the glenoid side. Particularly, the bone density data may have implications for soft tissue tensioning to reduce the incidence of acromial stress fractures in the preoperatively at-risk classified population.[28]

The higher shear forces on the humeral components with stemless RSAs require strategically located implant fixation features below the anatomic neck to provide sufficient primary fixation strength.[1,3,33] The use of specific VOIs in this study based on the relevant regions for implant fixation features, improved the accuracy of the density evaluation compared to 2D measures or global volumes.[37] Additionally, intrascanner variability was reduced by using patient-specific linear interpolation on a BMD scale, which was verified in our study with phantom calibrated values with excellent ICCs. As only 1 scanner with the same scanning parameters was used to compare the calibration methods, the HU values showed similarly good intra class correlations. However, inaccuracies can be expected to be higher when different CT devices and exposure parameters are used.[10,37,44,49] The reduction of these inaccuracies recently resulted in significantly improved predictions (AUC = 0.93) compared to standard HU values (AUC = 0.73) in a multicentric aTSA cohort.[46]

Various studies using ML models have shown good results in predicting osteoporosis from standard preoperative CT scans with improved classifications when using CT attenuations of multiple bones compared to any single bone.[40-43] SVMs with various kernel functions showed excellent discriminant power in these models, comparable to our findings, with several bone density parameters selected as input for reliable bone density SVM classification in both training and testing data. The fact that 27% of the cases differed from the anatomical classification model confirms the importance of tailoring ML models on the problem to be solved. The danger of overfitting and overinterpretation in tailoring these models was addressed with internal validation statistics (k-fold cross validation) and a testing data set providing external validity as the data originated from 157 differently adjusted scanners from different sites. The higher proportion of patients with a lower bone density compared to the anatomic cohort[37] confirms the systematically lower BMD in RSA and the functionality of our classification by additionally outperforming the conventional statistical model (LR). In addition to the current clinical predictors of RSA complications, the quantification of bone density defines the baseline value (poor bone density/osteoporosis) that are known to correlate with the currently used predictors.[2] Therefore, the use of bone density may complete the set of variables, especially when predicting clinical improvement or complications, which to our knowledge is currently not the case in these models.[19,20,26,39]

In accordance with current literature, our results demonstrated that opportunistic screening of the bone quality in the proximal humerus can be performed based on routine CT scans obtained for RSA. To apply this study in a clinical setting, a prospective validation study or an intraoperative bone density verification may help to implement the concepts of this study in a preoperative planning tool to improve intraoperative or 2D HU measures.

Limitations

We acknowledge some limitations to the current study. Validation of the patient-specific calibration was only performed in 1 scanner and with the same scanning parameters. Further intra- and interscanner differences can be addressed by including phantom calibration during clinical scanning in future studies. In addition, RSA patients with our inclusion criteria showed systematically reduced bone densities in an older cohort. Gender considerations did not add value to our predictions; however, inclusion of categorical, pre- and postoperative clinical data may increase the impact of these models. Nevertheless, density analysis and ML models are intended to work in an RSA clinical population with standard CT scans (without phantom), as demonstrated in the current approach. Prospective validation studies should aim to validate the developed classification models and already existing thresholds, to further elucidate optimal prediction of adequate bone quality for successful implant fixation. Bone density predictions for the impact of glenoid sided complications should be used with caution, as they are based on local humeral BMD values. Future work should therefore incorporate scapular bone density parameters into these models for better validity on the glenoid side. Additionally, critical bone qualities with variable anchoring principles may be applicable to a wider range of patient bone qualities, and the influence of design specific bone density parameters remains a research question.

Conclusion

Preoperative CT scans can be used to quantify the proximal humeral bone quality in patients undergoing RSA. The use of ML models and patient-specific calibration on BMD demonstrated that multiple 3D bone density scores improved the accuracy of objective preoperative bone quality assessment. The trained model could provide preoperative information to surgeons treating patients with potentially poor bone quality.

Disclaimers:

Funding: Arthrex provided full support of this study. Patrick J. Denard receives support for travel to meetings for the study or other purposes from Arthrex. Patric Raiss receives support for travel to meetings for the study or other purposes from Arthrex. Brian C. Werner receives research support from Arthrex, Zimmer Biomet, Exactech, Pacira, and Lifenet and receives support for travel to meetings for the study or other purposes from Arthrex. Asheesh Bedi receives support for travel to meetings for the study or other purposes from Arthrex.
Conflicts of interest: Daniel Ritter is an employee of Arthrex. Patrick J. Denard receives consulting fees and honoraria from Arthrex and receives royalties from Arthrex. Patric Raiss receives consulting fees and honoraria from Arthrex. Coen A. Wijdicks is an employee of Arthrex. Brian C. Werner receives consulting fees and honoraria from Arthrex, Pacira, and Lifenet. Asheesh Bedi receives consulting fees and honoraria from Arthrex and receives royalties from Arthrex. Samuel Bachmaier is an employee of Arthrex.

References

1. Alidousti H, Giles JW, Emery RJH, Jeffers J. Spatial mapping of humeral head bone density. J Shoulder Elbow Surg 2017;26:1653-61. https://doi.org/10.1016/j.jse.2017.03.006
2. ASES Complications of RSA Research Group, Mahendraraj KA, Abboud J, Armstrong A, Austin L, Brolin T, et al. Predictors of acromial and scapular stress fracture after reverse shoulder arthroplasty: a study by the ASES complications of RSA Multicenter Research Group. J Shoulder Elbow Surg 2021;30:2296-305. https://doi.org/10.1016/j.jse.2021.02.008
3. Bachmaier S, Flury M, Lichtenberg S, Schwyzer H-K, Anderl W, Denard PJ, et al. Postpreparation peri-implant humeral bone density and fixation strength vary based on design in stemless reverse shoulder

arthroplasty. Semin Arthroplasty 2021;31:677-87. https://doi.org/10.1053/j.sart.2021.04.005

4. Bernatz JT, Brooks AE, Nguyen BP, Shin ED, Binkley NC, Anderson PA, et al. Prevalence and treatment of osteoporosis prior to elective shoulder arthroplasty. J Am Acad Orthop Surg Glob Res Rev 2020;4:e20.00204. https://doi.org/10.5435/JAAOSGlobal-D-20-00204
5. Blakeney WG, Urvoy M, Chaoui J, Raiss P, Athwal GS, Walch G. Development and assessment of 3-dimensional computed tomography measures of proximal humeral bone density: a comparison to established 2-dimensional measures and intraoperative findings in patients undergoing shoulder arthroplasty. JSES Int 2021;5:1008-13. https://doi.org/10.1016/j.jseint.2021.07.015
6. Casp AJ, Montgomery SRJ, Cancienne JM, Brockmeier SF, Werner BC. Osteoporosis and implant-related complications after anatomic and reverse total shoulder arthroplasty 2020;28:121-7. https://doi.org/10.5435/jaaos-d-18-00537
7. Churchill RS, Chuinard C, Wiater JM, Friedman R, Freehill M, Jacobson S, et al. Clinical and radiographic outcomes of the simpliciti canal-sparing shoulder arthroplasty system: a prospective two-year multicenter study. J Bone Joint Surg Am 2016;98:552-60. https://doi.org/10.2106/JBJS.15.00181
8. Cronin KJ, Vaughan A, Tzeuton S, Abboud JA. Prospective assessment of osteoporosis in total shoulder arthroplasty. Semin Arthroplasty 2023;33:15-21. https://doi.org/10.1053/j.sart.2022.07.015
9. Daher M, Fares MY, Boufadel P, Khanna A, Zalaquett Z, Abboud JA. Osteoporosis in the setting of shoulder arthroplasty: a narrative review. Geriatr Orthop Surg Rehabil 2023;14:21514593231182527. https://doi.org/10.1177/21514593231182527
10. Eggermont F, Verdonschot N, van der Linden Y, Tanck E. Calibration with or without phantom for fracture risk prediction in cancer patients with femoral bone metastases using CT-based finite element models. PLoS One 2019;14:e0220564. https://doi.org/10.1371/journal.pone.0220564
11. Free J, Eggermont F, Derikx L, van Leeuwen R, van der Linden Y, Jansen W, et al. The effect of different CT scanners, scan parameters and scanning setup on Hounsfield units and calibrated bone density: a phantom study. Biomed Phys Eng Expr 2018;4:12. https://doi.org/10.1088/2057-1976/aad66a
12. Groot OQ, Ogink PT, Lans A, Twining PK, Kapoor ND, DiGiovanni W, et al. Machine learning prediction models in orthopedic surgery: a systematic review in transparent reporting. J Orthop Res 2022;40:475-83. https://doi.org/10.1002/jor.25036
13. Gupta P, Haeberle HS, Zimmer ZR, Levine WN, Williams RJ, Ramkumar PN. Artificial intelligence-based applications in shoulder surgery leaves much to be desired: a systematic review. JSES Rev Rep Tech 2023;3:189-200. https://doi.org/10.1016/j.xrrt.2022.12.006
14. Harmer L, Throckmorton T, Sperling JW. Total shoulder arthroplasty: are the humeral components getting shorter? Curr Rev Musculoskelet Med 2016;9:17-22. https://doi.org/10.1007/s12178-016-9313-3
15. Hayden A, Cotter EJ, Hennick T, Hetzel S, Wollaeger J, Anderson S, et al. Bone quality in total shoulder arthroplasty: a prospective study correlating CT Hounsfield units with thumb test and FRAX score. JSES Int 2023;7:628-35. https://doi.org/10.1016/j.jseint.2023.03.012
16. Innocenti B, Radyul Y, Bori E. The use of artificial intelligence in orthopedics: applications and limitations of machine learning in diagnosis and prediction. Appl Sci 2022;12:10775. https://doi.org/10.3390/app122110775
17. Koo TK, Li MY. A guideline of selecting and reporting intraclass correlation coefficients for reliability research. J Chiropr Med 2016;15:155-63. https://doi.org/10.1016/j.jcm.2016.02.012
18. Kruse C, Eiken P, Vestergaard P. Clinical fracture risk evaluated by hierarchical agglomerative clustering. Osteoporos Int 2017;28:819-32. https://doi.org/10.1007/s00198-016-3828-8
19. Kumar V, Roche C, Overman S, Simovitch R, Flurin PH, Wright T, et al. Using machine learning to predict clinical outcomes after shoulder arthroplasty with a minimal feature set. J Shoulder Elbow Surg 2021;30:e225-36. https://doi.org/10.1016/j.jse.2020.07.042
20. Kumar V, Roche C, Overman S, Simovitch R, Flurin PH, Wright T, et al. What is the accuracy of three different machine learning techniques to predict clinical outcomes after shoulder arthroplasty? Clin Orthop Relat Res 2020;478:2351-63. https://doi.org/10.1097/CORR.0000000000001263
21. Kumar S, Sperling JW, Haidukewych GH, Cofield RH. Periprosthetic humeral fractures after shoulder arthroplasty. J Bone Joint Surg Am 2004;86:680-9. https://doi.org/10.2106/00004623-200404000-00003
22. Levin JM, Rodriguez K, Polascik BA, Zeng S, Warren E Jr, Rechenmacher A, et al. Simple preoperative radiographic and computed tomography measurements predict adequate bone quality for stemless total shoulder arthroplasty. J Shoulder Elbow Surg 2022;31:2481-7. https://doi.org/10.1016/j.jse.2022.05.008
23. Lu Y, Salmons HI, Mickley JP, Bedard NA, Taunton MJ, Wyles CC. Defining clinically meaningful subgroups for risk stratification in patients undergoing revision total hip arthroplasty: a combined unsupervised and supervised machine learning approach. J Arthroplasty 2023;38:1990-7.e1. https://doi.org/10.1016/j.arth.2023.06.027
24. Luo W, Phung D, Tran T, Gupta S, Rana S, Karmakar C, et al. Guidelines for developing and reporting machine learning predictive models in biomedical research: a multidisciplinary view. J Med Internet Res 2016;18:e323. https://doi.org/10.2196/jmir.5870
25. McGraw KO, Wong SP. Forming inferences about some intraclass correlation coefficients. Psychol Methods 1996;1:30-46.
26. McLendon PB, Christmas KN, Simon P, Plummer OR, Hunt A, Ahmed AS, et al. Machine learning can predict level of improvement in shoulder arthroplasty. JB JS Open Access 2021;6:e20.00128. https://doi.org/10.2106/JBJS.OA.20.00128
27. Nagels J, Stokdijk M, Rozing PM. Stress shielding and bone resorption in shoulder arthroplasty. J Shoulder Elbow Surg 2003;12:35-9. https://doi.org/10.1067/mse.2003.22
28. Nappo KE, Christensen DL, Wolfe JA, Tintle SM. Glenoid neck Hounsfield units on computed tomography can accurately identify patients with low bone mineral density. J Shoulder Elbow Surg 2018;27:1268-74. https://doi.org/10.1016/j.jse.2017.11.008
29. Pauwels R, Jacobs R, Singer SR, Mupparapu M. CBCT-based bone quality assessment: are Hounsfield units applicable? Dentomaxillofac Radiol 2015;44:20140238. https://doi.org/10.1259/dmfr.20140238
30. Peikari M, Salama S, Nofech-Mozes S, Martel AL. A cluster-then-label semi-supervised learning approach for pathology image classification. Sci Rep 2018;8:7193. https://doi.org/10.1038/s41598-018-24876-0
31. Pervaiz K, Cabezas A, Downes K, Santoni BG, Frankle MA. Osteoporosis and shoulder osteoarthritis: incidence, risk factors, and surgical implications. J Shoulder Elbow Surg 2013;22:e1-8. https://doi.org/10.1016/j.jse.2012.05.029
32. Raiss P, Edwards TB, Deutsch A, Shah A, Bruckner T, Loew M, et al. Radiographic changes around humeral components in shoulder arthroplasty. J Bone Joint Surg Am 2014;96:e54. https://doi.org/10.2106/JBJS.M.00378
33. Reeves JM, Athwal GS, Johnson JA. An assessment of proximal humerus density with reference to stemless implants. J Shoulder Elbow Surg 2018;27:641-9. https://doi.org/10.1016/j.jse.2017.09.019
34. Reeves JM, Johnson JA, Athwal GS. An analysis of proximal humerus morphology with special interest in stemless shoulder arthroplasty. J Shoulder Elbow Surg 2018;27:650-8. https://doi.org/10.1016/j.jse.2017.10.029
35. Reeves JM, Vanasse T, Roche C, Athwal GS, Johnson JA, Faber KJ, et al. Regional apparent density correlations within the proximal humerus. JSES Int 2021;5:525-31. https://doi.org/10.1016/j.jseint.2020.12.001
36. Reeves JM, Vanasse T, Roche C, Faber KJ, Langohr GDG. Initial assessments of a Handheld Indentation Probe's correlation with cancellous bone density, Stiffness, and strength: an objective alternative to "Thumb testing". J Med Dev Trans ASME 2021;15:044502. https://doi.org/10.1115/1.4052305
37. Ritter D, Denard PJ, Raiss P, Wijdicks CA, Bachmaier S. Preoperative 3D computed tomography bone density measures provide objective

bone quality classifications for stemless anatomic total shoulder arthroplasty. J Shoulder Elbow Surg 2024;33:1503-11. https://doi.org/10.1016/j.jse.2023.11.005
38. Ritter D, Denard PJ, Raiss P, Wijdicks CA, Bachmaier S. A stemless anatomic shoulder arthroplasty design provides increased cortical medial calcar bone loading in variable bone densities compared to a short stem implant. JSES Int 2024;8:851-8. https://doi.org/10.1016/j.jseint.2024.02.008
39. Roche C, Kumar V, Overman S, Simovitch R, Flurin PH, Wright T, et al. Validation of a machine learning-derived clinical metric to quantify outcomes after total shoulder arthroplasty. J Shoulder Elbow Surg 2021;30:2211-24. https://doi.org/10.1016/j.jse.2021.01.021
40. Sebro R, De la Garza-Ramos C. Opportunistic screening for osteoporosis and osteopenia from CT scans of the abdomen and pelvis using machine learning. Eur Radiol 2023;33:1812-23. https://doi.org/10.1007/s00330-022-09136-0
41. Sebro R, De la Garza-Ramos C. Machine learning for opportunistic screening for osteoporosis from CT scans of the wrist and forearm. Diagnostics (Basel) 2022;12:691. https://doi.org/10.3390/diagnostics12030691
42. Sebro R, De la Garza-Ramos C. Support vector machines are superior to principal components analysis for selecting the optimal bones' CT attenuations for opportunistic screening for osteoporosis using CT scans of the foot or ankle. Osteoporos Sarcopenia 2022;8:112-22. https://doi.org/10.1016/j.afos.2022.09.002
43. Sebro R, Elmahdy M. Machine learning for opportunistic screening for osteoporosis and osteopenia using knee CT scans. Can Assoc Radiol J 2023;74:676-87. https://doi.org/10.1177/08465371231164743
44. Smith ACJ, Tse JJ, Waungana TH, Bott KN, Kuczynski MT, Michalski AS, et al. Internal calibration for opportunistic computed tomography muscle density analysis. PLoS One 2022;17:e0273203. https://doi.org/10.1371/journal.pone.0273203
45. Spross C, Kaestle N, Benninger E, Fornaro J, Erhardt J, Zdravkovic V, et al. Deltoid tuberosity index: a simple radiographic tool to assess local bone quality in proximal humerus fractures. Clin Orthop Relat Res 2015;473:3038-45. https://doi.org/10.1007/s11999-015-4322-x
46. Tabarestani TQ, Levin JM, Warren E, Boadi P, Twomey-Kozak J, Wixted C, et al. Preoperative glenoid bone density is associated with systemic osteoporosis in primary shoulder arthroplasty. Semin Arthroplasty 2023;33:727-34. https://doi.org/10.1053/j.sart.2023.07.006
47. Testa EJ, Albright JA, Lemme NJ, Molla V, McCrae B, Daniels AH, et al. Increased risk of periprosthetic fractures and revision arthroplasty in patients undergoing shoulder arthroplasty with a history of prior Fragility fractures: a matched cohort analysis. J Am Acad Orthop Surg 2023;31:e473-80. https://doi.org/10.5435/JAAOS-D-22-00752
48. Tingart MJ, Apreleva M, von Stechow D, Zurakowski D, Warner JJ. The cortical thickness of the proximal humeral diaphysis predicts bone mineral density of the proximal humerus. J Bone Joint Surg Br 2003;85:611-7. https://doi.org/10.1302/0301-620x.85b4.12843
49. Winsor C, Li X, Qasim M, Henak CR, Pickhardt PJ, Ploeg H, et al. Evaluation of patient tissue selection methods for deriving equivalent density calibration for femoral bone quantitative CT analyses. Bone 2021;143:115759. https://doi.org/10.1016/j.bone.2020.115759

6. Publication II

Citation: Ritter, D.; Raiss, P.; Denard, P.J.; Werner, B.C.; Müller, P.E.; Woiczinski, M.; Wijdicks, C.A.; Bachmaier, S. Volumetric Humeral Canal Fill Ratio Effects Primary Stability and Cortical Bone Loading in Short and Standard Stem Reverse Shoulder Arthroplasty: A Biomechanical and Computational Study. J Imaging 2024, 10, doi:10.3390/jimaging10120334.

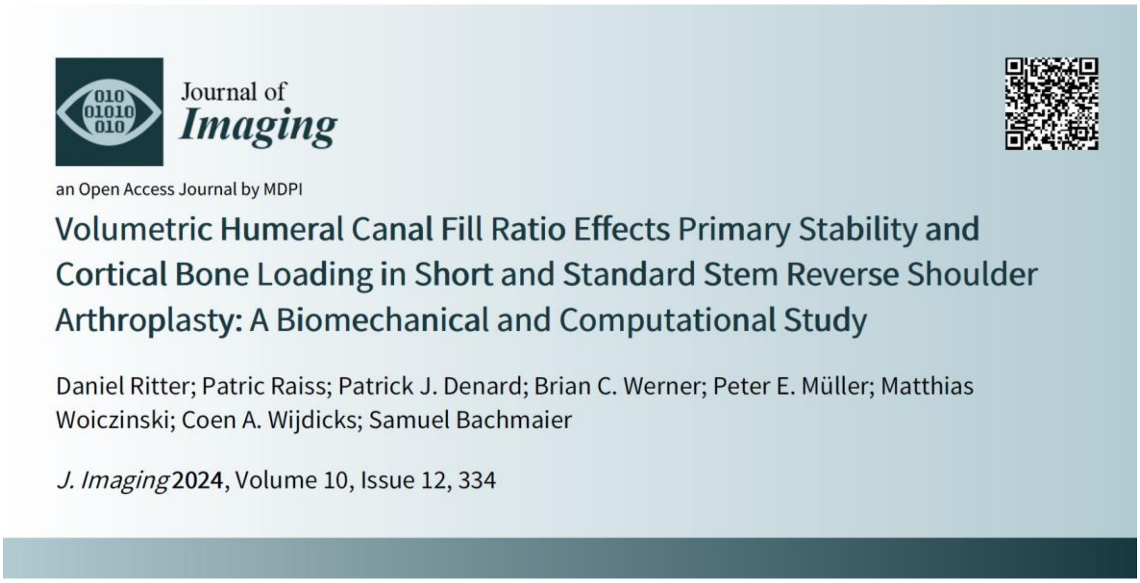
Journal of Imaging
an Open Access Journal by MDPI

Volumetric Humeral Canal Fill Ratio Effects Primary Stability and Cortical Bone Loading in Short and Standard Stem Reverse Shoulder Arthroplasty: A Biomechanical and Computational Study

Daniel Ritter; Patric Raiss; Patrick J. Denard; Brian C. Werner; Peter E. Müller; Matthias Woiczinski; Coen A. Wijdicks; Samuel Bachmaier

J. Imaging **2024**, Volume 10, Issue 12, 334

Journal of Imaging

MDPI

Article

Volumetric Humeral Canal Fill Ratio Effects Primary Stability and Cortical Bone Loading in Short and Standard Stem Reverse Shoulder Arthroplasty: A Biomechanical and Computational Study

Daniel Ritter [1,2,*], Patric Raiss [3], Patrick J. Denard [4], Brian C. Werner [5], Peter E. Müller [2], Matthias Woiczinski [2,6], Coen A. Wijdicks [1] and Samuel Bachmaier [1]

1 Department of Orthopedic Research, Arthrex, 81249 Munich, Germany
2 Department of Orthopaedics and Trauma Surgery, Musculoskeletal University Center Munich (MUM), University Hospital, LMU Munich, 80336 Munich, Germany
3 OCM Clinic, 81369 Munich, Germany
4 Southern Oregon Orthopedics, Medford, OR 97504, USA
5 Department of Orthopaedic Surgery, University of Virginia Health System, Charlottesville, VA 22908, USA
6 Experimental Orthopaedics University Hospital Jena, Campus Eisenberg, Friedrich-Schiller-University, 07607 Eisenberg, Germany
* Correspondence: publications@arthrex.com

Abstract: Objective: This study evaluated the effect of three-dimensional (3D) volumetric humeral canal fill ratios (VFR) of reverse shoulder arthroplasty (RSA) short and standard stems on biomechanical stability and bone deformations in the proximal humerus. Methods: Forty cadaveric shoulder specimens were analyzed in a clinical computed tomography (CT) scanner allowing for segmentation of the humeral canal to calculate volumetric measures which were verified postoperatively with plain radiographs. Virtual implant positioning allowed for group assignment (VFR < 0.72): Standard stem with low (n = 10) and high (n = 10) filling ratios, a short stem with low (n = 10) and high filling ratios (n = 10). Biomechanical testing included cyclic loading of the native bone and the implanted humeral component. Optical recording allowed for spatial implant tracking and the quantification of cortical bone deformations in the proximal humerus. Results: Planned filling ratios based on 3D volumetric measures had a good-to-excellent correlation (ICC = 0.835; p < 0.001) with implanted filling ratios. Lower canal fill ratios resulted in significantly higher variability between short and standard stems regarding implant tilt (820 N: p = 0.030) and subsidence (220 N: p = 0.046, 520 N: p = 0.007 and 820 N: p = 0.005). Higher filling ratios resulted in significantly lower bone deformations in the medial calcar area compared to the native bone, while the bone deformations in lower filling ratios did not differ significantly (p > 0.177). Conclusions: Lower canal filling ratios maintain dynamic bone loading in the medial calcar of the humerus similar to the native situation in this biomechanical loading setup. Short stems implanted with a low filling ratio have an increased risk for implant tilt and subsidence compared to high filling ratios or standard stems.

Keywords: reverse shoulder arthroplasty; short stem; standard stem; CT imaging; canal fill; stress shielding; micromotion; bone deformation; biomechanics

check for updates

Citation: Ritter, D.; Raiss, P.; Denard, P.J.; Werner, B.C.; Müller, P.E.; Woiczinski, M.; Wijdicks, C.A.; Bachmaier, S. Volumetric Humeral Canal Fill Ratio Effects Primary Stability and Cortical Bone Loading in Short and Standard Stem Reverse Shoulder Arthroplasty: A Biomechanical and Computational Study. *J. Imaging* **2024**, *10*, 334. https://doi.org/10.3390/jimaging10120334

Academic Editor: Raimondo Schettini

Received: 11 November 2024
Revised: 13 December 2024
Accepted: 20 December 2024
Published: 23 December 2024

1. Introduction

Reverse shoulder arthroplasty (RSA) with stemmed humeral implants has good long-term results with a low humeral loosening rate, but bone resorption rates remain high [1–3]. Thus, humeral stems have transitioned to short and stemless designs, accepting the risk of reduced primary fixation stability [4–7]. Prior clinical studies have shown a correlation between bone resorption and a high canal fill ratio (FR) of humeral implants [8–11]. Conversely, lower canal fill ratios in short stem RSA are associated with subsidence and varus or valgus malalignment [12]. Initial implant tilt due to reduced mechanical stability was additionally shown to have effects on proximal humeral bone stresses [13]. While thresholds for filling ratios at risk for proximal bone resorption have been defined on plain radiographs (metaphyseal (<0.625) and distal filling ratios (<0.725 and <0.82 depending on metaphyseal ratio)), ref. [14] validation of the distal preoperative measure has shown only moderate predictive accuracy [15]. A three-dimensional (3D) canal fill calculation and its effects on the primary stability and clinical stress shielding may be a valuable tool to increase preoperative planning capabilities.

Related work demonstrated the utility of a volumetric filling ratio (VFR) that was able to predict stress shielding in higher filling ratios more accurately than commonly described two-dimensional filling ratios [16]. Humeral implant primary stability and implant–bone loading patterns vary according to stem type and design and differ from the physiological load transfer patterns in the healthy proximal humerus [13,17]. Finite element analyses (FEA) of stress shielding conditions report a distal load transfer in longer stem lengths, demonstrating the importance of proper stem sizing to achieve a trade-off between adequate primary stability and stress shielding [18–20]. Recent assessments of the primary stability of different canal fills leave potential for improvement as only isolated stem stability and 2D imaging were investigated [21]. Segmentation of the humeral canal anatomy in preoperative 3D CT data may help to objectively select the stem size to reduce the risk of implant subsidence and stress shielding [16,22]. Additionally, investigation of the complete humeral implant in relation to the 3D calculated canal filling ratios may improve the understanding of differing implant–bone load transfer patterns [21,23].

The research questions of this study aimed to evaluate the effect of 3D volumetric humeral canal fill ratios of short and standard RSA stems on biomechanical stability. An analysis of the CT-based bone density and the humeral canal in association with the bone micromotion during cyclic testing allowed us to investigate the hypothesis that increased canal fill ratios provide higher primary stability, with less bone loading in the medial proximal humerus.

2. Materials and Methods

A biomechanical study was performed on 40 cadaveric specimens to evaluate humeral implant stability. Forty cadaveric shoulder specimens (24 male, 16 female; 67 $\pm$ 4 years) were procured (Science Care Inc., Phoenix, AZ, USA). None of the specimens showed macroscopic or radiological signs of humeral or glenohumeral pathologies or anomalies. Prior to biomechanical testing, a 3D analysis of the humeral canal was conducted and used to plan the humeral component size (Figure 1).

Figure 1. Methodical framework, from virtually planning and developing a volumetric measure of the humeral canal which was used in this study for group assignment and planning of low and high filling ratios. Canal fill ratios were controlled using postoperative X-rays after the implantation and before testing the implanted humeral component biomechanically.

2.1. Virtual Planning

The cadaveric shoulders were scanned with a voxel size of 0.5 mm (120 kVp and 80 mA) in a clinical CT scanner (Siemens SOMATOM Definition AS+, Siemens Healthcare GmbH, Erlangen, Germany) to meet the specifications of a current planning software (Virtual Implant Positioning; Arthrex, Inc., Naples, FL, USA). Patient-specific calibration was performed according to previous studies to make these calculations applicable for multicentric standard preoperative CT data [17,24,25]. Gray scale values were converted into bone mineral density (BMD) values by linearly interpolating grayscale values on defined BMD air fat and muscle values [-840, –80 and 30 mgHA/cm^3] to reduce intra- and interscanner inaccuracies. Humeral bone density parameters were evaluated to ensure similar bone density distributions in the treatment groups. According to previous studies, the principal bone density parameters (Epiphysis Cylinder BMD (Epi. Cyl. BMD); Epiphysis Cylinder bone volume per total volume (BV/TV), Metaphysis Cylinder BV/TV, Inferior Support (Inf. Sup.) BMD, and age) were evaluated [17,25]. Morphological parameters of each volume of interest were calculated using pixel-counting methods using the respective bone volume (BV) of the total volume (TV) as BV/TV. Bone model development was performed based on CT voxel data imported as a four-dimensional point cloud (i.e., [x, y, z, mgHA/cm^3]).

2.2. Pre- and Postoperative Canal Fill Analysis

Based on the 3D data, the humeral canal was segmented to calculate volumetric measures after a virtual anatomic humeral head resection according to the surgical technique later performed in the specimen preparation. Standard image processing steps were performed: segmentation of the cortical shell and subtracting it from the whole filled bone resulted in the volumes of interest. The filling ratio calculation in two (2D Metaphysis FR and 2D Diaphysis FR) or three dimensions (3D VFR) was calculated as shown in Figure 2 according to recent clinical studies [14,16]. A commercial CT image processing software (Simpleware ScanIP, Synopsis, Exeter, UK) was used to position the 135° inclined implant virtually with the best-fitting stem and cup size selected (no perforation of the cortical bone). Based on the initial plan, deviating stem and cup sizes were virtually positioned to ensure proper group assignment and implantability for the respective implant types. This resulted in a canal fill ratio range between 0.54 and 0.97.

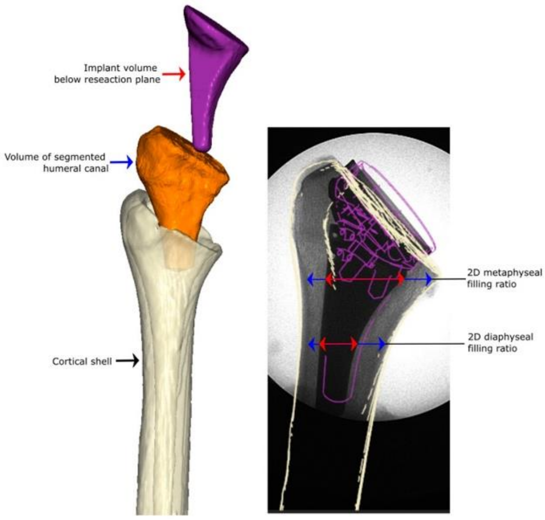

Figure 2. Measurement and calculation of the filling ratios by dividing the red marked measure through the respective blue one. The three-dimensional rendered and segmented CT data on the left side allowed for volumetric calculation of the canal fill ratio (3D VFR). Calculation of the canal fill ratios based on two-dimensional plane radiographs (2D Metaphysis FR and 2D Diaphysis FR) is shown on the right side based on current clinical practice [14,16].

An anterior-posterior (AP) and medial-lateral (ML) X-ray was taken before biomechanical testing to validate the preoperatively (preOP) plan with the actual implanted (postOP) position and filling ratio (Figure 3). After preoperative planning and canal fill calculations (Figure 3A), a 3D-2D registration of the humeral bone was performed using preoperative CT data and postoperative X-ray images (Figure 3B). Potential deviations in varus/valgus, rotation, and translation were analyzed (Figure 3C). Postoperative filling ratio calculations were calculated to verify the match between planned and implanted fill (Figure 3D).

Figure 3. The 2D to 3D registration allowedto validate the accuracy of preoperative canal fill measurements with the actual postoperative implant seating: (**A**). preoperative planning of the humeral implant (purple) and segmentation of the humeral canal (orange), (**B**). registration of postOP X-rays, (**C**). correction of the implant position according to postOP position (blue) and (**D**). calculation of the true postOP canal fill ratio for comparison with the preOP ratio.

2.3. Specimen Grouping and Implantation

Following virtual implant selection, a 135° inlay humeral component available in short or standard lengths was implanted (Univers Revers; Arthrex, Inc., Naples, FL, USA). The low versus high filling ratio was defined at a threshold of 0.72, refs. [14,26] resulting in four groups: a standard stem with low ($\text{Standard}_{\text{low}}$, n = 10) and high ($\text{Standard}_{\text{high}}$, n = 10) filling ratios, a short stem with low (SS_{low}, n = 10), and high filling ratios (SS_{high}, n = 10).

The cadaveric specimens were stored at −20 °C and thawed at room temperature before tissue preparation and testing. The humeral neck was marked using anatomic landmarks before resecting the humeral head along the anatomic neck perpendicular to the metaphyseal axis using an oscillating saw and a 135° cutting guide. The canal was then prepped according to manufacturer specifications, followed by the placement of the planned humeral component. X-rays were taken to confirm the implant seating. Testing was performed at room temperature, and the tissue was kept moist using saline solution throughout the preparation and testing phases.

2.4. Biomechanical Testing

Based on previous biomechanical studies, three levels of load were tested: 220 N, 520 N, and 820 N [24,27–31]. The 220 N load level was applied to mimic 20% body weight (BW) (196 N). The force experienced during rehabilitation arm movements simulates the loading at time-zero after surgery as measured by a telemetric shoulder implant. The 520 N load level was intended to replicate the forces encountered during the initial two months of physical therapy following shoulder arthroplasty, equating to 40% BW (392 N) during resistance training [28]. The highest load level (820 N) simulated peak loads during "normal" use without any weight in hand. As in this rehabilitation phase bone ingrowth already appears, this load level represents a worst-case scenario during rehabilitation. Loads were applied in the coronal plane at a 30° angle from the implant's central axis, as indicated by in vivo measurements [29,30].

Testing of the native bone was performed before humeral component implantation. The humeral head was cyclically loaded using a custom-made polyethylene stamp that matched the humeral head diameter. After humeral component implantation, the PE of the prosthesis was loaded with the matching glenosphere. Native and humeral component testing was performed in the same setup and specimen orientation to allow for comparison of the two loading situations. In both setups, joint contact pressure was simulated for 1000 cycles per load block in force control mode at a frequency of 1.5 Hz (Figure 4A). A ball bearing was included above the stamp to avoid constraining loads. A single-axis material testing machine (ElectroPuls E3000; Instron, Darmstadt, Germany) was used to apply the loads and investigate micromotion and bone deformation at the steady states within the final cycle of each load block using an optical tracking system (Figure 4B).

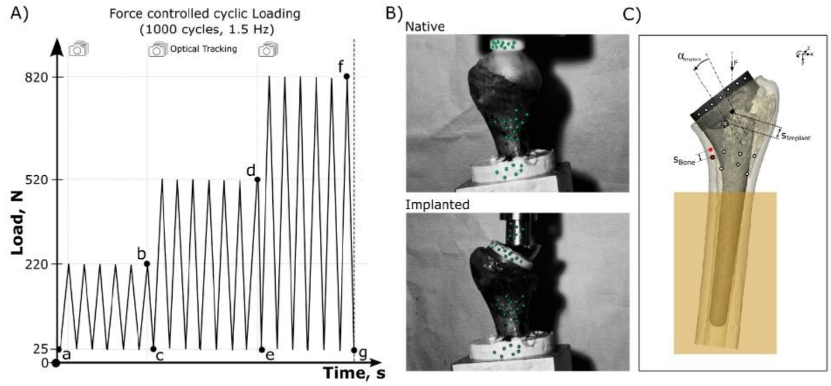

Figure 4. (**A**) Testing protocol shows the loading cycles including the points of data analysis (a–g). (**B**) Experimental cyclic loading setups and the optical tracking points (green) for data analysis. (**C**) Evaluated tracking points during cyclic loading force (F) to analyze implant subsidence and tilt measurements between analysis points a and b, d or f, respectively, (s_{imlant} and α_{imlant}, Δab, Δad, and Δaf) at the end of each loading block. Bone micromotion (s_{BoneHW}, Δbc, Δde, and Δfg) was evaluated as bone displacement within each final load cycle (hysteresis width (HW)). Total compressive transmission caused deformation of the bone was measured at the end of each loading block (s_{BoneTot}, Δab, Δad, and Δaf).

Mechanical data were continuously recorded at a sampling rate of 500 Hz. An optical tracking system (Carl Zeiss GOM Metrology GmbH, Braunschweig, Germany) was used to record the subsidence and tilt of the implant relative to the bone and the deformation and micromotion of the bone relative to the embedding. The optical measurements were captured at a frequency of 30 Hz. Tracking points with a diameter of 0.8 mm were affixed to the embedding, bone, implant, and actuator, which facilitated the correction of rigid body motion in relation to the fixed embedding. Point clouds on the bone were placed in zone 5 of Denard et al. bone resorption classification as bone resorptions were clinically most present in this bone region [9]. The system's dual-camera setup enabled spatial point cloud tracking with an average deviation of 4.9 ± 3.8 µm. Bone deformation was measured on the cortical superficial bone. The differentiation between the relative motion of the implant and the bone was accomplished by assigning different coordinate systems to each component within the optical tracking system.

Cyclic outcome variables (Figure 4A) retrieved from recorded images were compared either with the time-zero reference state (total bone deformation) or assessed during one load hysteresis applied (micromotion). Cyclic outcome variables regarding implant stability (Figure 4C) included implant tilt (α_{imlant}) and subsidence (s_{implant}) at the end of each loading block (220 N, 520 N, and 820 N). The measured bone deformation at the cortical surface during the final load cycle (final hysteresis width (HW)) between valley and peak loading offered insights into dynamic proximal bone loading (Bone micromotion $-$ s_{BoneHW}). Total bone deformation was measured in the medial calcar cortical bone from the time-zero reference image to the end of each loading block (Total bone deformation $-$ s_{BoneTot}). Testing the native and humeral component implanted situation allowed for a comparison of the bone deformation parameters (s_{BoneHW} and $s_{BoneTot}$). The data were analyzed using a commercial software package (Matlab version R2023a, MathWorks, Natick, MA, USA).

2.5. Statistical Analysis

Biomechanical testing outcome metrics were the dependent primary outcome variables. Filling ratio calculations were used as covariates in multivariable regression analyses. Statistical analysis was performed using commercial software (JMP, version 17, JMP Statistical Discovery LLC, Cary, NC, USA).

Intraclass correlation coefficients (ICC) were used to examine the accuracy of the humeral canal fill ratios using a pre- to postoperative comparison. The analysis included a two-way random effects analysis for single measures, and reliability was applied in the context of consistency of a single measure and a single rater. ICCs greater than 0.75 were considered excellent, ICCs of 0.40 to 0.75 indicated moderate reliability, and ICCs of less than 0.40 indicated poor reliability [32,33].

Statistical analyses included one-way analysis of variance (ANOVA) with a Holm–Sidak post hoc test conducted for significant pairwise analysis of the primary outcome variables. A significance level of $p \leq 0.05$ was established. The observed post hoc average power value of all one-way ANOVA tests exceeded the desired power level of 0.8, concluding that the sample size was sufficient. No prior sample size calculation was performed, as no matching mean and standard deviation values were found for our outcome variables and methods. The Shapiro–Wilks and Brown–Forsythe tests confirmed that each dataset represented a normal distribution and equal variance. A non-parametric test (Kruskal–Wallis) was used for datasets that failed these tests. For Kruskal–Wallis tests that found significance, Dunn's post hoc tests including Bonferroni correction were conducted to further analyze the differences.

3. Results

Postoperative X-ray adjusted calculation of the filling ratios demonstrated improved reliability in preoperatively virtual positioned implants for the 3D VFR with an excellent ICC compared to moderate ICCs when using two-dimensional measures (Table 1).

Table 1. Intraclass correlation coefficients (ICC) and confidence intervals (CI) assessing the consistency of the preoperative and postoperative canal fill calculation.

Canal Fill Ratio	ICC * (CI **)	*p*-Value
3D VFR #	0.835 (0.710–0.910)	<0.001
2D Metaphysis FR $	0.569 (0.316–0.746)	<0.001
2D Diaphysis FR $	0.495 (0.220–0.697)	<0.001

* ICC intra class correlation coefficient; ** CI confidence interval; # VFR volumetric filling ratio; $ FR filling ratio.

The groupwise comparison of the canal fill measures resulted in significant differences when using the VFR for both groups and pre- and post-operative measures, while the two-dimensional measures showed a significant difference for the postoperative 2D Diaphysis measure only (Table 2). Specimen distribution (age and gender) did not have an effect on the filling ratio calculation or the bone density. No statistically significant differences were found in bone density and preoperative 2D measures (Table 2).

J. Imaging **2024**, *10*, 334

Table 2. Mean values with standard deviations including statistical analysis of the density variables (BMD Bone Mineral Density; BV/TV Bone Volume/Total Volume) for specimens assigned to the standard or short stem groups with low and high filling ratios, respectively.

Imaging Parameter	Standard $_{Low}$	Standard $_{High}$	*p*-Value	SS$^{\rceil}$ $_{Low}$	SS$^{\rceil}$ $_{High}$	*p*-Value	*p*-Value Standard $_{Low}$ vs. SS$^{\rceil}$ $_{Low}$	*p*-Value Standard $_{High}$ vs. SS$^{\rceil}$ $_{High}$
Age [years]	66± 5	66 ± 5	0.999	66 ± 3	66 ± 4	0.999	0.999	0.999
Number Females	4	5	-	3	4	-	-	-
Epi. Cyl. BMD ** [mgHA/cm^3]	305 ± 39	322 ± 49	0.789	300 ± 49	287 ± 25	0.903	0.991	0.263
Epiphysis Cylinder BV/TV ~	0.31 ± 0.04	0.33 ±0.04	0.542	0.34 ± 0.07	0.31 ± 0.04	0.499	0.333	0.719
Metaphysis Cyl. BV/TV ~	0.21 ± 0.03	0.24 ± 0.03	0.393	0.23 ± 0.04	0.21 ± 0.04	0.742	0.662	0.468
Inf. Sup. BMD ** [mgHA/cm^3]	356 ± 43	355 ± 38	0.999	335 ± 36	325 ± 36	0.929	0.698	0.368
3D VFR$_{PreOP}$ $^{\#}$	0.62 ± 0.06	0.77 ± 0.10	0.003 *	0.62 ± 0.07	0.80 ± 0.10	<0.001 *	0.999	0.814
3D VFR$_{PostOP}$ $^{\#}$	0.65 ± 0.08	0.77 ± 0.11	0.013 *	0.62 ± 0.05	0.82 ± 0.09	<0.001 *	0.925	0.690
2D Metaphysis FR$_{PreOP}$ $^{\$}$	0.62 ± 0.06	0.65 ± 0.05	0.610	0.66 ± 0.06	0.70 ± 0.05	0.404	0.557	0.357
2D Diaphysis FR$_{PreOP}$ $^{\$}$	0.50 ± 0.05	0.52 ± 0.06	0.882	0.49 ± 0.04	0.55 ± 0.05	0.085	0.975	0.570
2D Metaphysis FR$_{PostOP}$ $^{\$}$	0.61 ± 0.05	0.62 ± 0.05	0.991	0.64 ± 0.05	0.63 ± 0.0+	0.965	0.982	0.675
2D Diaphysis FR$_{PostOP}$ $^{\$}$	0.50 ± 0.07	0.52 ± 0.05	0.950	0.49 ± 0.05	0.57 ± 0.07	0.014 *	0.969	0.175

* statistical significance ($p < 0.05$); ** BMD Bone mineral density; ~ BV/TV bone volume per total volume; $^{\#}$ VFR volumetric filling ratio; $^{\$}$ FR filling ratio; $^{\rceil}$ SS short stem.

3.1. Primary Stability

Lower canal fill ratios resulted in significantly higher variability between short and standard stems regarding implant tilt (820 N: $p = 0.030$) and subsidence (220 N: $p = 0.046$, 520 N: $p = 0.007$ and 820 N: $p = 0.005$). Among the short stems, implant subsidence was increased in the low filling ratio group compared to the high filling ratio group in the 820 N block (Figure 5A). The short stems in the low filling ratio group also showed significantly increased implant tilt at 820 N loading compared to standard stemmed implants with a low and high filling ratio (Figure 5B).

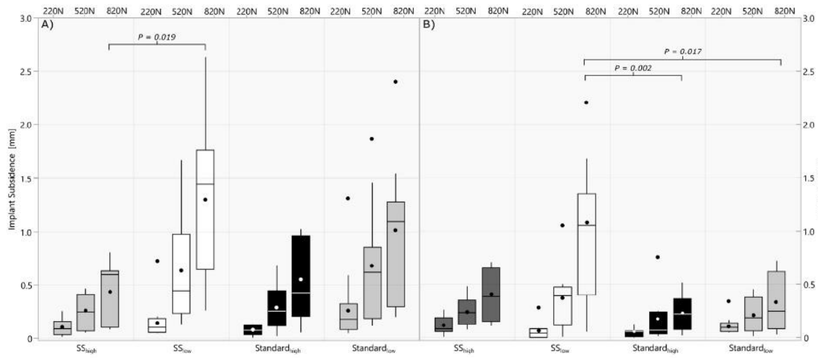

Figure 5. Boxplot of implant subsidence (**A**) and tilt (**B**) at the end of each cyclic loading block (220 N, 520 N, and 820 N) comparing short and standard stem implants, respectively, implanted with high and low filling ratios.

3.2. Bone Loading

No statistical differences in the bone loading variables were found between the short and standard stems with low or high filling ratios ($p > 0.179$), wherefore overall low and high filling ratio groups were compared including standard and short stems (Figure 6). Canal fill ratios across the groups (Range 0.54–0.97) significantly correlated with bone micromotion (220 N: r = 0.55 $p < 0.001$; 520 N: r = 0.52 $p = 0.032$) at lower load levels. Higher filling ratios resulted in significantly lower total bone deformation in the medial calcar area compared to the native bone (Figure 6A), while the total deformation in the lower filling ratio groups did not differ significantly (220 N: $p = 0.374$ 520 N: $p = 0.211$; 820 N: $p = 0.177$). Testing of the native bone showed significantly increased bone micromotion compared to both lower and higher filling ratio groups (Figure 6B).

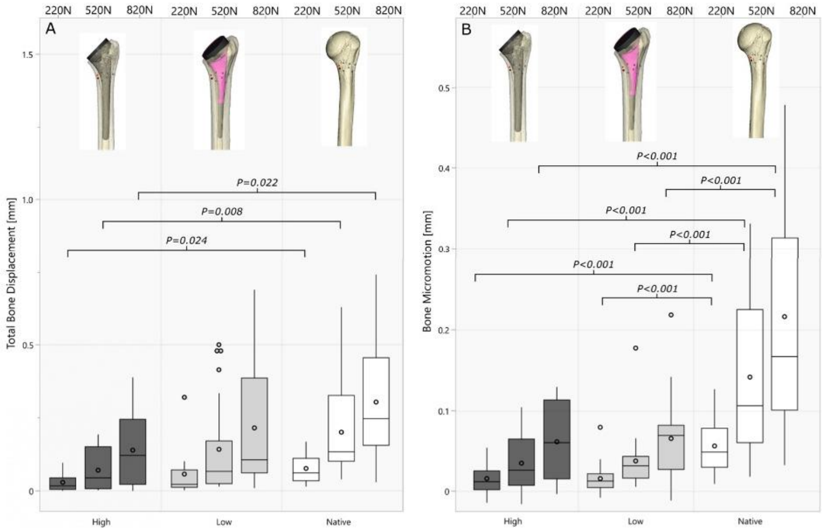

Figure 6. Boxplots of total bone deformation (**A**) and bone micromotion (**B**) for each cyclic loading block (220 N, 520 N, and 820 N) comparing low- and high filling ratios to the biomechanical behavior of the native bone.

4. Discussion

The most important finding of this study was that preoperatively plannable volumetric canal filling ratios have significant effects on the biomechanical behavior of humeral components at the implant–bone interface. Higher humeral canal fill ratios reduced the implant-to-bone loading in the medial calcar bone region compared to the native bone. Lower canal fill ratios approximated the native bone deformations, while short stem implants with canal fill ratios < 0.72 demonstrated a higher risk for implant tilt and subsidence with biomechanical testing. A reliable and accurate method to calculate the preoperative filling ratio was developed explicitly for short and standard stem implants and validated with post-operative X-rays. This 2D to 3D registration was previously shown to allow accurate prediction of stress shielding based on a VFR in a retrospective cohort [14,16]. On the other hand, low filling ratios in RSA were shown to result in increased implant subsidence and tilt [12]. Experimental primary stability and bone deformation data of humeral RSA components for correlation analyses with the humeral canal fill ratio help to understand differing load transfer patterns and the deviations from the native bone loading.

Several studies have demonstrated a correlation between stem length or diameter and higher rates of proximal humerus stress shielding [18,34–37]. However, two-dimensional filling ratios calculated on plain radiographs can be affected by rotation, irregular geometry of the bony anatomy of the humerus, and the geometry of noncylindrical stems, resulting in only moderate accuracy [15]. Therefore, a more robust 3D measurement of the canal volume was used and validated in this work for filling ratio calculation. The application in preoperative CT scans from a standard clinical CT device ensured that the method is universally applicable in a preoperative planning process. The validation of the preoperative calculation using the postoperative position of the implant showed excellent reliability when using 3D models. Increased VFR ICCs (ICC = 0.835) compared to 2D measures (metaphyseal ICC = 0.569 and diaphyseal ICC = 0.495) demonstrate improved preoperative reliability and resulted in an improved separability between all low and high filling ratios and implant types while the 2D measurement only worked for short stem postoperative diaphyseal filling ratios (Table 2). A recent clinical retrospective study using 3D models and 2D postoperative registration in anatomic TSA showed good predictability of proximal humeral stress shielding based on volumetric metaphyseal and diaphyseal filling ratios [16]. The registration of preoperative CT data and postoperative X-rays benefitted our study as the canal fill ratios significantly affected the implant–bone loading and biomechanical device behavior. The increased reversible bone deformation suggests that stimulation can be maintained through the medial calcar region (zones 4 and 5) [9] when using lower filling ratios, which may reduce stress shielding caused bone resorption in this area, as observed clinically with an inlay or cortical rim supporting design [38,39]. Intended osseointegration at the bone–implant interface is closely associated with the mechanical environment of the implant and respective micromotions. Differently maintained mechanical bone loads have been reported to significantly affect bone restoration, especially during the proliferative phase of bone healing [40–42]. To reduce bone resorptions after the healing phase, bone micromotions mimicking the native load absorption pattern are desirable. In our study, the bone deformation measured in the medial calcar area was significantly shielded from load when comparing native and implantation test results. This correlates with clinical findings, as any metal implantation somehow stress shields the bone, even stemless designs result in medial calcar stress shielding [38,39,43,44]. In clinical studies, reduced bone resorption in lower filling ratios correlates with our findings where bone micromotions significantly correlate with the canal fill ratios. A reduction in bone loading significantly decreased the bone micromotion in high canal fill ratios (FR > 0.72) compared to the native bone, which may correlate with the severity of bone resorptions in the clinical setting.

During the application of the postoperatively relevant load levels (220 N, 520 N), the primary stability of lower filling ratios did not differ regarding stem type and filling ratio, similarly as shown in a recent biomechanical study in artificial bone [23]. However, lower filling ratios in combination with short stem implants were more prone to implant tilt and subsidence in increased (post-rehabilitation 820 N) loading. While higher filling ratios and standard stem implants withstood the 820 N load, higher loads during the rehabilitation protocol in lower canal fill ratios may cause earlier migration and tilt that may prevent bone ingrowth [27,45,46]. A recent biomechanical study investigated isolated stem stability and demonstrated significantly increased construct stiffness in +2 mm diameter increased short stems. The increased implant stability in higher filling ratios influenced the loading of the bone due to a more distally shifted implant-to-bone load transfer. Varus/valgus tilt, subsidence, different implant positions in the cancellous bed, and implant design and coatings significantly affect the primary humeral bone stresses [13,21,47–49]. Particularly the implant design used in this study, the flushlay design using a cup in the cancellous bed, contributes significantly to the primary stability and load transfer in the proximal humerus [50]. Therefore, the planning and inclusion of the cup size below the resection plane helped to determine the true volumetric filling ratio relevant to finding the trade-off between stress shielding and primary stability aiming for a ratio of 0.72, while still allowing adaption of the filling ratio. The adaption of implant sizes could help to gain a higher primary stability in poor bone densities where a final size prediction with the inclusion of bone density variables may pay off to patient-specifically find the most adequate implant sizes. Especially the volumetric canal fill ratio is more robust when adapting stem sizes, as the full construct humeral component is considered, compared to only two specific planes in 2D methods. However, the effects of differing implant designs on primary stability and bone adaptions during rehabilitation can be affected by other biological factors that influence bone formation or resorption [34,35,51].

While the effects of the preoperative evaluable bone density on biomechanical implant behavior have already been demonstrated, [17,24] this study showed significant effects of preoperatively calculated volumetric canal fill ratios on the primary stability and implant–bone loading. Both may influence primary implant stability after shoulder arthroplasty surgery, wherefore we controlled for an equal bone density distribution in the groups to reduce the impact of variable specimen age and gender between the groups and focus on the investigation of differing canal fill ratios. The impact of in vivo biologics such as the effects of bone ingrowth (secondary fixation) and stress shielding cannot be reproduced biomechanically, but the comparative findings of a native and implantation test setup help to understand potential causes for stress shielding and implant subsidence. Preoperative canal fill calculation allows to accurately determine the intended stem size to improve the planning process between the risk of stress shielding and limited implant stability.

There are some limitations to the current study. Bony adaptions which affect secondary stability in clinical applications, cannot be investigated in cadaveric biomechanical testing. Therefore, this study's stability and bone loading results may behave differently in an in vivo setting over a more extended follow-up period. The effect of different implant designs, coatings, varying abduction angles as well as the micromotions in cancellous bone to promote bone ingrowth is a pertinent question beyond the scope of this study. The findings of this work may differ for onlay or inlay humeral component designs. The comparison of the combined groups of short and standard stems in the bone loading investigations can be improved to find bone loading differences between the stem length in specific filling ratios, maybe in an FE analysis. The usage of a short and standard stemmed implant using the same metaphyseal design allowed for the comparison to the native bone when applying low and high filling ratios. Volumetric canal fill ratio calculations were postoperatively verified; however, other deviations to preoperative planning (varus/valgus) may affect bone loading and subsidence patterns, which should be investigated accordingly. Additionally, the volume ratio only provides information on the implant and canal sizes without considering the influences associated with differing shapes and anatomies which may have an additional impact on the primary stability. An axial compression load vector was applied at a fixed angle to simulate the compressive loading of the humeral component. The test setup and method in this biomechanical study only roughly simulate the in vivo loading, and the implant may clinically behave differently. However, the findings using these implants showed the effects of stem and cup sizing on primary stability in a time-zero setting to show different load transfer patterns in an experimental biomechanical study. To overcome these limitations, the application of the volumetric filling ratio in preoperative planning should be studied in a prospective clinical setting. This approach may provide important information when comparing the biomechanical behavior of future stemless humeral RSA components to stemmed implants.

5. Conclusions

Both short and standard-length stem RSA humeral components implanted with a low canal filling ratio maintain dynamic bone loading in the medial calcar of the humerus similar to the native bone tested in this loading setup. However, the implantation of shorter stems with a lower filling ratio increased the risk of time-zero implant tilt and subsidence. In contrast, higher filling ratios or standard stems implanted with low or high filling ratios demonstrated higher primary stability, especially in higher daily peak loads (820 N). Volumetric preoperative canal fill calculations are more reliable than 2D calculations in planar radiographs.

Author Contributions: Conceptualization, D.R., P.R. and S.B.; Data curation, D.R.; Formal analysis, D.R.; Investigation, D.R.; Methodology, D.R. and M.W.; Project administration, D.R. and C.A.W.; Resources, C.A.W. and S.B.; Software, D.R.; Supervision, D.R., C.A.W. and S.B.; Validation, D.R., P.R., P.J.D., B.C.W., P.E.M. and M.W.; Visualization, D.R.; Writing—original draft, D.R.; Writing—review and editing, D.R., P.R., P.J.D., B.C.W., P.E.M., M.W., C.A.W. and S.B. All authors have read and agreed to the published version of the manuscript.

Funding: Investigation performed at Arthrex, Department of Orthopedic Research. Arthrex provided full support of this study (Study No. AIRR-00608-118).

Institutional Review Board Statement: Not applicable.

Informed Consent Statement: Not applicable.

Data Availability Statement: Dataset available on request from the authors.

Conflicts of Interest: D.R. is an employee of Arthrex. P.R. receives consulting fees and honoraria from Arthrex, receives support for travel to meetings for the study or other purposes from Arthrex. P.D. receives consulting fees and honoraria from Arthrex, receives support for travel to meetings for the study or other purposes from Arthrex, and receives royalties from Arthrex. B.W. receives consulting fees and honoraria from Arthrex, Pacira and Lifenet, receives research support from Arthrex, Zimmer Biomet, Exactech, Pacira and Lifenet and receives support for travel to meetings for the study or other purposes from Arthrex. M.W. declares no conflicts of interests. C.W. is an employee of Arthrex. P.E.M. receives consulting fees and honoraria from BBraun Aesculap and Medacta and the affiliated research institute receives research support from Arthrex. There were no financial payments or other benefits related to the subject of this article. S.B. is an employee of Arthrex.

References

1. Esfandiari, A.; Hamoodi, Z.; Newton, A.; Nixon, M.; Webb, M.; Kenyon, P. The incidence of humeral bone resorption in uncemented reverse shoulder arthroplasty and the impact on functional outcomes. *Semin. Arthroplast. JSES* **2022**, *32*, 638–643. [CrossRef]
2. Inoue, K.; Suenaga, N.; Oizumi, N.; Yamaguchi, H.; Miyoshi, N.; Taniguchi, N.; Morita, S.; Munemoto, M.; Kurata, S.; Tanaka, Y. Humeral bone resorption after reverse shoulder arthroplasty using uncemented stem. *JSES Int.* **2020**, *4*, 138–143. [CrossRef] [PubMed]
3. Sanchez-Sotelo, J. Current Concepts in Humeral Component Design for Anatomic and Reverse Shoulder Arthroplasty. *J. Clin. Med.* **2021**, *10*, 5151. [CrossRef] [PubMed]
4. Testa, E.J.; Albright, J.A.; Lemme, N.J.; Molla, V.; McCrae, B.; Daniels, A.H.; Paxton, E.S. Increased Risk of Periprosthetic Fractures and Revision Arthroplasty in Patients Undergoing Shoulder Arthroplasty With a History of Prior Fragility Fractures: A Matched Cohort Analysis. *J. Am. Acad. Orthop. Surg.* **2023**, *31*, e473–e480. [CrossRef] [PubMed]
5. ASES Complications of RSA Multicenter Research Group; Mahendraraj, K.A.; Abboud, J.; Armstrong, A.; Austin, L.; Brolin, T.; Entezari, V.; Friedman, L.; Garrigues, G.E.; Grawe, B.; et al. Predictors of acromial and scapular stress fracture after reverse shoulder arthroplasty: A study by the ASES Complications of RSA Multicenter Research Group. *J. Shoulder Elb. Surg.* **2021**, *30*, 2296–2305. [CrossRef] [PubMed]
6. Bernatz, J.T.; Brooks, A.E.; Nguyen, B.P.; Shin, E.D.; Binkley, N.C.; Anderson, P.A.; Grogan, B.F. Prevalence and Treatment of Osteoporosis Prior to Elective Shoulder Arthroplasty. *J. Am. Acad. Orthop. Surg. Glob. Res. Rev.* **2020**, *4*, e20.00204. [CrossRef] [PubMed]
7. Ackland, D.C.; Patel, M.; Knox, D. Prosthesis design and placement in reverse total shoulder arthroplasty. *J. Orthop. Surg. Res.* **2015**, *10*, 101. [CrossRef]
8. Casagrande, D.J.; Parks, D.L.; Torngren, T.; Schrumpf, M.A.; Harmsen, S.M.; Norris, T.R.; Kelly, J.D., 2nd. Radiographic evaluation of short-stem press-fit total shoulder arthroplasty: Short-term follow-up. *J. Shoulder Elb. Surg.* **2016**, *25*, 1163–1169. [CrossRef] [PubMed]
9. Denard, P.J.; Raiss, P.; Gobezie, R.; Edwards, T.B.; Lederman, E. Stress shielding of the humerus in press-fit anatomic shoulder arthroplasty: Review and recommendations for evaluation. *J. Shoulder Elb. Surg.* **2018**, *27*, 1139–1147. [CrossRef]
10. Nagels, J.; Stokdijk, M.; Rozing, P.M. Stress shielding and bone resorption in shoulder arthroplasty. *J. Shoulder Elb. Surg.* **2003**, *12*, 35–39. [CrossRef]
11. Spormann, C.; Durchholz, H.; Audigé, L.; Flury, M.; Schwyzer, H.K.; Simmen, B.R.; Kolling, C. Patterns of proximal humeral bone resorption after total shoulder arthroplasty with an uncemented rectangular stem. *J. Shoulder Elb. Surg.* **2014**, *23*, 1028–1035. [CrossRef] [PubMed]
12. Tross, A.K.; Ladermann, A.; Wittmann, T.; Schnetzke, M.; Nolte, P.C.; Collin, P.; Raiss, P. Subsidence of Uncemented Short Stems in Reverse Shoulder Arthroplasty-A Multicenter Study. *J. Clin. Med.* **2020**, *9*, 3362. [CrossRef]
13. Tavakoli, A.; Spangenberg, G.; Reeves, J.M.; Faber, K.J.; Langohr, G.D.G. Humeral short stem varus-valgus alignment affects bone stress. *J. Orthop. Res.* **2022**, *40*, 2169–2178. [CrossRef] [PubMed]
14. Kramer, M.; Olach, M.; Zdravkovic, V.; Manser, M.; Raiss, P.; Jost, B.; Spross, C. The effects of length and width of the stem on proximal humerus stress shielding in uncemented primary reverse total shoulder arthroplasty. *Arch. Orthop. Trauma. Surg.* **2024**, *144*, 633–672. [CrossRef]
15. Raiss, P.; Wittmann, T.; Blakeney, W.; Urvoy, M.; Walch, G. Validation of the distal filling ratio in uncemented convertible short-stem shoulder arthroplasty. *Arch. Orthop. Trauma. Surg.* **2023**, *143*, 1833–1839. [CrossRef]
16. Celik, H.; Chauhan, A.; Flores-Hernandez, C.; D'Lima, D.; Hoenecke, H. Three-dimensional Volumetric Filling Ratio Predicts Stress Shielding in Short-stem Anatomic Total Shoulder Arthroplasty. *J. Am. Acad. Orthop. Surg.* **2020**, *28*, 1047–1054. [CrossRef] [PubMed]
17. Ritter, D.; Denard, P.J.; Raiss, P.; Wijdicks, C.A.; Bachmaier, S. Preoperative 3-dimensional computed tomography bone density measures provide objective bone quality classifications for stemless anatomic total shoulder arthroplasty. *J. Shoulder Elb. Surg.* **2024**, *33*, 1503–1511. [CrossRef]

18. Razfar, N.; Reeves, J.M.; Langohr, D.G.; Willing, R.; Athwal, G.S.; Johnson, J.A. Comparison of proximal humeral bone stresses between stemless, short stem, and standard stem length: A finite element analysis. *J. Shoulder Elb. Surg.* **2016**, *25*, 1076–1083. [CrossRef] [PubMed]
19. Reeves, J.M.; Langohr, G.D.G.; Athwal, G.S.; Johnson, J.A. The effect of stemless humeral component fixation feature design on bone stress and strain response: A finite element analysis. *J. Shoulder Elb. Surg.* **2018**, *27*, 2232–2241. [CrossRef] [PubMed]
20. Roberto, P.; Helen, I.; Mohammad, N.J.; Kristine, I.; Jashint, M.; Sarah, L.W.; Kenneth, C.; Ashish, G. The hybrid humerus reverse shoulder arthroplasty: A prospective study of bone grafting and metaphyseal fixation with undersized stem in the assessment of proximal humeral stress shielding and associated clinical outcome. *Semin. Arthroplast. JSES* **2024**, *34*, 797–806. [CrossRef]
21. Reeves, J.M.; Spangenberg, G.W.; Elwell, J.A.; Stewart, B.; Vanasse, T.; Roche, C.; Faber, K.J.; Langohr, G.D.G. Implications of humeral short-stem diametral sizing on implant stability. *JSES Int.* **2023**, *7*, 2445–2453. [CrossRef] [PubMed]
22. Kazumasa, T.; Hiromu, I. Association between the canal filling ratio and bone resorption in trabecular metal stems in reverse total shoulder arthroplasty: A radiographic analysis using tomosynthesis. *JSES Int.* **2024**, *8*, 1077–1086. [CrossRef]
23. Galteri, G.; Montanari, S.; Dozza, G.; Palanca, M.; Cristofolini, L. Short humeral stem in total shoulder arthroplasty does not jeopardize primary implant stability. *JSES Int.* **2024**, *in press*. [CrossRef]
24. Ritter, D.; Denard, P.J.; Raiss, P.; Wijdicks, C.A.; Bachmaier, S. A Stemless Anatomic Shoulder Arthroplasty Design Provides Increased Cortical Medial Calcar Bone Loading in Variable Bone Densities Compared to a Short Stem Implant. *JSES Int.* **2024**, *8*, 851–858. [CrossRef]
25. Ritter, D.; Denard, P.J.; Raiss, P.; Wijdicks, C.A.; Werner, B.C.; Bedi, A.; Bachmaier, S. Machine Learning Models Can Define Clinically Relevant Bone Density Sub-groups based on Patient Specific Calibrated CT Scans in Patients Undergoing Reverse Shoulder Arthroplasty. *J. Shoulder Elb. Surg.* **2024**, *ahead of print*. [CrossRef] [PubMed]
26. Freislederer, F.; Moroder, P.; Audige, L.; Schneller, T.; Ameziane, Y.; Trefzer, R.; Imiolczyk, J.P.; Scheibel, M. Analysis of three different reverse shoulder arthroplasty designs for cuff tear arthropathy—The combination of lateralization and distalization provides best mobility. *BMC Musculoskelet. Disord.* **2024**, *25*, 204. [CrossRef] [PubMed]
27. Favre, P.; Seebeck, J.; Thistlethwaite, P.A.; Obrist, M.; Steffens, J.G.; Hopkins, A.R.; Hulme, P.A. In vitro initial stability of a stemless humeral implant. *Clin. Biomech.* **2016**, *32*, 113–117. [CrossRef]
28. Bergmann, G.; Graichen, F.; Bender, A.; Kaab, M.; Rohlmann, A.; Westerhoff, P. In vivo glenohumeral contact forces--measurements in the first patient 7 months postoperatively. *J. Biomech.* **2007**, *40*, 2139–2149. [CrossRef]
29. Bergmann, G.; Graichen, F.; Bender, A.; Rohlmann, A.; Halder, A.; Beier, A.; Westerhoff, P. In vivo gleno-humeral joint loads during forward flexion and abduction. *J. Biomech.* **2011**, *44*, 1543–1552. [CrossRef]
30. Westerhoff, P.; Graichen, F.; Bender, A.; Halder, A.; Beier, A.; Rohlmann, A.; Bergmann, G. In vivo measurement of shoulder joint loads during activities of daily living. *J. Biomech.* **2009**, *42*, 1840–1849. [CrossRef] [PubMed]
31. Chen, R.E.; Knapp, E.; Qiu, B.; Miniaci, A.; Awad, H.A.; Voloshin, I. Biomechanical comparison of stemless humeral components in total shoulder arthroplasty. *Semin. Arthroplast. JSES* **2022**, *32*, 145–153. [CrossRef]
32. McGraw, K.O.; Wong, S.P. Forming inferences about some intraclass correlation coefficients. *Psychol. Methods* **1996**, *1*, 30–46. [CrossRef]
33. Koo, T.K.; Li, M.Y. A Guideline of Selecting and Reporting Intraclass Correlation Coefficients for Reliability Research. *J. Chiropr. Med.* **2016**, *15*, 155–163. [CrossRef]
34. Denard, P.J.; Noyes, M.P.; Walker, J.B.; Shishani, Y.; Gobezie, R.; Romeo, A.A.; Lederman, E. Proximal stress shielding is decreased with a short stem compared with a traditional-length stem in total shoulder arthroplasty. *J. Shoulder Elb. Surg.* **2018**, *27*, 53–58. [CrossRef] [PubMed]
35. Raiss, P.; Edwards, T.B.; Deutsch, A.; Shah, A.; Bruckner, T.; Loew, M.; Boileau, P.; Walch, G. Radiographic changes around humeral components in shoulder arthroplasty. *J. Bone Jt. Surg. Am.* **2014**, *96*, e54. [CrossRef]
36. Vegas, A.; Cannon, D.; Lewis, S.; Glener, J.; Mekkawy, K.L.; Rodriguez, H.C.; Schodlbauer, D.F.; Levy, J.C. Impact of humeral stem length on calcar resorption in anatomic total shoulder arthroplasty. *J. Shoulder Elb. Surg.* **2024**, *33*, 130–138. [CrossRef] [PubMed]
37. Stijn, G.C.J.; Philipp, K.; Alexandra, S.V.; Stefan, K.; Mazda, F.; Karl, W.; Florian, G. The effect of humeral diaphyseal stem filling ratio on clinical and radiological outcome. *Semin. Arthroplast. JSES* **2024**, *34*, 340–347. [CrossRef]
38. Alikhah, A.; Imiolczyk, J.P.; Krukenberg, A.; Scheibel, M. Screw fixation in stemless shoulder arthroplasty for the treatment of primary osteoarthritis leads to less osteolysis when compared to impaction fixation. *BMC Musculoskelet. Disord.* **2020**, *21*, 295. [CrossRef]
39. Aibinder, W.R.; Uddin, F.; Bicknell, R.T.; Krupp, R.; Scheibel, M.; Athwal, G.S. Stress shielding following stemless anatomic total shoulder arthroplasty. *Shoulder Elb.* **2023**, *15*, 54–60. [CrossRef]
40. Bailón-Plaza, A.; Marjolein, C.H. Beneficial effects of moderate, early loading and adverse effects of delayed or excessive loading on bone healing. *J. Biomech.* **2003**, *36*, 1069–1077. [CrossRef]
41. Barcik, J.; Epari, D.R. Can Optimizing the Mechanical Environment Deliver a Clinically Significant Reduction in Fracture Healing Time? *Biomedicines* **2021**, *9*, 691. [CrossRef]
42. Ulstrup, A.K. Biomechanical concepts of fracture healing in weight-bearing long bones. *Acta Orthop. Belg.* **2008**, *74*, 291–302. [PubMed]
43. Greis, M.; Heubach, K.; Hoberg, M.; Irlenbusch, U. Proximal humeral bone loss in stemless shoulder arthroplasty: Potential factors influencing bone loss and a new classification system. *Arch. Orthop. Trauma. Surg.* **2023**, *143*, 3085–3090. [CrossRef]

44. Churchill, R.S. Stemless shoulder arthroplasty: Current status. *J. Shoulder Elb. Surg.* **2014**, *23*, 1409–1414. [CrossRef]
45. Peppers, T. Fixation of humeral prostheses and axial micromotion. *J. Shoulder Elb. Surg.* **1998**, *7*, 414–418. [CrossRef] [PubMed]
46. Pilliar, R.M.; Lee, J.M.; Maniatopoulos, C. Observations on the effect of movement on bone ingrowth into porous-surfaced implants. *Clin. Orthop. Relat. Res.* **1986**, *208*, 108–113. [CrossRef]
47. Goñalons-Giol, F.; Ventura-Parellada, C.; Gàmez-Baños, F.; Mora-Guix, J.M. Stress shielding: Short-term radiological results of the reverse shoulder arthroplasty with an anatomic proximal coated stem in proximal humeral fractures. *Arch. Orthop. Trauma. Surg.* **2024**, *144*, 783–790. [CrossRef]
48. Synnott, S.; Langohr, G.D.G.; Reeves, J.M.; Johnson, J.A.; Athwal, G.S. The effect of humeral implant thickness and canal fill on interface contact and bone stresses in the proximal humerus. *JSES Int.* **2021**, *5*, 881–888. [CrossRef] [PubMed]
49. Humphrey, C.S.; Bravman, J.T. A Method to Facilitate Improved Positioning of a Reverse Prosthesis Stem During Arthroplasty Surgery: The Metaphyseal-centering Technique. *Tech. Shoulder Elb. Surg.* **2018**, *19*, 67–74. [CrossRef]
50. Colasanti, C.A.; Mercer, N.P.; Contreras, E.; Simovitch, R.W.; Zuckerman, J.D. Reverse shoulder arthroplasty design—Inlay vs. onlay: Does it really make a difference? *J. Shoulder Elb. Surg.* **2024**, *33*, 2073–2085. [CrossRef]
51. Sandberg, O.H.; Aspenberg, P. Inter-trabecular bone formation: A specific mechanism for healing of cancellous bone. *Acta Orthop.* **2016**, *87*, 459–465. [CrossRef]

7. Publication III

Citation: Ritter, D.; Raiss, P.; Denard, P.J.; Werner, B.C.; Kistler, M.; Lesnicar, C.; van der Merwe, M.; Müller, P.E.; Woiczinski, M.; Wijdicks, C.A.; et al. Reverse Shoulder Arthroplasty Baseplate Stability Is Affected by Bone Density and the Type and Amount of Augmentation. Bioengineering 2025, 12, 42.

bioengineering

an Open Access Journal by MDPI

Reverse Shoulder Arthroplasty Baseplate Stability Is Affected by Bone Density and the Type and Amount of Augmentation

Daniel Ritter; Patric Raiss; Patrick J. Denard; Brian C. Werner; Manuel Kistler; Celina Lesnicar; Micheal van der Merwe; Peter E. Müller; Matthias Woiczinski; Coen A. Wijdicks; Samuel Bachmaier

Bioengineering 2025, Volume 12, Issue 1, 42 bioengineering

MDPI

Article

Reverse Shoulder Arthroplasty Baseplate Stability Is Affected by Bone Density and the Type and Amount of Augmentation

Daniel Ritter [1,2,*], Patric Raiss [3], Patrick J. Denard [4], Brian C. Werner [5], Manuel Kistler [2], Celina Lesnicar [2], Micheal van der Merwe [1], Peter E. Müller [2], Matthias Woiczinski [2,6], Coen A. Wijdicks [1] and Samuel Bachmaier [1]

1 Department of Orthopedic Research, Arthrex, 81249 Munich, Germany
2 Department of Orthopaedics and Trauma Surgery, Musculoskeletal University Center Munich (MUM), University Hospital, LMU Munich, 80336 Munich, Germany
3 OCM Clinic, 81369 Munich, Germany
4 Southern Oregon Orthopedics, Medford, OR 97504, USA
5 Department of Orthopaedic Surgery, University of Virginia Health System, Charlottesville, VA 22908, USA
6 Experimental Orthopaedics University Hospital Jena, Campus Eisenberg, Friedrich-Schiller-University, 07607 Eisenberg, Germany
* Correspondence: publications@arthrex.com

Abstract: Objective: This study evaluated the effects of bony increased offset (BIO) and metallic augments (MAs) on primary reverse shoulder arthroplasty (RSA) baseplate stability in cadaveric specimens with variable bone densities. Methods: Thirty cadaveric specimens were analyzed in an imaging and biomechanical investigation. Computed tomography (CT) scans allowed for preoperative RSA planning and bone density analysis. Three correction methods of the glenoid were used: (1) corrective reaming with a standard baseplate, which served as the reference group ($n = 10$); (2) MA-RSA ($n = 10$); and (3) angled BIO-RSA ($n = 10$). Each augment group consisted of 10° ($n = 5$) and 20° ($n = 5$) corrections. Biomechanical testing included cyclic loading in an articulating setup, with optical pre- and post-cyclic micromotion measurements in a rocking horse setup. Results: There were no differences in bone density between groups based on CT scans ($p > 0.126$). The BIO-RSA group had higher variability in micromotion compared to the MA-RSA and reference groups ($p = 0.013$), and increased total micromotion compared to the reference group ($p = 0.039$). Both augmentations using 20° corrections had increased variance in rotational stability compared to the reference group ($p = 0.043$). Micromotion correlated with the subchondral bone density in the BIO-RSA group ($r = -0.63$, $p = 0.036$), but not in the MA-RSA ($p > 0.178$) or reference ($p > 0.117$) groups. Conclusions: Time-zero baseplate implant fixation is more variable with BIO-RSA and correlates with bone density. Corrections of 20° with either augmentation approach increase variability in rotational micromotion. The preoperative quantification of bone density may be useful before utilizing 20° of correction, especially when adding a bone graft in BIO-RSAs.

Keywords: reverse shoulder arthroplasty; preoperative bone density; CT imaging; augment; baseplate; primary fixation; BIO-RSA

check for updates

Academic Editors: Stuart Goodman and Alvaro N. Gurovich

Received: 12 November 2024
Revised: 6 December 2024
Accepted: 6 January 2025
Published: 8 January 2025

Citation: Ritter, D.; Raiss, P.; Denard, P.J.; Werner, B.C.; Kistler, M.; Lesnicar, C.; van der Merwe, M.; Müller, P.E.; Woiczinski, M.; Wijdicks, C.A.; et al. Reverse Shoulder Arthroplasty Baseplate Stability Is Affected by Bone Density and the Type and Amount of Augmentation. *Bioengineering* **2025**, *12*, 42. https://doi.org/10.3390/bioengineering12010042

1. Introduction

Reverse shoulder arthroplasty (RSA) is an effective treatment for shoulder pathologies, including osteoarthritis and rotator cuff deficiency [1]. The first RSA designs medialized the center of rotation (COR). However, high rates of scapular notching and limited rotational range of motion led to implant modifications. One of the major adjustments was glenoid-sided lateralization. Shifting the COR laterally compared to earlier designs lowered the risk of bony impingement [2–4]. However, lateralization increases stress at the baseplate–glenoid interface.

From a technical perspective, it is advised to avoid a superior tilt of the glenoid baseplate to maximize stability. Given the concavity of the glenoid, correction of the RSA angle is necessary to achieve appropriate baseplate contact. While inferior reaming is an option, this approach can require extensive bone removal and lead to medialization. Alternatively, correction of the RSA angle with the maintenance of bone stock and net lateralization can be achieved with either bone grafts (bony increased offset (BIO)) or metal augments (MAs) [1,5–9]. Notably, increased lateralization in combination with poor bone density may compromise primary implant fixation [10–12] and increase complications, with significant effects on long-term patient outcomes [13–17]. Prior studies have suggested that computed tomography (CT) scans used for preoperative planning may provide valuable information about bone density [18–20]. Biomechanical data comparing baseplate stability and micromotion with BIO- or MA-RSA are lacking [21–23]. The effects of bone density and amount of RSA angle correction on time-zero baseplate fixation can improve preoperative data to optimize surgical decision-making.

The purpose of this study was to compare the time-zero implant micromotion of BIO-RSA and MA-RSA with different amounts of inclination correction in relation to preoperatively analyzable glenoid bone density. It was hypothesized that BIO-RSAs would have decreased time-zero stability compared to MA-RSAs, particularly with increased correction and lower bone density.

2. Materials and Methods

A biomechanical investigation was performed on 30 cadaveric shoulder specimens. All specimens (mean age 71.9 ± 11.9 years; 13 females and 17 males) were scanned in a clinical CT scanner for surgical planning, followed by bone density and glenoid morphology assessments. Specimens were assigned into three groups, including two treatment groups with augmentation and one reference group without augmentation. The treatment groups included n = 10 MAs and n = 10 angled BIO-RSAs. Preoperative planning allowed the assignment of five specimens with 10° correction and five specimens with 20° correction to each treatment group (Figure 1).

2.1. Bone Density

Bone density parameters were extracted from scans performed in a standard clinical CT scanner (Siemens SOMATOM Definition AS+, Siemens Healthcare GmbH, Erlangen, Germany) with a voxel resolution of 0.6 × 0.6 × 0.6 mm. Patient-specific calibration was performed according to previous studies to make this bone density analysis applicable to multicentric standard preoperative CT data [18,19,24]. Grayscale values were converted into bone mineral density (BMD) values by linearly interpolating grayscale values on defined BMD air fat and muscle values [−840, −80 and 30 mgHA/cm^3]. The morphological parameter (BV/TV) calculation of each VOI was based on pixel-counting methods using the respective bone volume (BV) of the total volume (TV).

Regions of Interest

Global volumes of interest (VOIs) included the glenoid bone portion (Figure 2). Regions of interest were evaluated along the scapular axis, through the root of the scapular spine and the middle point of the glenoid. Regions of interest relevant for implant stability included a subchondral and glenoid vault cylinder (Figure 2). The diameter of both cylinders was defined as 50% of the 3 to 9 o'clock glenoid distance measured at the articular surface. The depth of the glenoid vault cylinder was defined as up until one endpoint of the cylinder reached the medial cortex. The subchondral cylinder depth was determined using one-third of the glenoid vault cylinder, starting medially to the articulating cortex below necrotic bone tissue. All regions of interest were cropped to use the pixel information, using a global segmentation threshold for consistent bone density extraction (Figure 2).

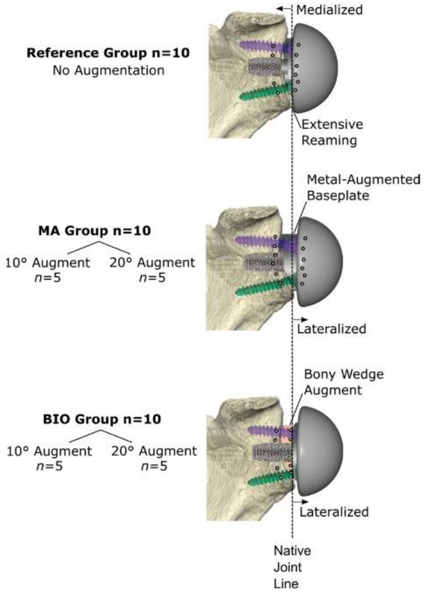

Figure 1. Group assignment of the specimen based on virtually planned reverse shoulder arthroplasty. Bone density analysis and biomechanical testing for the reference, metal augment (MA) and bony increased offset (BIO) groups, which consisted of (n = 5) 10° and 20° augmentation, respectively. The compression screws in the inferior position are shown by green screws with locking screws (purple) in the superior position.

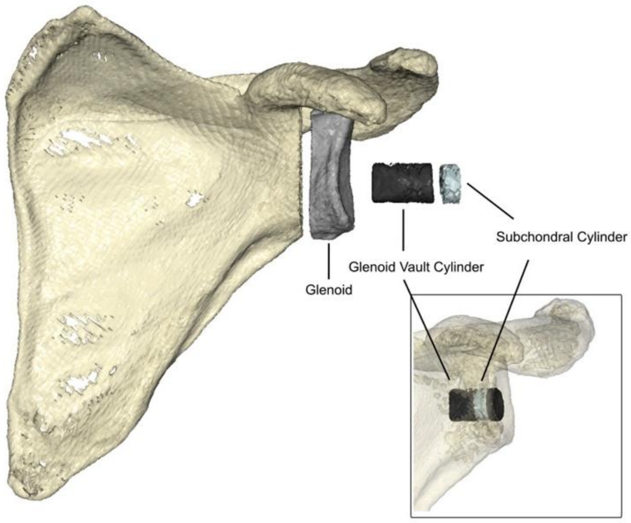

Figure 2. Evaluation of the bone density in the respective regions of interest: glenoid, cylindrical glenoid vault, and subchondral cylinder, demonstrated in three three-dimensionally rendered CT images.

2.2. Virtual Planning and Surgical Technique

Specimens (Science Care Inc., Phoenix, AZ, USA) were stored at −20 °C and thawed at room temperature for at least 24 h before tissue preparation and testing. CT imaging-based preoperative planning was performed using a commercially available three-dimensional preoperative planning software (Virtual Implant Positioning version 8.1.0, Arthrex; Naples, FL, USA). A 24 mm circular baseplate (Modular Glenoid System; Arthrex; Naples, FL, USA) was positioned 3 mm superior to the inferior glenoid rim in all specimens. Implantation was planned to achieve 5° of implant retroversion and a 0° RSA angle. This defined the degree (10° or 20°) of full-wedge augmentation. The correct wedge orientation was achieved by slightly rotating the implant around its axis to reach the minimum baseplate or bone graft contact area threshold of 80%. Extensive bone reaming was necessary for the non-augmented reference group to provide 0° inclination and 5° retroversion. Minimal reaming was performed in the glenoids planned for either BIO- or MA-RSA augmentation. All cases (n = 30) were planned and corrected to a 0° RSA angle and 5° retroversion with the augment that demonstrated the least amount of reaming. The specimens were then assigned into the following groups: 10° BIO (n = 5), 10° MA (n = 5), 20° BIO (n = 5), 20° MA (n = 5), and Reference (n = 10). The bone and metal augmentations were planned in the same manner, as a bone grafting instrument set allowed for the reproducible preparation of the respective grafts.

All the baseplates were placed using a reusable patient-specific guide (Glenoid Targeter; Arthrex, Naples, FL, USA) to ensure replication of the planned position. The central baseplate post and peripheral screws were implanted in a bicortical fashion using the respective screw and post length. The post length anchoring in the native glenoid was consistent for all groups (BIO: 26 ± 4 mm; MA: 24 ± 5 mm; Reference: 26 ± 4 mm). The screws consisted of a non-locking compression screw in the inferior position and three more locking screws, which were kept consistent for all groups. Standard glenospheres were used without additional lateralization or inferiorization, and the diameter was defined according to the plan to achieve a 3 mm inferior overhang. The amount of lateral offset was defined by the degree of augmentation. The 10° and 20° augmentations resulted in an additional 2.1 mm and 4.4 mm of lateral offset, respectively (Figure 1). To achieve the 0° inclination and 5° retroversion in the reference group, additional glenoid reaming resulted in 2.1 to 4.4 mm medialization of the COR in reference to the native joint line [25,26].

2.3. Biomechanical Testing

Biomechanical testing was developed in accordance with the ASTM F2028-17 testing standard [27]. The testing procedure was conducted in two phases, in two custom test setups (Figure 3). Shear and compression loads were applied in a biaxial rocking-horse setup, while measuring the displacement of the glenoid baseplate (setup A). Cyclic rotation of the glenoid component was performed in an articulation simulator (setup B) to simulate shoulder abduction. Following the articular cyclic loading, the displacement of the glenoid baseplate was recorded again in setup A using the same shear and compressive loading setup. All specimens were embedded centrally in an aluminum pot using polyurethane resin (RenCast® FC 52/53 Isocyanate and FC 53 Polyol, Huntsman Advanced Materials (Europe) BV, Everberg, Belgium). The articulating surface of the glenosphere component was carefully aligned horizontally, and the embedding material was filled to a level at a safe distance from the implant or screws.

For setup A, the specimens were mounted on the biaxial testing setup (Figure 3). The load was applied via a humeral polyethylene component matching the glenosphere size, fixed in a universal testing machine (Instron ElectroPuls E10000, Norwood, MA, USA) with a six-component load cell (MCS10-010-6C, Baldwin Messtechnik GmbH, Darmstadt, Germany). A constant compressive load of 430 N was applied through the COR of the joint, perpendicular to the glenoid plane, while the specimens were moved cyclically along the superior–inferior axis, parallel to the glenoid plane, using a linear actuator (RK DuoLine S 80, Phoenix Mecano, Stein am Rhein, Switzerland) for a reproducible shear force application of 350 N, with a frequency of 1/6 Hz, for 25 load cycles (Figure 3). In accordance with the ASTM standard, the measuring frequency did not exceed 200 N/s.

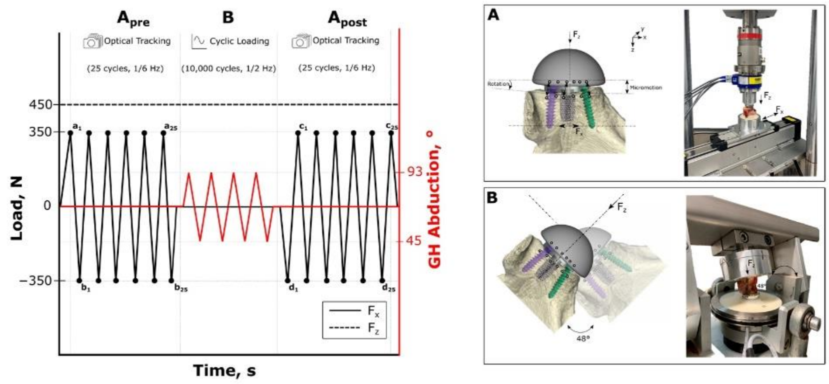

Figure 3. Test protocol and phases of the two test setups (**left**): phase (**A**): shear (Fx) and compressive loading (Fz), with definition of the measurement of outcome variables before (pre, mean Δa_1b_1 to $\Delta a_{25}b_{25}$) and after (post, mean Δc_1d_1 to $\Delta c_{25}d_{25}$) fatigue testing; phase (**B**): fatigue testing with cyclic abduction under compressive loading (Fz) in two experimental setups (**right**), setup A: biaxial rocking-horse setup for shear and compressive loading during micromotion detection, and setup B: articulation simulator for implant loosening.

In setup B, the embedded specimens were clamped into the articulation simulator (Figure 3). All the reverse glenoid components were cyclically rotated from 45° to 93° (a total of 48°) of abduction around the matching humeral polyethylene component. A total of 10,000 load cycles, with a compressive load of 430 N, were applied, at a frequency of 0.5 Hz.

2.4. Outcome Variables

Primary stability was defined as micromotion at the implant–glenoid interface (Figure 3). To assess the primary stability of the glenoid implants, the spatial displacement of the glenoid component was recorded pre- and post-cyclically during the rocking-horse-tests (setup A) using an optical measuring system (Aramis, 3D Camera 2.3M, Carl Zeiss GOM Metrology, Oberkochen, Germany), with a frequency of 5 Hz for 25 cycles. The camera configuration ensured a measuring volume of 140 mm × 90 mm × 90 mm and a measuring accuracy of 2.8 μm within and 5.6 μm outside of the focus plane. For motion detection, six measuring points were fixed to the surface of the glenosphere and the glenoid rim, and, if applicable, to the bony augment (Figure 3). Micromotion was calculated as the relative displacement between the glenoid rim and the glenosphere. Rotational displacement resulted from two lines extending from the first to the last measuring point on the glenosphere and the glenoid, respectively. Rotational displacement and micromotion were analyzed as the mean minimum to maximum values of each shear load cycle before (pre, mean Δa_1b_1 to $\Delta a_{25}b_{25}$) and after (post, mean Δc_1d_1 to $\Delta c_{25}d_{25}$) fatigue testing (Figure 3). For the BIO group, the bone graft was separately tracked optically to quantify the percentages of graft–glenoid and implant–graft micromotion, respectively. The outcome data of the implant–bone interface analysis included pre- and post-cyclic rotation and micromotion and the respective evaluated pre-to-post-cyclic differences.

2.5. Statistical Analysis

The biomechanical testing outcome metrics were the dependent primary outcome variables. Bone density variables were defined as secondary outcome variables. Correlation analysis was performed between primary and secondary outcome variables using Pearson's correlation coefficients. Statistical analysis was performed using commercial software (Sigma Plot Statistics for Windows, version 13.0, Systat Software, San Jose, CA, USA).

The statistical analysis comprised a one-way ANOVA with a Holm–Sidak post hoc test, conducted for a significant pairwise analysis of the primary outcome variables. Significance was defined as $p \leq 0.05$. The observed post hoc average power value of all the one-way ANOVA tests exceeded the desired power level of 0.8, confirming that the sample size was sufficient. No prior sample size calculation was performed, as no matching mean and standard deviation values were found for our outcome variables and methods. Shapiro–Wilks and Brown–Forsythe tests confirmed that each data set adhered to a normal distribution and equal variance, respectively. For data sets that failed these tests, a non-parametric test (Kruskal–Wallis) was used for non-normal-distributed data sets. For Kruskal–Wallis tests that found significance, Dunn's post hoc tests, including Bonferroni correction, were conducted to further analyze the differences.

3. Results

There were no differences in bone density (Table 1) between the two treatment and reference groups for comparisons in Figures 4 and 5 or the groups assigned based on type and amount of augmentation ($p > 0.126$), as shown in Figure 6.

Table 1. Mean values with standard deviations of density variables (BMD—bone mineral density; BV/TV—bone volume/total volume) for specimens assigned to reference, metal augment (MA), and bony increased offset (BIO) groups, including statistical analysis.

Bone Density Variables	MA	BIO	Reference	MA vs. BIO *p*-Value	MA vs. Ref. *p*-Value	BIO vs. Ref. *p*-Value
Subchondral Cylinder BMD [mgHA/cm^3]	217 ± 34	211 ± 16	238 ± 37	0.905	0.256	0.121
Glenoid Cylinder [mgHA/cm^3]	409 ± 49	385 ± 32	397 ± 57	0.515	0.837	0.852
Glenoid Global [mgHA/cm^3]	371 ± 58	347 ± 30	386 ± 35	0.447	0.697	0.121
Subchondral Cylinder BV/TV	0.62 ± 0.15	0.59 ± 0.18	0.66 ± 0.14	0.906	0.820	0.568
Glenoid Cylinder BV/TV	0.72 ± 0.13	0.69 ± 0.11	0.73 ± 0.12	0.811	0.987	0.722
Glenoid Global BV/TV	0.78 ± 0.13	0.73 ± 0.11	0.80 ± 0.10	0.548	0.976	0.426

BIO baseplate fixation resulted in a higher variability in micromotion compared to the MA-RSA and reference groups ($p = 0.013$), and increased total micromotion ($p = 0.039$) compared to the reference group (Figure 4). The micromotion in the BIO-RSA group had a similar percentage of displacement at the implant–graft (53 ± 14%) and the graft–glenoid interfaces (47 ± 16%), resulting in similar micromotion to that of the reference and MA groups. Micromotion in the MA-RSA ($p > 0.178$) and reference ($p > 0.117$) groups did not correlate significantly with bone density, while a significant correlation with subchondral bone density (cylindrical BV/TV) was found for the BIO group ($r = -0.63$, $p = 0.036$).

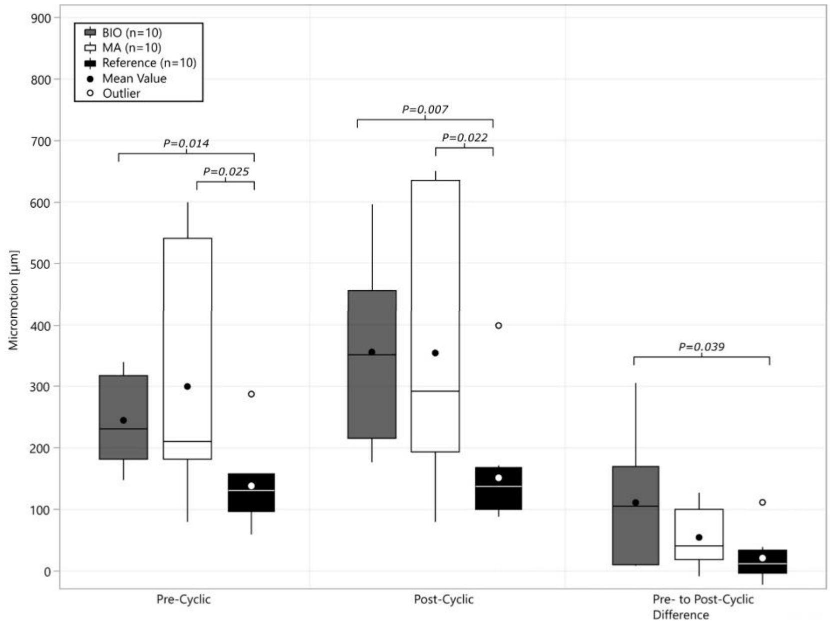

Figure 4. Boxplot with mean and median overall cyclic micromotion before (pre-) and after (post-) cyclic loading. Micromotion added through cyclic loading is quantified as pre- to post-cyclic difference.

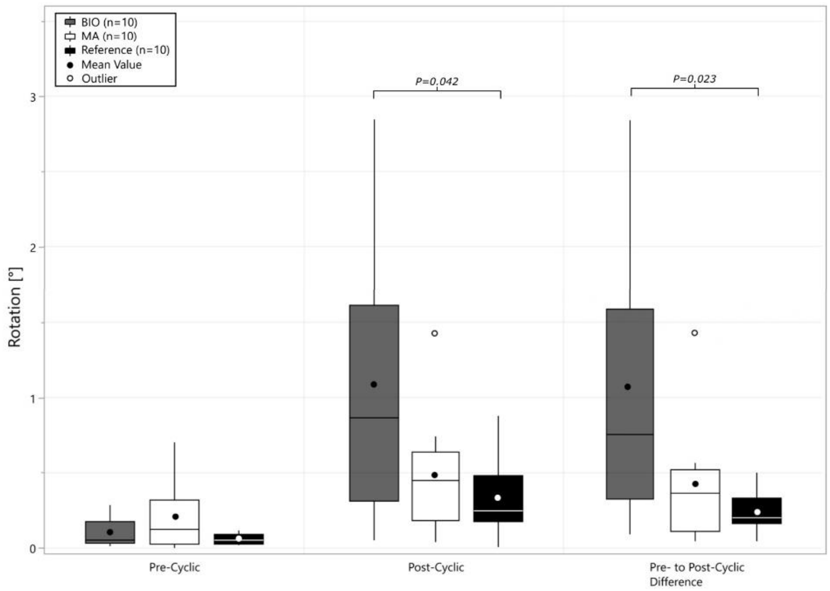

Figure 5. Boxplot with mean and median overall rotational displacement before (pre-) and after (post-) cyclic loading, and quantified difference. Rotation added through cyclic loading is quantified as pre- to post-cyclic difference.

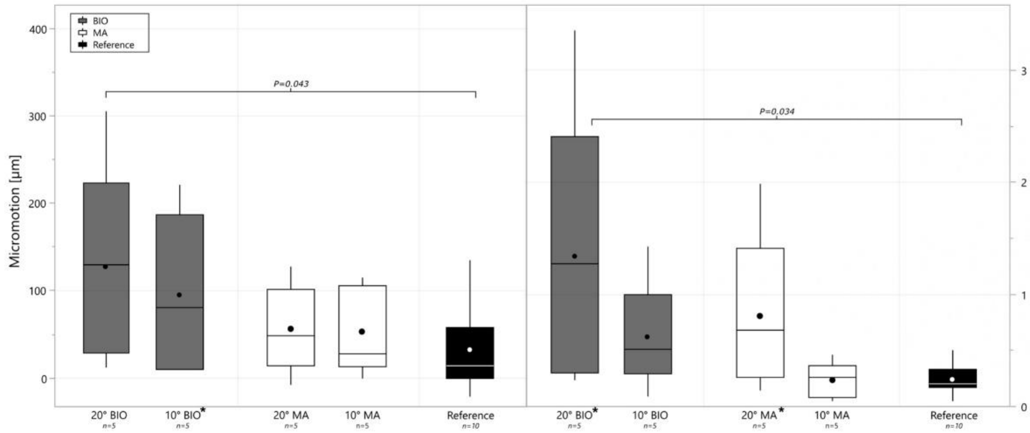

Figure 6. Boxplot with mean and median difference, quantifying micromotion from pre- to post-cyclic change in micromotion (**left**) and rotational displacement (**right**), divided per degree and type of augmentation. Group names marked with asterisks showed significantly increased variance compared to reference group.

In the pre-/post-cyclic comparison (Figure 5) of the rotational displacement, the BIO-RSA group had higher variability than the MA and reference groups ($p < 0.033$), and increased micromotion compared to the reference group (Figure 5, $p = 0.023$).

As is visible in Figure 6, both augmentation approaches resulted in significantly higher rotational fixation variability ($p = 0.034$) when using 20° of correction. The 10° BIO-RSA correction group had increased variance in micromotion compared to the reference group ($p = 0.043$), and the 20° BIO-RSA group had significantly higher micromotion and rotational displacement than the reference group (Figure 6).

4. Discussion

The most important findings of this study are that time-zero implant–bone micromotion of an RSA glenoid baseplate is affected by (1) the method of angular correction (bone versus metal), (2) the amount of angular correction, and (3) variability in bone density. BIO-RSA baseplate stability was more variable with increased micromotion and rotational displacement. Implant micromotion when using angled BIO-RSA was also correlated with glenoid subchondral bone density, with a higher degree of RSA angle correction (20°) resulting in increased variability in rotational stability compared to MAs. While the impact of micromotion on bone resorption and clinical outcomes remains to be determined, assessment of glenoid bone density with preoperative CTs may be a helpful tool to screen the bone density for informed decision-making regarding metal or bone as a means of angular deformity correction during RSA.

The long-term bone graft behavior of BIO-RSA procedures may be related to the mechanical environment, and there is a risk of graft resorption, which may influence clinical outcomes due to implant loosening and scapular notching [9,28,29]. The clinical importance of graft fixation is currently undergoing discussion, as the 5-year survival rate is reliable, and anchoring the baseplate without a graft behind has also been reported to have positive outcomes (the "stilting" technique) [30]. However, it can be difficult to precisely control the intended bony wedge size due to both graft preparation and potential compression during implantation. Experienced surgeons may not be challenged by preparing and implanting the graft reproducibly; however, MAs reduce the graft variables and achieve the desired contact area through glenoid preparation.

Considering the micromotion at the interfaces of the BIO-RSA constructs separately (the glenoid–graft and implant–graft interfaces), the respective micromotions were in a similar range as for the MA and reference groups, which may indicate clinically reliable healing rates with BIO-RSA as well as with MAs [31,32]. However, the significant correlation with bone density in the BIO-RSA group and the addition of an interface between the bony augment and the baseplate explain the higher variability and the overall increase in micromotion. Undefined bone graft compression due to varying fixation techniques and bone densities may be reasons for the clinical appearances of stress shielding, implant loosening, and scapular notching [9,28,29]. Thus, MAs may be preferred, particularly in patients with poor bone quality, as less variable fixation stability when using these implants did not correlate with the bone density. Generally, high degrees of lateralization or large augment angles should be applied carefully in patients with poor bone densities to achieve adequate primary fixation. Notably, higher fixation variability was found in our study when using 20° augments, regardless of the bone density and augment type utilized.

In revision scenarios or highly retroverted and inclined glenoids, healed autologous bone grafts enable bone preservation or even bone formation in patients needing long-term or revisable joint reconstructions. The in vivo biological effects on autologous bone healing are unclear, and cannot be reproduced biomechanically; however, this study showed significant differences between current implant types according to varying bone densities. The CT-based planning and investigation of primary fixation for variable bone densities may benefit the surgeon in terms of implant selection and fixation. The proposed bone density evaluation and applicability in clinical CT scans allows objective preoperative bone density classification, with a significant impact on time-zero implant stability, treatment, and stress shielding in RSA patients [17,24]. Biomechanical studies on primary augmented baseplate stability are rare, and focus on ex vivo models in artificial bone or finite element analyses. The results from previous studies are similar to our findings, with increased stresses in bony augments and higher degrees of lateralization [21–23]. Our study bridges the gap to the clinical situation by using standard clinical preoperative CT scans of cadaveric specimens and an articulating loading setup. The results in an artificial bone substitute are viable as confounders can be reduced, but they significantly deviate from measurements in cadaveric bone [23]. The subject-specific evaluation of preoperative plans for respective treatments, including bone density, therefore increase the clinical relevance of our study. The articulating test setup used in this study represents the most similar conditions to an in vivo situation available in the current literature. Rehabilitation-relevant load levels and standardized pre- and post-cyclic micromotion measurements allowed us to analyze the effects of in vivo-like cyclic loading on implant micromotion. Micromotion did not exceed the 150 μm limit for osseointegration [10–12] in the pre- to post-cyclic observations, except for in BIO-RSA constructs with poor bone densities, which exceeded this value slightly. In a clinical use case, patients below a specified bone density threshold could be detected, who are at risk for greater micromotions. Adaption of the surgical technique to reduce undefined graft compression states could be a consequence of preoperative risk stratification. For example, machine learning models could be used for clearer detection to give suitable recommendations for patients with poor bone density [18,19].

Other factors may influence the fixation of the baseplate and the behavior of an augment [33]. One biomechanical study recommended that the surgical technique may be modified according to the patient's bone density and necrotic bone regions [34]. Constant refinement of preoperative evaluation models by adding and optimizing parameters is necessary to handle the multifactorial nature of shoulder reconstructions and their complications. The patient-specific calibration method in our study helped to reduce inaccuracies due to intra- and interscanner variations, and to make bone density analyses applicable in a multicentric context [35,36]. The concept proposed in this study, using systematically mapped bone densities in the glenoid, demonstrates promising value for its inclusion in CT-based preoperative planning, but it may still need to be validated for everyday clinical application [37]. While aseptic glenoid loosening is rare, complication rates remain increased in patients with poor bone density [17]. With an aging population and the common performance of glenoid lateralization in RSA, the preoperative identification of patients with low bone density may have implications for treatment approaches. The implementing implantation-relevant bone density parameters (subchondral (below potential necrosis) and glenoid vault cylinder) showed the highest level of interaction with implant stability in the BIO-RSA procedure. Both treatments remain valid options, but preoperative bone quality assessment may pay off by offering better preoperative knowledge in surgeons' decision processes and potentially improving patient outcomes [20,38,39].

There are several limitations to the current study that are important to acknowledge. Bony ingrowth, which provides secondary anchorage in clinical applications, could not be accounted for in the cadaveric specimens. The in vivo stability and the load transfer of the investigated implants may behave differently over a more extended follow-up period. The biological effects and the ability of different implant types and designs to promote bone ingrowth are pertinent questions beyond this study's scope. Nevertheless, the findings of this work determine the primary stability of BIO- and MA-RSA before bone ingrowth, and provide insight into primary implant behavior in an experimental biomechanical study. Cyclic loading in an articulating setup allowed for the simulation of glenohumeral abduction, but did not address variable in vivo shoulder joint loading and variable rotational and shear forces. Our findings are limited to a modular glenoid baseplate using standardized augmentation; multiplanar and severe defects should be researched in future studies. Patient-specific calibration may not have been necessary for this study, as all the specimens were scanned in one scanner with the same settings, but it may help in applying the bone density model multicentrically [40]. The comparison of multicentric scans and their subsequent validation with density phantoms represent future research questions.

5. Conclusions

Time-zero baseplate implant fixation is more variable with BIO-RSA and correlates with bone density. Corrections of 20° with either augmentation approach increase variability in rotational micromotion. The preoperative quantification of bone density may be useful before utilizing 20° of correction, especially when adding a bone graft in BIO-RSAs.

Author Contributions: Conceptualization, D.R., P.R. and S.B.; Data curation, D.R., C.L. and M.K.; Formal analysis, D.R., C.L. and M.K.; Investigation, D.R., C.L. and M.K.; Methodology, D.R., C.L., M.K. and M.W.; Project administration, D.R., M.v.d.M., C.L., M.K. and C.A.W.; Resources, M.v.d.M., C.A.W. and S.B.; Software, D.R., C.L., M.K.; Supervision, D.R., C.A.W. and S.B.; Validation, D.R., P.R., P.J.D., B.C.W., P.E.M. and M.W.; Visualization, D.R. and C.L.; Writing—original draft, D.R., C.L. and M.K.; Writing—review & editing, D.R., P.R., P.J.D., B.C.W., C.L., M.K., P.E.M., M.W., M.v.d.M., C.A.W. and S.B. All authors have read and agreed to the published version of the manuscript.

Funding: Investigation performed at the Department of Orthopaedics and Trauma Surgery, Musculoskeletal University Center Munich (MUM), University Hospital, LMU Munich, Germany. Arthrex provided full support of this study (Study No. AIRR-00608-119).

Institutional Review Board Statement: Not applicable.

Informed Consent Statement: Not applicable.

Data Availability Statement: Dataset available on request from the authors.

Conflicts of Interest: D.R. is an employee of Arthrex. P.R. receives consulting fees and honoraria from Arthrex, and receives support for travel to meetings for studies or other purposes from Arthrex. P.J.D. receives consulting fees and honoraria from Arthrex, receives support for travel to meetings for studies or other purposes from Arthrex, and receives royalties from Arthrex. B.C.W. receives consulting fees and honoraria from Arthrex, Pacira, and Lifenet, receives research support from Arthrex, Zimmer Biomet, Exactech, Pacira, and Lifenet and receives support for travel to meetings for studies or other purposes from Arthrex. M.K. declares no conflicts of interests. C.L. declares no conflicts of interests. M.v.d.M. is an employee of Arthrex. M.W. declares no conflicts of interests. C.A.W. is an employee of Arthrex. P.E.M. receives consulting fees and honoraria from BBraun Aesculap and Medacta, and the affiliated research institute receives research support from Arthrex. There were no financial payments or other benefits related to the subject of this article. S.B. is an employee of Arthrex.

References

1. Bacle, G.; Nové-Josserand, L.; Garaud, P.; Walch, G. Long-Term Outcomes of Reverse Total Shoulder Arthroplasty: A Follow-up of a Previous Study. *J. Bone Joint Surg. Am.* **2017**, *99*, 454–461. [CrossRef] [PubMed]
2. Berhouet, J.; Garaud, P.; Favard, L. Evaluation of the role of glenosphere design and humeral component retroversion in avoiding scapular notching during reverse shoulder arthroplasty. *J. Shoulder Elbow Surg.* **2014**, *23*, 151–158. [CrossRef]
3. Levigne, C.; Boileau, P.; Favard, L.; Garaud, P.; Mole, D.; Sirveaux, F.; Walch, G. Scapular notching in reverse shoulder arthroplasty. *J. Shoulder Elb. Surg.* **2008**, *17*, 925–935. [CrossRef] [PubMed]
4. Werthel, J.D.; Walch, G.; Vegehan, E.; Deransart, P.; Sanchez-Sotelo, J.; Valenti, P. Lateralization in reverse shoulder arthroplasty: A descriptive analysis of different implants in current practice. *Int. Orthop.* **2019**, *43*, 2349–2360. [CrossRef]
5. Boileau, P.; Moineau, G.; Roussanne, Y.; O'Shea, K. Bony Increased-offset Reversed Shoulder Arthroplasty: Minimizing Scapular Impingement While Maximizing Glenoid Fixation. *Clin. Orthop. Relat. Res.®* **2011**, *469*, 2558–2567. [CrossRef] [PubMed]
6. Boileau, P.; Morin-Salvo, N.; Bessière, C.; Chelli, M.; Gauci, M.-O.; Lemmex, D.B. Bony increased-offset–reverse shoulder arthroplasty: 5 to 10 years' follow-up. *J. Shoulder Elb. Surg.* **2020**, *29*, 2111–2122. [CrossRef] [PubMed]
7. Dimock, R.; Fathi Elabd, M.; Imam, M.; Middleton, M.; Godenèche, A.; Ali Narvani, A. Bony increased-offset reverse shoulder arthroplasty: A meta-analysis of the available evidence. *Shoulder Elb.* **2021**, *13*, 18–27. [CrossRef] [PubMed]
8. Imiolczyk, J.-P.; Audigé, L.; Harzbecker, V.; Moroder, P.; Scheibel, M. Metallic humeral and glenoid lateralized implants in reverse shoulder arthroplasty for cuff tear arthropathy and primary osteoarthritis. *JSES Int.* **2022**, *6*, 221–228. [CrossRef]
9. Merolla, G.; Giorgini, A.; Bonfatti, R.; Micheloni, G.M.; Negri, A.; Catani, F.; Tarallo, L.; Paladini, P.; Porcellini, G. BIO-RSA vs. metal-augmented baseplate in shoulder osteoarthritis with multiplanar glenoid deformity: A comparative study of radiographic findings and patient outcomes. *J. Shoulder Elb. Surg.* **2023**, *32*, 2264–2275. [CrossRef] [PubMed]
10. Favre, P.; Seebeck, J.; Thistlethwaite, P.A.; Obrist, M.; Steffens, J.G.; Hopkins, A.R.; Hulme, P.A. In vitro initial stability of a stemless humeral implant. *Clin. Biomech.* **2016**, *32*, 113–117. [CrossRef] [PubMed]
11. Peppers, T. Fixation of humeral prostheses and axial micromotion. *J. Shoulder Elb. Surg.* **1998**, *7*, 414–418. [CrossRef] [PubMed]
12. Pilliar, R.M.; Lee, J.M.; Maniatopoulos, C. Observations on the effect of movement on bone ingrowth into porous-surfaced implants. *Clin. Orthop. Relat. Res.* **1986**, *208*, 108–113. [CrossRef]
13. Harmer, L.; Throckmorton, T.; Sperling, J.W. Total shoulder arthroplasty: Are the humeral components getting shorter? *Curr. Rev. Musculoskelet. Med.* **2016**, *9*, 17–22. [CrossRef] [PubMed]
14. Kumar, S.; Sperling, J.W.; Haidukewych, G.H.; Cofield, R.H. Periprosthetic Humeral Fractures After Shoulder Arthroplasty. *J. Bone Joint Surg. Am.* **2004**, *86*, 680–689. [CrossRef] [PubMed]
15. Nagels, J.; Stokdijk, M.; Rozing, P.M. Stress shielding and bone resorption in shoulder arthroplasty. *J. Shoulder Elb. Surg.* **2003**, *12*, 35–39. [CrossRef] [PubMed]
16. Raiss, P.; Edwards, T.B.; Deutsch, A.; Shah, A.; Bruckner, T.; Loew, M.; Boileau, P.; Walch, G. Radiographic changes around humeral components in shoulder arthroplasty. *J. Bone Jt. Surg. Am.* **2014**, *96*, e54. [CrossRef]
17. Casp, A.J.; Montgomery, S.R.J.; Cancienne, J.M.; Brockmeier, S.F.; Werner, B.C. Osteoporosis and Implant-Related Complications After Anatomic and Reverse Total Shoulder Arthroplasty. *J. Am. Acad. Orthop. Surg.* **2020**, *28*, 121–127. [CrossRef] [PubMed]
18. Ritter, D.; Denard, P.J.; Raiss, P.; Wijdicks, C.A.; Bachmaier, S. Preoperative 3-dimensional computed tomography bone density measures provide objective bone quality classifications for stemless anatomic total shoulder arthroplasty. *J. Shoulder Elb. Surg.* **2024**, *33*, 1503–1511. [CrossRef]

19. Ritter, D.; Denard, P.J.; Raiss, P.; Wijdicks, C.A.; Werner, B.C.; Bedi, A.; Müller, P.E.; Bachmaier, S. Machine Learning Models Can Define Clinically Relevant Bone Density Sub-groups based on Patient Specific Calibrated CT Scans in Patients Undergoing Reverse Shoulder Arthroplasty. *J. Shoulder Elb. Surg.* **2024**. *Epub ahead of printing*. [CrossRef]
20. Hayden, A.; Cotter, E.J.; Hennick, T.; Hetzel, S.; Wollaeger, J.; Anderson, S.; Grogan, B.F. Bone Quality in Total Shoulder Arthroplasty: A Prospective Study Correlating CT Hounsfield Units with Thumb Test and FRAX Score. *JSES Int.* **2023**, *7*, 628–635. [CrossRef]
21. Martin, E.J.; Duquin, T.R.; Ehrensberger, M.T. Reverse Total Shoulder Arthroplasty Baseplate Stability in Superior Bone Loss with Augmented Implant. *J. Shoulder Elb. Arthroplast.* **2021**, *5*, 24715492211020689. [CrossRef] [PubMed]
22. Smith, A.F.; Frankle, M.A.; Cronin, K.J. Maximizing Implant Stability in the Face of Glenoid Bone Stock Deficiency. *Orthop. Clin. North. Am.* **2024**, *55*, 101–111. [CrossRef] [PubMed]
23. Friedman, R.; Stroud, N.; Glattke, K.; Flurin, P.H.; Wright, T.; Zuckerman, J.; Roche, C. The impact of posterior wear on reverse shoulder glenoid fixation. *Bull. Hosp. Jt. Dis.* **2015**, *73*, S15–S20.
24. Ritter, D.; Denard, P.J.; Raiss, P.; Wijdicks, C.A.; Bachmaier, S. A Stemless Anatomic Shoulder Arthroplasty Design Provides Increased Cortical Medial Calcar Bone Loading in Variable Bone Densities Compared to a Short Stem Implant. *JSES Int.* **2024**, *8*, 851–858. [CrossRef]
25. Shah, A.; Werner, B.; Gobezie, R.; Denard, P.; Harmsen, S.; Brolin, T.; Bercik, M.; Thankur, S.; Doody, S.; Knopf, D.; et al. Quantifying bone loss and lateralization with standardized baseplate versus augmented baseplates. *JSES Int.* **2024**, *8*, 1055–1062. [CrossRef] [PubMed]
26. Werner, B.C.; Lin, A.; Lenters, T.R.; Lutton, D.; Creighton, R.A.; Port, J.; Doody, S.; Metcalfe, N.; Knopf, D. Influence of backside seating parameters and augmented baseplate components in virtual planning for reverse shoulder arthroplasty. *J. Shoulder Elb. Surg.* **2024**, *33*, 1352–1359. [CrossRef] [PubMed]
27. *ASTM F2028-17*; Standard Test Methods for Dynamic Evaluation of Glenoid Loosening or Disassociation. Book of ASTM Standards: West Conshohocken, PA, USA, 2017. [CrossRef]
28. Colasanti, C.A.; Lin, C.C.; Ross, K.A.; Luthringer, T.; Elwell, J.A.; Roche, C.P.; Virk, M.S.; Simovitch, R.W.; Routman, H.D.; Zuckerman, J.D. Augmented baseplates yield optimum outcomes when compared with bone graft augmentation for managing glenoid deformity during reverse total shoulder arthroplasty: A retrospective comparative study. *J. Shoulder Elb. Surg.* **2023**, *32*, 958–971. [CrossRef]
29. Boileau, P.; Morin-Salvo, N.; Gauci, M.-O.; Seeto, B.L.; Chalmers, P.N.; Holzer, N.; Walch, G. Angled BIO-RSA (bony-increased offset–reverse shoulder arthroplasty): A solution for the management of glenoid bone loss and erosion. *J. Shoulder Elb. Surg.* **2017**, *26*, 2133–2142. [CrossRef] [PubMed]
30. Simcox, T.G.; Hao, K.A.; Dada, O.; Beason, A.M.; Khlopas, A.; Farmer, K.W.; King, J.J.; Schoch, B.S.; Wright, T.W.; Struk, A.M.; et al. Survivorship and Clinical Outcomes of Reverse Total Shoulder Arthroplasty in Patients with Large Glenoid Defects Using the Stilting Technique and a Baseplate with Central Ingrowth Cage and Peripheral Locking Screws. *J. Shoulder Elb. Surg.* **2024**. *Online ahead of printing*. [CrossRef] [PubMed]
31. VandeKleut, M.L.; Yuan, X.; Teeter, M.G.; Athwal, G.S. Bony increased-offset reverse shoulder arthroplasty vs. metal augments in reverse shoulder arthroplasty: A prospective, randomized clinical trial with 2-year follow-up. *J. Shoulder Elb. Surg.* **2022**, *31*, 591–600. [CrossRef]
32. Wittmann, T.; Denard, P.J.; Werner, B.C.; Raiss, P. Glenoid lateralization in reverse shoulder arthroplasty: Metal vs. bone offset in different implant designs. *JSES Int.* **2024**, *8*, 845–850. [CrossRef] [PubMed]
33. Sandberg, O.H.; Aspenberg, P. Inter-trabecular bone formation: A specific mechanism for healing of cancellous bone. *Acta Orthop.* **2016**, *87*, 459–465. [CrossRef] [PubMed]
34. Achors, K.; Diaz, M.A.; Simon, P.; Hill, B.; Christmas, K.N.; Cronin, K.J.; Frankle, M.A. Avoiding Glenoid Baseplate Fixation Failure by Altering Surgical Technique for Varying Bone Densities. *JBJS Open Access* **2022**, *7*, e22. [CrossRef] [PubMed]
35. Eggermont, F.; Verdonschot, N.; van der Linden, Y.; Tanck, E. Calibration with or without phantom for fracture risk prediction in cancer patients with femoral bone metastases using CT-based finite element models. *PLoS ONE* **2019**, *14*, e0220564. [CrossRef] [PubMed]
36. Free, J.; Eggermont, F.; Derikx, L.; van Leeuwen, R.; van der Linden, Y.; Jansen, W.; Raaijmakers, E.; Tanck, E.; Kaatee, R. The effect of different CT scanners, scan parameters and scanning setup on Hounsfield units and calibrated bone density: A phantom study. *Biomed. Phys. Eng. Express* **2018**, *4*, 12. [CrossRef]
37. Tabarestani, T.Q.; Levin, J.M.; Warren, E.; Boadi, P.; Twomey-Kozak, J.; Wixted, C.; Goltz, D.E.; Wickman, J.; Hurley, E.T.; Anakwenze, O.; et al. Preoperative glenoid bone density is associated with systemic osteoporosis in primary shoulder arthroplasty. *Semin. Arthroplast. JSES* **2023**, *33*, 727–734. [CrossRef]
38. Levin, J.M.; Rodriguez, K.; Polascik, B.A.; Zeng, S.; Warren, E., Jr.; Rechenmacher, A.; Helmkamp, J.; Goltz, D.E.; Wickman, J.; Klifto, C.S.; et al. Simple preoperative radiographic and computed tomography measurements predict adequate bone quality for stemless total shoulder arthroplasty. *J. Shoulder Elb. Surg.* **2022**, *31*, 2481–2487. [CrossRef] [PubMed]

39. Cronin, K.J.; Vaughan, A.; Tzeuton, S.; Abboud, J.A. Prospective assessment of osteoporosis in total shoulder arthroplasty. *Semin. Arthroplast. JSES* **2023**, *33*, 15–21. [CrossRef]
40. Lee, D.C.; Hoffmann, P.F.; Kopperdahl, D.L.; Keaveny, T.M. Phantomless calibration of CT scans for measurement of BMD and bone strength-Inter-operator reanalysis precision. *Bone* **2017**, *103*, 325–333. [CrossRef] [PubMed]

8. References

1. Łukasiewicz, P., et al., *Narrative review of influence of prosthesis lateralization on clinical outcomes in reverse shoulder arthroplasty: glenoid vs. humerus vs. combined.* Annals of Joint, 2023. **8**: p. 24-24.

2. Churchill, R.S. and G.S. Athwal, *Stemless shoulder arthroplasty-current results and designs.* Curr Rev Musculoskelet Med, 2016. **9**(1): p. 10-6.

3. Kramer, M., et al., *The effects of length and width of the stem on proximal humerus stress shielding in uncemented primary reverse total shoulder arthroplasty.* Arch Orthop Trauma Surg, 2023.

4. Harmer, L., T. Throckmorton, and J.W. Sperling, *Total shoulder arthroplasty: are the humeral components getting shorter?* Curr Rev Musculoskelet Med, 2016. **9**(1): p. 17-22.

5. Kumar, S., et al., *Periprosthetic Humeral Fractures After Shoulder Arthroplasty.* 2004. **86**(4): p. 680-689.

6. Nagels, J., M. Stokdijk, and P.M. Rozing, *Stress shielding and bone resorption in shoulder arthroplasty.* Journal of Shoulder and Elbow Surgery, 2003. **12**(1): p. 35-39.

7. Raiss, P., et al., *Radiographic changes around humeral components in shoulder arthroplasty.* J Bone Joint Surg Am, 2014. **96**(7): p. e54.

8. Aibinder, W.R., et al., *Stress shielding following stemless anatomic total shoulder arthroplasty.* Shoulder Elbow, 2023. **15**(1): p. 54-60.

9. Alikhah, A., et al., *Screw fixation in stemless shoulder arthroplasty for the treatment of primary osteoarthritis leads to less osteolysis when compared to impaction fixation.* BMC Musculoskelet Disord, 2020. **21**(1): p. 295.

10. Greis, M., et al., *Proximal humeral bone loss in stemless shoulder arthroplasty: potential factors influencing bone loss and a new classification system.* Arch Orthop Trauma Surg, 2022.

11. Denard, P.J., et al., *Proximal stress shielding is decreased with a short stem compared with a traditional-length stem in total shoulder arthroplasty.* J Shoulder Elbow Surg, 2018. **27**(1): p. 53-58.

12. Schnetzke, M., et al., *Radiologic bone adaptations on a cementless short-stem shoulder prosthesis.* J Shoulder Elbow Surg, 2016. **25**(4): p. 650-7.

13. Habermeyer, P., et al., *Midterm results of stemless shoulder arthroplasty: a prospective study.* J Shoulder Elbow Surg, 2015. **24**(9): p. 1463-72.

14. Hawi, N., et al., *Nine-year outcome after anatomic stemless shoulder prosthesis: clinical and radiologic results.* J Shoulder Elbow Surg, 2017. **26**(9): p. 1609-1615.

15. Heuberer, P.R., et al., *Radiological changes do not influence clinical mid-term outcome in stemless humeral head replacements with hollow screw fixation: a prospective radiological and clinical evaluation.* BMC Musculoskelet Disord, 2018. **19**(1): p. 28.

16. Uschok, S., et al., *Is the stemless humeral head replacement clinically and radiographically a secure equivalent to standard stem humeral head replacement in the long-term follow-up? A prospective randomized trial.* J Shoulder Elbow Surg, 2017. **26**(2): p. 225-232.

17. DeVito, P., et al., *Medial calcar bone resorption after anatomic total shoulder arthroplasty: does it affect outcomes?* J Shoulder Elbow Surg, 2019. **28**(11): p. 2128-2138.

18. Favre, P., et al., *In vitro initial stability of a stemless humeral implant.* Clin Biomech (Bristol, Avon), 2016. **32**: p. 113-7.

19. Casp, A.J., et al., *Osteoporosis and Implant-Related Complications After Anatomic and Reverse Total Shoulder Arthroplasty.* 2020. **28**(3): p. 121-127.

20. Chen, R.E., et al., *Biomechanical comparison of stemless humeral components in total shoulder arthroplasty.* Seminars in Arthroplasty: JSES, 2022. **32**(1): p. 145-153.

21. Hayden, A., et al., *Bone Quality in Total Shoulder Arthroplasty: A Prospective Study Correlating CT Hounsfield Units with Thumb Test and FRAX Score.* JSES International, 2023.

22. Cronin, K.J., et al., *Prospective assessment of osteoporosis in total shoulder arthroplasty.* Seminars in Arthroplasty: JSES, 2023. **33**(1): p. 15-21.

23. Levin, J.M., et al., *Simple preoperative radiographic and computed tomography measurements predict adequate bone quality for stemless total shoulder arthroplasty.* J Shoulder Elbow Surg, 2022. **31**(12): p. 2481-2487.

24. Barcik, J. and D.R. Epari, *Can Optimizing the Mechanical Environment Deliver a Clinically Significant Reduction in Fracture Healing Time?* Biomedicines, 2021. **9**(6).

25. Bailón-Plaza, A. and C.H. Marjolein, *Beneficial effects of moderate, early loading and adverse effects of delayed or excessive loading on bone healing.* Journal of Biomechanics, 2003. **36**(8): p. 1069-1077.

26. Ulstrup, A.K., *Biomechanical concepts of fracture healing in weight-bearing long bones.* Acta Orthop Belg, 2008. **74**(3): p. 291-302.

27. Razfar, N., et al., *Comparison of proximal humeral bone stresses between stemless, short stem, and standard stem length: a finite element analysis.* J Shoulder Elbow Surg, 2016. **25**(7): p. 1076-83.

28. Maldonado, Z.M., et al., *Straining of the intact and fractured proximal humerus under physiological-like loading.* J Biomech, 2003. **36**(12): p. 1865-73.

29. Filardi, V., *Stress distribution in the humerus during elevation of the arm and external abduction.* J Orthop, 2020. **19**: p. 218-222.

30. Ritter, D., et al., *A Stemless Anatomic Shoulder Arthroplasty Design Provides Increased Cortical Medial Calcar Bone Loading in Variable Bone Densities Compared to a Short Stem Implant.* JSES International, 2024.

31. Reeves, J.M., G.S. Athwal, and J.A. Johnson, *An assessment of proximal humerus density with reference to stemless implants.* J Shoulder Elbow Surg, 2018. **27**(4): p. 641-649.

32. Bachmaier, S., et al., *Postpreparation peri-implant humeral bone density and fixation strength vary based on design in stemless reverse shoulder arthroplasty.* Seminars in Arthroplasty: JSES, 2021. **31**(4): p. 677-687.

33. Alidousti, H., et al., *Spatial mapping of humeral head bone density.* J Shoulder Elbow Surg, 2017. **26**(9): p. 1653-1661.

34. Celik, H., et al., *Three-dimensional Volumetric Filling Ratio Predicts Stress Shielding in Short-stem Anatomic Total Shoulder Arthroplasty.* J Am Acad Orthop Surg, 2020. **28**(24): p. 1047-1054.

35. Reeves, J.M., et al., *Implications of humeral short-stem diametral sizing on implant stability.* JSES Int, 2023. **7**(6): p. 2445-2453.

36. Testa, E.J., et al., *Increased Risk of Periprosthetic Fractures and Revision Arthroplasty in Patients Undergoing Shoulder Arthroplasty With a History of Prior Fragility Fractures: A Matched Cohort Analysis.* J Am Acad Orthop Surg, 2023. **31**(9): p. e473-e480.

37. Group, A.C.o.R.R., et al., *Predictors of acromial and scapular stress fracture after reverse shoulder arthroplasty: a study by the ASES Complications of RSA Multicenter Research Group.* J Shoulder Elbow Surg, 2021. **30**(10): p. 2296-2305.

38. Bernatz, J.T., et al., *Prevalence and Treatment of Osteoporosis Prior to Elective Shoulder Arthroplasty.* J Am Acad Orthop Surg Glob Res Rev, 2020. **4**(12): p. e20 00204.

39. Daher, M., et al., *Osteoporosis in the Setting of Shoulder Arthroplasty: A Narrative Review.* Geriatr Orthop Surg Rehabil, 2023. **14**: p. 21514593231182527.

40. Boileau, P., et al., *Angled BIO-RSA (bony-increased offset–reverse shoulder arthroplasty): a solution for the management of glenoid bone loss and erosion.* Journal of Shoulder and Elbow Surgery, 2017. **26**(12): p. 2133-2142.

41. Imiolczyk, J.-P., et al., *Metallic humeral and glenoid lateralized implants in reverse shoulder arthroplasty for cuff tear arthropathy and primary osteoarthritis.* JSES International, 2022. **6**(2): p. 221-228.

42. Merolla, G., et al., *BIO-RSA vs. metal-augmented baseplate in shoulder osteoarthritis with multiplanar glenoid deformity: a comparative study of radiographic findings and patient outcomes.* J Shoulder Elbow Surg, 2023. **32**(11): p. 2264-2275.

43. Pervaiz, K., et al., *Osteoporosis and shoulder osteoarthritis: incidence, risk factors, and surgical implications.* J Shoulder Elbow Surg, 2013. **22**(3): p. e1-8.

44. Spross, C., et al., *Deltoid Tuberosity Index: A Simple Radiographic Tool to Assess Local Bone Quality in Proximal Humerus Fractures.* Clin Orthop Relat Res, 2015. **473**(9): p. 3038-45.

45. Churchill, R.S., et al., *Clinical and Radiographic Outcomes of the Simpliciti Canal-Sparing Shoulder Arthroplasty System: A Prospective Two-Year Multicenter Study.* J Bone Joint Surg Am, 2016. **98**(7): p. 552-60.

46. Reeves, J.M., et al., *Initial Assessments of a Handheld Indentation Probe's Correlation With Cancellous Bone Density, Stiffness, and Strength: An Objective Alternative to "Thumb Testing".* Journal of Medical Devices, 2021. **15**(4).

47. Gregory, J.M., J. Siahaan, and M. Urvoy, *Preoperative metaphyseal cancellous bone density is associated with intraoperative conversion to stemmed total shoulder arthroplasty.* JSES Rev Rep Tech, 2023. **3**(3): p. 285-288.

48. Raiss, P., et al., *Validation of the distal filling ratio in uncemented convertible short-stem shoulder arthroplasty.* Arch Orthop Trauma Surg, 2023. **143**(4): p. 1833-1839.

49. Pauwels, R., et al., *CBCT-based bone quality assessment: are Hounsfield units applicable?* Dentomaxillofac Radiol, 2015. **44**(1): p. 20140238.

50. Free, J., et al., *The effect of different CT scanners, scan parameters and scanning setup on Hounsfield units and calibrated bone density: a phantom study.* Biomedical Physics & Engineering Express, 2018. **4**(5): p. 12.

51. Eggermont, F., et al., *Calibration with or without phantom for fracture risk prediction in cancer patients with femoral bone metastases using CT-based finite element models.* PLoS One, 2019. **14**(7): p. e0220564.

52. Smith, A.C.J., et al., *Internal calibration for opportunistic computed tomography muscle density analysis.* PLoS One, 2022. **17**(10): p. e0273203.

53. Winsor, C., et al., *Evaluation of patient tissue selection methods for deriving equivalent density calibration for femoral bone quantitative CT analyses.* Bone, 2021. **143**: p. 115759.

54. Reeves, J.M., et al., *Regional apparent density correlations within the proximal humerus.* JSES Int, 2021. **5**(3): p. 525-531.

55. Innocenti, B., Y. Radyul, and E. Bori, *The Use of Artificial Intelligence in Orthopedics: Applications and Limitations of Machine Learning in Diagnosis and Prediction.* Applied Sciences, 2022. **12**(21).

56. Gupta, P., et al., *Artificial Intelligence-Based Applications in Shoulder Surgery Leaves Much To Be Desired: A Systematic Review.* JSES Reviews, Reports, and Techniques, 2023.

57. Blakeney, W.G., et al., *Development and assessment of 3-dimensional computed tomography measures of proximal humeral bone density: a comparison to established 2-dimensional measures and intraoperative findings in patients undergoing shoulder arthroplasty.* JSES Int, 2021. **5**(6): p. 1008-1013.

58. Reeves, J.M., J.A. Johnson, and G.S. Athwal, *An analysis of proximal humerus morphology with special interest in stemless shoulder arthroplasty.* J Shoulder Elbow Surg, 2018. **27**(4): p. 650-658.

59. Sebro, R. and C. De la Garza-Ramos, *Machine Learning for Opportunistic Screening for Osteoporosis from CT Scans of the Wrist and Forearm.* Diagnostics (Basel), 2022. **12**(3).

Attachment A: Publication IV

Citation: Ritter D, Denard PJ, Raiss P, Wijdicks CA, Bachmaier S. Preoperative 3-dimensional computed tomography bone density measures provide objective bone quality classifications for stemless anatomic total shoulder arthroplasty. J Shoulder Elbow Surg. 2024; 33(7):1503-1511. doi: 10.1016/j.jse.2023.11.005.

J Shoulder Elbow Surg (2024) 33, 1503–1511

ELSEVIER

Journal of Shoulder and Elbow Surgery

www.elsevier.com/locate/ymse

Preoperative 3-dimensional computed tomography bone density measures provide objective bone quality classifications for stemless anatomic total shoulder arthroplasty

Daniel Ritter, MSc[a,b,*], Patrick J. Denard, MD[c], Patric Raiss, MD[d], Coen A. Wijdicks, PhD, MBA[a], Samuel Bachmaier, MSc[a]

[a]*Department of Orthopedic Research, Arthrex GmbH, Munich, Germany*
[b]*Department of Orthopaedics and Trauma Surgery, Musculoskeletal University Center Munich (MUM), University Hospital, LMU Munich, Munich, Germany*
[c]*Southern Oregon Orthopedics, Medford, OR, USA*
[d]*OCM Clinic, Munich, Germany*

Background: Reproducible methods for determining adequate bone densities for stemless anatomic total shoulder arthroplasty (aTSA) are currently lacking. The purpose of this study was to evaluate the utility of preoperative computed tomography (CT) imaging for assessing the bone density of the proximal humerus for supportive differentiation in the decision making for stemless humeral component implantation. It was hypothesized that preoperative 3-dimensional (3-D) CT bone density measures provide objective classifications of the bone quality for stemless aTSA.

Methods: A 3-part study was performed that included the analysis of cadaveric humerus CT scans followed by retrospective application to a clinical cohort and classification with a machine learning model. Thirty cadaveric humeri were evaluated with clinical CT and micro-CT (μCT) imaging. Phantom-calibrated CT data were used to extract 3-D regions of interest and defined radiographic scores. The final image processing script was applied retrospectively to a clinical cohort (n = 150) that had a preoperative CT and intraoperative bone density assessment using the "thumb test," followed by placement of an anatomic stemmed or stemless humeral component. Post-scan patient-specific calibration was used to improve the functionality and accuracy of the density analysis. A machine learning model (Support vector machine [SVM]) was utilized to improve the classification of bone densities for a stemless humeral component.

Results: The image processing of clinical CT images demonstrated good to excellent accuracy for cylindrical cancellous bone densities (metaphysis [ICC = 0.986] and epiphysis [ICC = 0.883]). Patient-specific internal calibration significantly reduced biases and unwanted variance compared with standard HU CT scans ($P < .0001$). The SVM showed optimized prediction accuracy compared with conventional statistics with an accuracy of 73.9% and an AUC of 0.83 based on the intraoperative decision of the surgeon. The SVM model based on density clusters increased the accuracy of the bone quality classification to 87.3% with an AUC of 0.93.

Conclusions: Preoperative CT imaging allows accurate evaluation of the bone densities in the proximal humerus. Three-dimensional regions of interest, rescaling using patient-specific calibration, and a machine learning model resulted in good to excellent prediction for objective bone quality classification. This approach may provide an objective tool extending preoperative selection criteria for stemless humeral component implantation.

Investigation performed at the Arthrex Department of Orthopedic Research, Munich, Germany.

*Reprint requests: Daniel Ritter, MSc, Department of Orthopedic Research, Arthrex GmbH, Erwin-Hielscher-Strasse 9, Munich, 81249, Germany.
E-mail address: publications@arthrex.com (D. Ritter).

https://doi.org/10.1016/j.jse.2023.11.005

Level of evidence: Anatomy Study; Imaging

Keywords: Stemless aTSA; bone density; patient-specific calibration; machine learning; CT imaging; 3D CT reconstruction

In recent years, anatomic total shoulder arthroplasty (aTSA) has seen a trend toward stemless humeral fixation. Standard-length humeral stems can be associated with intraoperative periprosthetic fracture, proximal humeral bone loss due to stress shielding, and significant bone loss in revision surgery.[15,18,22,25,37] Stemless components may avoid many of these problems, but fixation of stemless components may be more dependent on bone quality. Poor bone quality is associated with unstable humeral implant fixation and a higher risk for complications in TSA.[4,5,10] To identify adequate bone quality for stemless implant fixation, the "thumb test" is often used, which is limited by its intraoperative application (as opposed to preoperative) and the fact that it is highly subjective.[6,29]

Preoperative planning with computed tomography (CT) imaging has become a common tool to assess glenoid morphology. CT data may also offer the ability to provide objective measurements of bone mineral density (BMD).[7,16,19,33] Gray-scale values for density interpolation on the Hounsfield unit (HU) scale from CT scans have demonstrated variability because of the use of different devices, exposure parameters, the position of the measurement, and the mass inside and outside the field of view.[11,23] However, patient-specific calibration of the gray-scale values on BMD has been reported to reduce inaccuracies.[9,32,36]

Manual calculation from CT scans, such as the deltoid tuberosity index and circular metaphyseal 2-dimensionally measured HU densities, have been found to be valuable for predicting the ability to place a stemless device with central impacted fixation.[7,12,16,19,33] However, these tools may not apply to other stemless fixation designs,[2,24,27,28] as density interpolation and 3-D regional bone patterns were not included. The latter approaches could include a threshold analysis and predictive modeling with machine learning to provide a better use of preoperative CT data to contribute to implant decision making or preoperative notification for potential patients at risk due to osteoporosis complications.

The purpose of this study was to evaluate the utility of preoperative CT imaging assessing the bone density of the proximal humerus for supportive differentiation in the decision making for stemless humeral component implantation. It was hypothesized that preoperative 3-D CT bone density measures provide objective classification of the patients' humeral bone quality.

Materials and methods

This is a retrospective diagnostic study comprising 3 parts: (1) a phantom-calibrated cadaveric CT investigation including feature extraction of various bone density parameters, (2) the retrospective evaluation using the bone model in a clinical cohort, and (3) the establishment of prediction models to compare bone density classifications (Fig. 1).

Feature extraction

Thirty fresh frozen cadaveric arm specimens (71.9 ± 11.9 years; BMI: 22.7 ± 4.2; 13 females and 17 males) were procured (Science Care Inc., Phoenix, AZ, USA) and prepared for density analyses with the arms stored at –20°C. The cadaveric humeri were scanned with a voxel size of 0.6 mm (120 kVp and 80 mA) in a clinical CT scanner (SOMATOM Definition AS+; Siemens Healthcare GmbH) with gray-scale values converted into BMD (mgHA/cm^3) values using the manufacturer's density phantoms. Additional micro-CT (μCT; Phoenix V|tome|x S micro-CT scanner; Waygate Technologies, Huerth, Germany) scans with a voxel resolution of 50 μm and a phantom-calibrated gray scale in BMD (mgHA/cm^3) were used as a reference to assess the accuracy of the density analyses. A custom image-processing script (MATLAB, version 2023a; MathWorks, Natick, MA, USA) with segmentation and morphologic image-processing steps was created to investigate the various CT scans of the cadaveric humeri (CT and μCT) and retrospective clinical CT scans. Bone model development was performed based on CT voxel data imported as a 4-dimensional point cloud (ie, [x, y, z, mgHA/cm^3]). Global volumes of interest (VOIs) included bone portions (epiphysis, metaphysis, and diaphysis) separated in reference to anatomic landmarks and along the diaphyseal or metaphyseal axes of the humeral bone (Fig. 2). Although the main orientation of the greater tubercle cylinder was aligned with the diaphyseal axis, the main orientation of the VOIs in the proximal humerus was aligned with the metaphyseal axis. The epi- and metaphyseal bone cylinder diameter was defined as 50% of the largest diameter at the resection plane. The cylinder depth was defined as 50% of the respective global volume. The cortical shoulder scores (fitted Tingart,[3] Gianotti, and deltoid tuberosity index [DTI]) were calculated using distance measuring and pixel counting methods. The morphologic parameter (ie, bone volume [BV] / total volume [TV]) calculation of each VOI was also based on pixel counting methods using the respective BV of the TV.

Retrospective evaluation

A retrospective review was performed on a multicenter database (Virtual Implant Positioning [VIP] System; Arthrex Inc., Naples, FL, USA) of shoulder arthroplasties (n = 150; 69 ± 10 years; 70 female and 80 male patients) performed between December 2019 and December 2022. Inclusion criteria included primary aTSA, diagnoses of primary osteoarthritis, a preoperative CT scan, and humeral fixation with either a press-fit stemmed (ie, standard stem) (Univers II Total Shoulder System; Arthrex Inc.), a short-stem

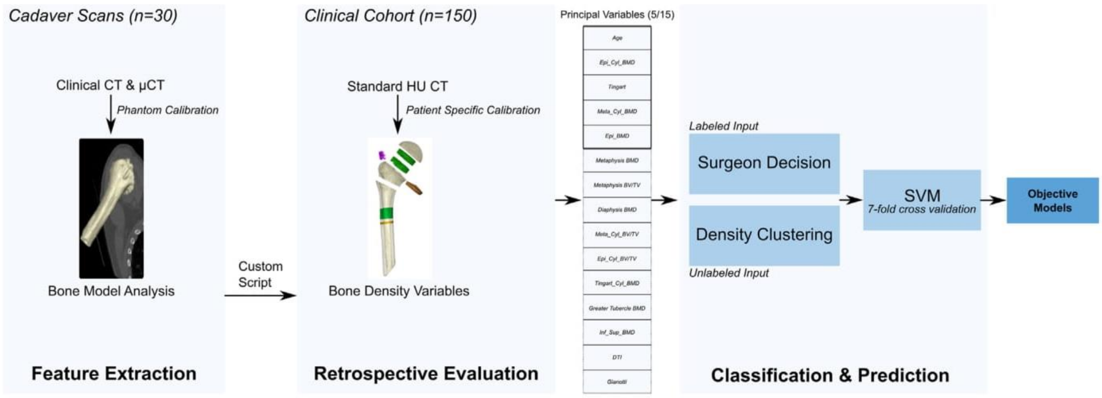

Figure 1 Schematic illustration of specimen allocation of the different examinations and structure of the analysis steps in terms of feature extraction in cadaveric scans, retrospective evaluation in a clinical cohort, and classification and prediction. *CT*, computed tomography; *µCT*, micro–computed tomography; *HU*, Hounsfield unit; *BMD*, bone mineral density; *BV*, bone volume; *TV*, total volume; *DTI*, deltoid tuberosity index; *SVM*, support vector machine.

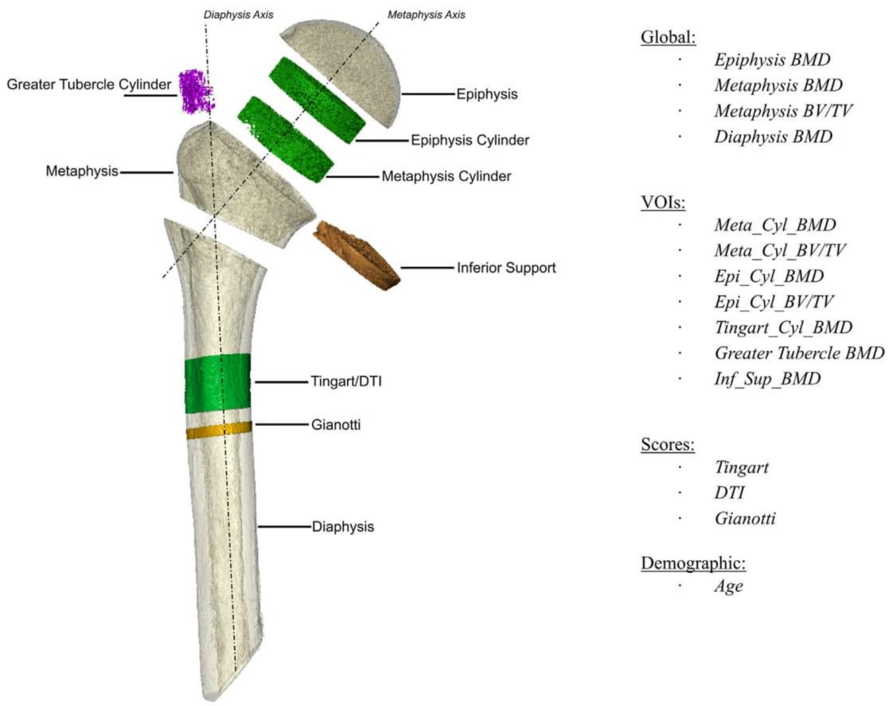

Figure 2 Examples of 3-dimensionally rendered µCT images along with the analysis axes used for assessment of the respective VOI, with all outcome parameters listed with the corresponding density measure on the right side. *DTI*, deltoid tuberosity index; *BMD*, bone mineral density; *BV*, bone volume; *TV*, total volume; *VOIs*, volumes of interest.

(Univers Apex Total Shoulder System; Arthrex Inc.), or a stemless (Eclipse Stemless Shoulder Prosthesis; Arthrex Inc.) implant.

A total of 150 preoperative CT scans were identified of cases treated with 73 stemmed and 77 stemless components from 91 different sites. The anonymized preoperative CT scans were evaluated using the custom image-processing script that previously was verified with the µCT data. Based on the outcome variables, predictive models were developed using defined

Table I Summary of the predictive models including the method used, input data, and the targeted prediction

Model	*Model Surg HU*	*Model Surg HA*	*SVM Surg HA*	*SVM Cluster HA*
Method	QDA	QDA	SVM	*K*-means + SVM
Input data	HU scaled	Rescaled BMD	Rescaled BMD	Rescaled BMD
	Labeled	Labeled	Labeled	Unlabeled
Prediction	Surgeon decision	Surgeon decision	Surgeon decision	Low- or high BMD cluster

HU, Hounsfield units; *QDA*, quadratic discriminant analysis; *BMD*, bone mineral density; *SVM*, support vector machine.

Table II ICCs to assess the accuracy of clinical CT scans by the use of μCT data using phantom-calibrated scans

	Clinical CT vs. μCT		
	ICC (95% CI)		*P* value
Global			
Epiphysis BMD	0.642	0.462-0.999	<.001
Metaphysis BMD	0.246	0.068-0.997	.001
Metaphysis BV/TV	0.507	0.279-0.999	<.001
Diaphysis BMD	0.173	0.027-0.996	.008
VOI			
Meta_Cyl_BMD	0.986	0.926-0.999	<.001
Meta_Cyl_BV/TV	0.460	0.310-0.987	.113
Epi_Cyl_BMD	0.883	0.570-0.999	<.001
Epi_Cyl_BV/TV	0.295	0.098-0.998	<.001
Tingart_Cyl_BMD	0.186	0.034-0.996	.060
Greater tubercle BMD	0.380	0.160-0.998	<.001
Inf_Sup_BMD	0.900	0.616-0.999	<.001
Scores			
Tingart	0.575	0.028-0.996	.007
DTI	0.387	0.166-0.998	<.001
Gianotti	0.291	0.096-0.998	<.001

BMD, bone mineral density; *BV*, bone volume; *TV*, total volume; *VOI*, volume of interest; *DTI*, deltoid tuberosity index; *CT*, computed tomography; *μCT*, micro–computed tomography; *ICC*, intraclass correlation coefficient; *CI*, confidence interval.

principal variables for objective bone quality classifications. To set a baseline for differing scales of the retrospectively gathered CT scans resulting from intra- and interscanner variations, patient-specific air-muscle-fat calibration was performed to interpolate the gray scales on BMD values recently reported with good functionality.[9,32,36] Therefore, air, muscle, and fat gray values were used to linearly interpolate the CT data on a density scale (–840, 30, –80 mgHA/cm^3) to allow for improved application of the image-processing steps on more consistent data. Scanning parameters were defined according to specifications needed for the use of a planning software (Virtual Implant Positioning [VIP] System; Arthrex Inc.) with resolutions below 0.6 mm (range 0.35-0.6 mm).

Outcome parameters for comparison included demographic and bone density data from the available CT scans. According to the Scree plot, 5 parameters were found to be sufficient to define the statistical models describing 99% of the data variance. Variable selection was performed according to the *F* value and respective probability to stepwise select the 5 principal variables. Principal variables served as input variables for classifications and predictions (*Age*, *Epi_Cyl_BMD*, *Tingart*, *Meta_Cyl_BMD*, and *Epi_BMD*).

Classification and prediction

Predictive models were created either to predict the surgeons' treatment decision (labeled input) or for the assignment to density clusters (unlabeled input) (Table I). Multivariate models (Model Surg HA and Model Surg HU) were used to analyze the separability between labeled patients (short and standard stem combined vs. stemless) using a quadratic discriminant analysis. The maximum likelihood estimation including the bootstrapping method was used to analyze these statistical models regarding accuracy, sensitivity, and specificity.

Machine learning models for group classification were created using a support vector machine (SVM), which is a supervised machine learning model that is commonly used for pattern recognition, classification, and regression analysis. Gaussian kernel functions were tuned, and *k*-fold cross-validation (Sturge rule: $k = 7$) was used. The kernel scale was restricted to a "medium" fine range to prevent overfitting. The SVM was trained to classify the data based on either the surgeons' treatment decisions (SVM Surg HA) or the density clustered labels (SVM Cluster HA). These clusters were created using the *K*-means principle (2 clusters plus 1 outlier cluster resulted from cohesion optimization according to the Akaike and Bayesian information criteria). The following application of an SVM was used to achieve optimization of the cluster separation, including 7-fold cross-validation.

Outcomes from statistical modeling and machine learning were reported according to current recommendations and checklists (ie, TRIPOD).[13,14,20] Receiver operating characteristic curves were used to analyze the different models. Reliable prediction of bone densities for stemless arthroplasty was intended using 3D preoperative CT measures. The performances of the models were rated according to the area under the curve (AUC) as excellent (0.9-1.0), good (0.8-0.9), fair (0.7-0.8), and poor (0.6-0.7).

Statistical analysis

The accuracy of the extracted features of the cadaveric clinical CT scans was examined with μCT data using intraclass correlation coefficients (ICCs). A 2-way random effects analysis for single measures is taken in the experiment and reliability is applied to a context of the consistency of a single measure of a single rater. ICCs greater than 0.75 were considered excellent, ICCs of 0.40-0.75 were considered to indicate moderate reliability, and those less than 0.40, poor reliability.[17,21]

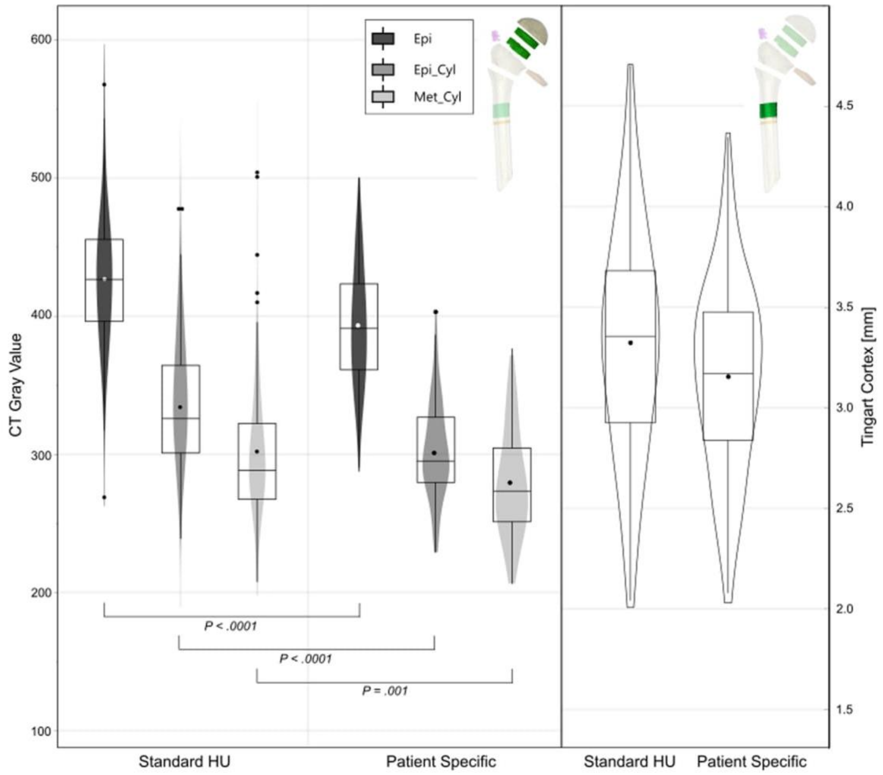

Figure 3 Box plots with mean and median values and distribution fitting of the principal density variables for the differently calibrated gray scales of the retrospectively evaluated cohort. *CT*, computed tomography; *HU*, Hounsfield unit.

Statistical analysis of the retrospectively evaluated cohort included a 1-way analysis of variance with post hoc pairwise analysis using the Holm-Sidak correction. Significance was defined as $P \leq .05$, and the desired power level was set at 0.8. The Shapiro-Wilks test and Brown-Forsythe test were used to confirm each data set followed a normal distribution and equal variance, respectively. A nonparametric test (Kruskal-Wallis) was used for data sets that failed these tests. For Kruskal-Wallis tests that found significance, a post hoc test according to the Dunn method was conducted to further analyze the differences. Additional differences in variances were analyzed using the Brown-Forsythe test.

All statistical analyses were performed using commercial software (JMP, version 17.0.0 [JMP Statistical Discovery, Cary, NC, USA], and MATLAB, version 2023a [MathWorks]).

Results

Feature extraction

ICCs for the extracted features on phantom-calibrated cadaver CT scans compared with μCT images (Table II) demonstrated good to excellent accuracy for specific BMD VOIs (*Meta_Cyl_BMD* [ICC = 0.986], *Epi_Cyl_BMD* [ICC = 0.883], and *Inf_Sup_BMD* [ICC = 0.900]). Inaccuracies with poor correlation coefficients were found for clinical BV/TV observations (*Meta_Cyl_BV/TV* [ICC = 0.046] and *Epi_Cyl_BV/TV* [ICC = 0.295]). The Tingart cylindric fitted cortical thickness showed moderate but highest coefficients of the scores (ICC = 0.575).

Retrospective evaluation

Patient-specific internal calibration significantly reduced the biases for global epiphyseal and cylindric cancellous BMD parameters compared to HU densities of the selected principal variables (Fig. 3). The patient-specific calibration significantly reduced variability and outliers for *Epi_Cyl_BMD* ($P < .0001$, $F = 34.7$) and *Meta_Cyl_BMD* ($P < .0001$, $F = 13.6$). No statistical differences between the calibration procedures were found ($P = .910$) without the variance differing ($P = .920$, $F = 0.120$) for the fitted Tingart score.

Table III Mean values and statistical analysis of the density variables treated with stemless or stemmed implants based on (A) surgeons' decisions compared to (B) objective bone density clustering

	A. Surgeon classification			B. Density clustering		
	Stemless (n = 77)	Stem (n = 73)	*P* value	Stemless (n = 82)	Stem (n = 68)	*P* value
Global BMD						
Epiphysis BMD	400 ± 44	386 ± 44	.078	424 ± 38	368 ± 32	**<.001**
Metaphysis BMD	384 ± 44	372 ± 41	.113	409 ± 35	353 ± 31	**<.001**
Metaphysis BV/TV	0.36 ± 0.12	0.34 ± 0.14	.477	0.37 ± 0.14	0.32 ± 0.11	**.025**
Diaphysis BMD	726 ± 75	722 ± 90	.375	743 ± 72	709 ± 88	**.017**
VOIs						
Meta_Cyl_BMD	287 ± 47	273 ± 32	**.038**	304 ± 38	262 ± 34	**<.001**
Meta_Cyl_BV/TV	0.24 ± 0.11	0.22 ± 0.11	.350	0.25 ± 0.13	0.21 ± 0.10	**.030**
Epi_Cyl_BMD	309 ± 34	296 ± 36	**.040**	329 ± 30	281 ± 23	**<.001**
Epi_Cyl_BV/TV	0.38 ± 0.14	0.36 ± 0.14	.486	0.40 ± 0.15	0.34 ± 0.12	**.018**
Tingart_Cyl_BMD	690 ± 81	686 ± 72	.780	705 ± 82	674 ± 70	**.021**
Inf_Sup_BMD	307 ± 51	295 ± 45	.148	316 ± 50	288 ± 41	**.001**
Scores						
Tingart	3.1 ± 0.5	3.2 ± 0.4	.275	3.4 ± 0.4	3.0 ± 0.4	**<.001**
Age	67 ± 10	70 ± 8	**.023**	66 ± 10	71 ± 8	**.001**

BMD, bone mineral density; *BV*, bone volume; *TV*, total volume; *VOIs*, volumes of interest.
Gianotti score, deltoid tuberosity index, and greater tubercle BMD were removed because of low contribution to statistical modeling.
Boldface indicates statistical significance ($P < .05$).

Classification and prediction

A comparison of the variables based on the surgeons' decision showed significant differences for the cylindric cancellous BMD values and age (Table III, *A*). Density clustering improved the discriminant power with significant differences in all accurately evaluable outcome parameters (Table III, *B*).

Multivariate modeling using patient-specific calibrated (*Model Surg HA*) data improved the separation accuracy to 70.9% with an AUC of 0.76 compared with standard HU data (*Model Surg HU*) (Fig. 4). The surgeon decision–based SVM (*SVM Surg HA*) increased the accuracy to 73.9% with an AUC of 0.83. Classification according to the patients' bone densities by an SVM model (*SVM Cluster HA*) improved the accuracy to 87.3% with an AUC of 0.93 (Fig. 4).

Discussion

The most important finding of this study was that preoperative CT imaging can provide objective bone quality classifications using the proximal humerus bone densities to better differentiate during the decision-making process for stemless humeral component implantation. Patient-specific calibrated 3-D bone volumes significantly reduced biases and unwanted variance, providing a consistent input for objective bone density classifications. A machine learning algorithm in combination with demographic and density parameters showed good to excellent performance (AUC = 0.93) using a preoperative bone quality evaluation based on standard CT imaging and respective processing tools. Although multiple imaging studies in clinical[3,7,12,16,19,33] and nonclinical settings[2,24,27,28] are available, the primary goal of the current study was to improve the use of quantified bone densities to alert the surgeon for potential complications in stemless aTSA.[4] Our study combined the strength of various recent approaches by using systemic standardized density analyses,[2,3,24,27,28] assessments and correlations with the current intraoperative practice,[7,16,19,33] and prediction using machine learning tools.[31]

In a prospective study of patients undergoing TSA, Cronin et al[7] showed that low BMD affected intraoperative decision making in 16% of the cases. Healthy bone was intraoperatively identified in 95.5% of these cases but surgeons struggled with identifying poor bone (47.7% accuracy). Thus, there is a need for objective density measures. The intraoperative thumb test is currently used as criteria for the bone quality–based decision to place a stemless humeral component. Greater variations in the humeral head cut level or the location where the thumb test is performed by subjectively gauging the bone resistance to deformation and tactile assessment of bone quality depend on surgical experience.[16] Spatial mapping of the proximal humeral bone showed increasing bone density from central to peripheral regions below the anatomic neck, indicating a higher primary fixation strength with strategically located

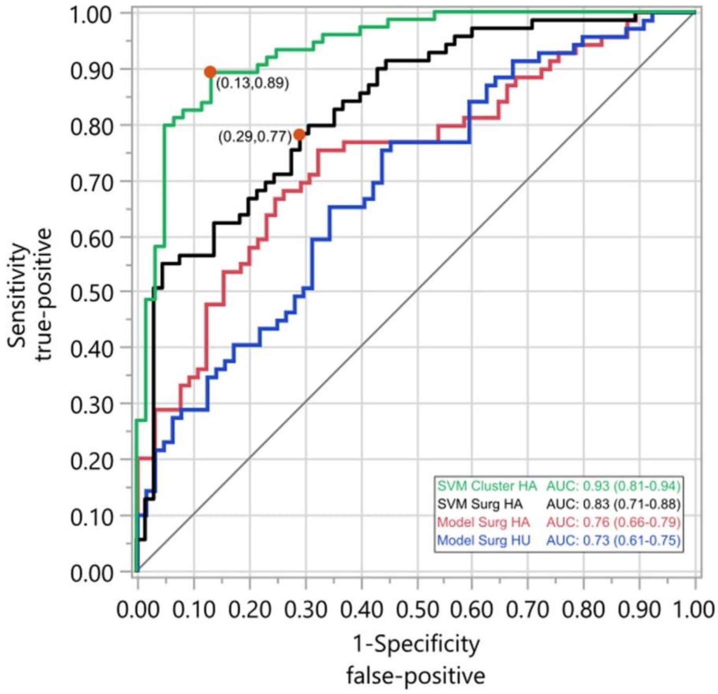

Figure 4 Receiver operating characteristic curves demonstrating the optimal threshold to maximize sensitivity and specificity for the final cluster-based SVM model compared with the model based on surgeons' classifications. The areas under the curves (*AUCs*) with 95% confidence intervals describe the performance of the models based on either patient-specific calibration (HA) or standard HU scale (HU). *SVM*, support vector machine; *HU*, Hounsfield unit.

implant fixation features.[1,2,26] Although the initial fixation strength varies between available humeral component designs, stemless humeral implants should be used in general with caution in weaker bone. However, the ability to implant a stemless device may vary depending on the design type and the respective peri-implant bone density where the fixations take place.[2] Current evidence suggests that cortical rim–supported, screwed stemless TSA devices are usable in a wider range of bone densities than central impaction designs.[5] However, variable bone density may affect clinical outcomes and bone resorption processes in the longer term.[4] An objective preoperative bone quality assessment aside from demographic factors may pay off to support the surgeons' decision process, especially with regard to future applications of stemless implants in reverse shoulder arthroplasty. It is notable that reverse shoulder arthroplasty populations have a significantly increased prevalence of osteoporosis and higher rates of periprosthetic fracture and revision surgery.[4] As CT-based preoperative planning for glenoid implant placement has become commonplace, this also provides an opportunity to objectively assess humeral bone quality without additional CT scanning.[30]

Based on the stated relevant regions for implant fixation, the use of defined 3-D VOIs, superior and inferior to the anatomic neck, improved the accuracy of the density evaluation compared with, for example, 2-D measures or global volumes. Linear interpolation on a BMD scale ($mgHA/cm^3$) using patient-specific calibration based on air, muscle, and fat gray values additionally reduced inter- and intrascanner variations for consistent segmentation to approximate accuracy of the phantom-calibrated densities based on which the image-processing algorithm was developed. These optimizations resulted in improved predictions (AUC = 0.93) compared with those in a recent study that used standard 2-D HU measurements (AUC = 0.776).[16] Levin et al[19] also showed excellent predictions (AUC = 0.98) based on their data set. However, their predictions were based on an unequally distributed population (stemmed n = 56 and stemless n = 5), with only 5 stemless TSA cases based on subjective surgeon decisions, and thus should be used cautiously. Furthermore, an external[14] or internal validation procedure of model performances in shoulder arthroplasty studies is often lacking.[7,12,16,19] Commonly a *k*-fold cross- or held-out validation is suggested for multivariable statistical and machine learning models.[20] In our study, a *k*-fold cross-validation was used to prevent the model from overfitting, and the use of scans from 91 sites implies external validity of the approach on these data. However, external validation from an independent user is missing and requires further prospective evaluation.

The potential extension from subjective surgeon decision–based data labeling to a semiautomated clustering of the bone density data in this study demonstrated the benefits of setting a stronger focus on CT density data. Density clustering and SVM classification may overfit the respective model but objectify the decision making apart from the surgeon's thumb. Similar to recent studies, an essential step was the use of patient-specific internal calibration that was shown to correct inaccuracies[9,32,36] resulting from different CT devices, exposure parameters, the position of the measurement, and the mass inside and outside the field of view.[23] Application of this postscan internal patient-specific calibration resulted in significantly reduced unwanted variances and biases. Although strong correlations between 2-D cortical scores and metaphyseal observations have been reported in the past,[8,19,33,34] poorer performance in terms of repeatability has also been shown recently, suggesting caution when using these measures in 2 dimensions.[16] Three-dimensional pixel counting and fitting to a hollow cylinder of the Tingart area improved reliability and was a valuable contribution to statistical modeling.[3,35]

In accordance with current literature, our results demonstrated that opportunistic screening of bone quality in the proximal humerus can be performed based on routine CT scans obtained for shoulder arthroplasty. Implementation in a preoperative planning tool including a machine learning model and application of a patient-specific calibration based on CT attenuations could significantly improve overall objective selectivity compared to intraoperative or 2-D HU measures.

Limitations

We acknowledge some limitations to the current study. Patient-specific calibration was only compared to a standard HU scale but not to more accurate phantom-calibrated scans. Recalibration with density phantoms in a clinical setting may be more accurate and represents a topic for future studies to allow for validation of postscan calibration with ground true BMD values. Nevertheless, image processing and prediction models were intended to work in an arthritic clinical population with standard CT scans (without phantom), which is ensured in the current approach. The sample size of this study as the basis for the machine learning models was small. Therefore, *k*-fold cross-validation was used as commonly suggested for smaller data sets. The semiautomated labeling based on bone densities followed by a classification learner may overfit the model but shows the benefit of machine learning approaches, objectively applied apart from the surgeon's thumb decision. Therefore, prospective validation studies should seek to validate the created classification models and already existing thresholds, to further elucidate optimal prediction of adequate bone quality to achieve successful fixation with stemless TSA. Future work should also investigate critical bone qualities regarding variable available humeral implant designs with differing anchoring principles within a wider range of patient bone quality. Additionally, the application of this approach for reverse shoulder arthroplasty implantations remains a research question for the future.

Conclusion

Preoperative CT imaging allows accurate evaluation of the bone densities in the proximal humerus. Three-dimensional regions of interest, rescaling using patient-specific calibration, and a machine learning model resulted in good to excellent prediction for objective bone quality classification. This approach may provide an objective tool extending preoperative selection criteria for stemless humeral component implantation.

Disclaimers:

Funding: Arthrex provided full support to this study
Conflicts of interest: Daniel Ritter is an employee of Arthrex. Patrick J. Denard receives consulting fees and honoraria, support for travel to meetings for the study or other purposes, and royalties from Arthrex. Patric Raiss receives consulting fees and honoraria and support for travel to meetings for the study or other purposes from Arthrex. Coen A. Wijdicks is an employee of Arthrex. Samuel Bachmaier is an employee of Arthrex.

References

1. Alidousti H, Giles JW, Emery RJH, Jeffers J. Spatial mapping of humeral head bone density. J Shoulder Elbow Surg 2017;26:1653-61. https://doi.org/10.1016/j.jse.2017.03.006
2. Bachmaier S, Flury M, Lichtenberg S, Schwyzer H-K, Anderl W, Denard PJ, et al. Postpreparation peri-implant humeral bone density and fixation strength vary based on design in stemless reverse shoulder arthroplasty. Semin Arthroplasty: JSES 2021;31:677-87. https://doi.org/10.1053/j.sart.2021.04.005
3. Blakeney WG, Urvoy M, Chaoui J, Raiss P, Athwal GS, Walch G. Development and assessment of 3-dimensional computed tomography measures of proximal humeral bone density: a comparison to established 2-dimensional measures and intraoperative findings in patients undergoing shoulder arthroplasty. JSES Int 2021;5:1008-13. https://doi.org/10.1016/j.jseint.2021.07.015
4. Casp AJ, Montgomery SRJ, Cancienne JM, Brockmeier SF, Werner BC. Osteoporosis and implant-related complications after

anatomic and reverse. J Am Acad Orthop Surg 2020;28:121-7. https://doi.org/10.5435/jaaos-d-18-00537
5. Chen RE, Knapp E, Qiu B, Miniaci A, Awad HA, Voloshin I. Biomechanical comparison of stemless humeral components in total shoulder arthroplasty. Semin Arthroplasty: JSES 2022;32:145-53. https://doi.org/10.1053/j.sart.2021.08.003
6. Churchill RS, Chuinard C, Wiater JM, Friedman R, Freehill M, Jacobson S, et al. Clinical and radiographic outcomes of the simpliciti canal-sparing shoulder arthroplasty System: a prospective two-year multicenter study. J Bone Joint Surg Am 2016;98:552-60. https://doi.org/10.2106/JBJS.15.00181
7. Cronin KJ, Vaughan A, Tzeuton S, Abboud JA. Prospective assessment of osteoporosis in total shoulder arthroplasty. Semin Arthroplasty: JSES 2023;33:15-21. https://doi.org/10.1053/j.sart.2022.07.015
8. Earp BE, Kallini JR, Collins JE, Benavent KA, Tintle SM, Rozental TD. Correlation of Hounsfield unit measurements on computed tomography of the shoulder with dual-energy X-ray absorptiometry scans and fracture risk assessment tool scores: a potential for opportunistic screening. J Orthop Trauma 2021;35:384-90. https://doi.org/10.1097/BOT.0000000000001994
9. Eggermont F, Verdonschot N, van der Linden Y, Tanck E. Calibration with or without phantom for fracture risk prediction in cancer patients with femoral bone metastases using CT-based finite element models. PLoS One 2019;14:e0220564. https://doi.org/10.1371/journal.pone.0220564
10. Favre P, Seebeck J, Thistlethwaite PA, Obrist M, Steffens JG, Hopkins AR, et al. In vitro initial stability of a stemless humeral implant. Clin Biomech 2016;32:113-7. https://doi.org/10.1016/j.clinbiomech.2015.12.004
11. Free J, Eggermont F, Derikx L, van Leeuwen R, van der Linden Y, Jansen W, et al. The effect of different CT scanners, scan parameters and scanning setup on Hounsfield units and calibrated bone density: a phantom study. Biomedical Physics & Engineering Express 2018;4:055013. https://doi.org/10.1088/2057-1976/aad66a.
12. Gregory JM, Siahaan J, Urvoy M. Preoperative metaphyseal cancellous bone density is associated with intraoperative conversion to stemmed total shoulder arthroplasty. JSES Rev Rep Tech 2023;3:285-8. https://doi.org/10.1016/j.xrrt.2023.01.009
13. Groot OQ, Ogink PT, Lans A, Twining PK, Kapoor ND, DiGiovanni W, et al. Machine learning prediction models in orthopedic surgery: a systematic review in transparent reporting. J Orthop Res 2022;40:475-83. https://doi.org/10.1002/jor.25036
14. Gupta P, Haeberle HS, Zimmer ZR, Levine WN, Williams RJ, Ramkumar PN. Artificial intelligence-based applications in shoulder surgery leaves much to Be desired: a systematic review. JSES Rev Rep Tech 2023;3:189-200. https://doi.org/10.1016/j.xrrt.2022.12.006
15. Harmer L, Throckmorton T, Sperling JW. Total shoulder arthroplasty: are the humeral components getting shorter? Curr Rev Musculoskelet Med 2016;9:17-22. https://doi.org/10.1007/s12178-016-9313-3
16. Hayden A, Cotter EJ, Hennick T, Hetzel S, Wollaeger J, Anderson S, et al. Bone quality in total shoulder arthroplasty: a prospective study correlating CT Hounsfield units with thumb test and FRAX score. JSES Int 2023;7:628-35. https://doi.org/10.1016/j.jseint.2023.03.012
17. Koo TK, Li MY. A guideline of selecting and reporting intraclass correlation coefficients for reliability research. J Chiropr Med 2016;15:155-63. https://doi.org/10.1016/j.jcm.2016.02.012
18. Kumar S, Sperling JW, Haidukewych GH, Cofield RH. Periprosthetic humeral fractures after shoulder arthroplasty. J Bone Joint Surg Am 2004;86:680-9. https://doi.org/10.2106/00004623-200404000-00003
19. Levin JM, Rodriguez K, Polascik BA, Zeng S, Warren E Jr, Rechenmacher A, et al. Simple preoperative radiographic and computed tomography measurements predict adequate bone quality for stemless total shoulder arthroplasty. J Shoulder Elbow Surg 2022;31:2481-7. https://doi.org/10.1016/j.jse.2022.05.008
20. Luo W, Phung D, Tran T, Gupta S, Rana S, Karmakar C, et al. Guidelines for developing and reporting machine learning predictive models in biomedical research: a multidisciplinary view. J Med Internet Res 2016;18:e323. https://doi.org/10.2196/jmir.5870
21. McGraw KO, Wong SP. Forming inferences about some intraclass correlation coefficients. Psychol Methods 1996;1:30-46.
22. Nagels J, Stokdijk M, Rozing PM. Stress shielding and bone resorption in shoulder arthroplasty. J Shoulder Elbow Surg 2003;12:35-9. https://doi.org/10.1067/mse.2003.22
23. Pauwels R, Jacobs R, Singer SR, Mupparapu M. CBCT-based bone quality assessment: are Hounsfield units applicable? Dentomaxillofac Radiol 2015;44:20140238. https://doi.org/10.1259/dmfr.20140238
24. Pervaiz K, Cabezas A, Downes K, Santoni BG, Frankle MA. Osteoporosis and shoulder osteoarthritis: incidence, risk factors, and surgical implications. J Shoulder Elbow Surg 2013;22:e1-8. https://doi.org/10.1016/j.jse.2012.05.029
25. Raiss P, Edwards TB, Deutsch A, Shah A, Bruckner T, Loew M, et al. Radiographic changes around humeral components in shoulder arthroplasty. J Bone Joint Surg Am 2014;96:e54. https://doi.org/10.2106/JBJS.M.00378
26. Reeves JM, Athwal GS, Johnson JA. An assessment of proximal humerus density with reference to stemless implants. J Shoulder Elbow Surg 2018;27:641-9. https://doi.org/10.1016/j.jse.2017.09.019
27. Reeves JM, Johnson JA, Athwal GS. An analysis of proximal humerus morphology with special interest in stemless shoulder arthroplasty. J Shoulder Elbow Surg 2018;27:650-8. https://doi.org/10.1016/j.jse.2017.10.029
28. Reeves JM, Vanasse T, Roche C, Athwal GS, Johnson JA, Faber KJ, et al. Regional apparent density correlations within the proximal humerus. JSES Int 2021;5:525-31. https://doi.org/10.1016/j.jseint.2020.12.001
29. Reeves JM, Vanasse T, Roche C, Faber KJ, Langohr GDG. Initial assessments of a handheld indentation Probe's correlation with cancellous bone density, stiffness, and strength: an objective alternative to "thumb testing". J Med Dev Trans ASME 2021;15:044502–10. https://doi.org/10.1115/1.4052305.
30. Rodríguez JA, Entezari V, Iannotti JP, Ricchetti ET. Pre-operative planning for reverse shoulder replacement: the surgical benefits and their clinical translation. Annals of Joint 2019;4:4. https://doi.org/10.21037/aoj.2018.12.09
31. Sebro R, De la Garza-Ramos C. Machine learning for opportunistic screening for osteoporosis from CT scans of the wrist and forearm. Diagnostics 2022;12:691. https://doi.org/10.3390/diagnostics12030691
32. Smith ACJ, Tse JJ, Waungana TH, Bott KN, Kuczynski MT, Michalski AS, et al. Internal calibration for opportunistic computed tomography muscle density analysis. PLoS One 2022;17:e0273203. https://doi.org/10.1371/journal.pone.0273203
33. Spross C, Kaestle N, Benninger E, Fornaro J, Erhardt J, Zdravkovic V, et al. Deltoid tuberosity index: a simple radiographic tool to assess local bone quality in proximal humerus fractures. Clin Orthop Relat Res 2015;473:3038-45. https://doi.org/10.1007/s11999-015-4322-x
34. Spross C, Zeledon R, Zdravkovic V, Jost B. How bone quality may influence intraoperative and early postoperative problems after angular stable open reduction-internal fixation of proximal humeral fractures. J Shoulder Elbow Surg 2017;26:1566-72. https://doi.org/10.1016/j.jse.2017.02.026
35. Tingart MJ, Apreleva M, von Stechow D, Zurakowski D, Warner JJ. The cortical thickness of the proximal humeral diaphysis predicts bone mineral density of the proximal humerus. J Bone Joint Surg Br 2003;85:611-7. https://doi.org/10.1302/0301-620x.85b4.12843
36. Winsor C, Li X, Qasim M, Henak CR, Pickhardt PJ, Ploeg H, et al. Evaluation of patient tissue selection methods for deriving equivalent density calibration for femoral bone quantitative CT analyses. Bone 2021;143:115759. https://doi.org/10.1016/j.bone.2020.115759
37. Wirth MA, Rockwood CA Jr. Complications of shoulder arthroplasty. Clin Orthop Relat Res 1994;307:47-69.

Attachment B: Publication V

Citation: Ritter D, Denard PJ, Raiss P, Wijdicks CA, Bachmaier S. A Stemless Anatomic Shoulder Arthroplasty Design Provides Increased Cortical Medial Calcar Bone Loading in Variable Bone Densities Compared to a Short Stem Implant. JSES International 2024. 8(4):851-858. doi.org/10.1016/j.jseint.2024.02.008

JSES International 8 (2024) 851–858

Contents lists available at ScienceDirect

JSES International

journal homepage: www.jsesinternational.org

A stemless anatomic shoulder arthroplasty design provides increased cortical medial calcar bone loading in variable bone densities compared to a short stem implant

Daniel Ritter, MSc[a,b,*], Patrick J. Denard, MD[c], Patric Raiss, MD[d], Coen A. Wijdicks, PhD, MBA[a], Samuel Bachmaier, MSc[a]

[a]*Arthrex Department of Orthopedic Research, Munich, Germany*
[b]*Department of Orthopaedics and Trauma Surgery, Musculoskeletal University Center Munich (MUM), University Hospital, LMU Munich, Munich, Germany*
[c]*Southern Oregon Orthopedics, Medford, OR, USA*
[d]*OCM Clinic, Munich, Germany*

A R T I C L E I N F O

Keywords:
Stemless TSA
Humeral implant micromotion
Medial calcar bone loading
Cortical rim support
Bone density
Biomechanics

Level of evidence: Basic Science Study; Biomechanics

Background: Several studies have reported proximal bone resorption in stemless and press-fit short-stem humeral implants for anatomic total shoulder arthroplasty. The purpose of this biomechanical study was to evaluate implant and cortical bone micromotion of a cortical rim-supported stemless implant compared to a press-fit short stem implant during cyclic loading and static compression testing.
Methods: Thirty cadaveric humeri were assigned to 3 groups based on a previously performed density analysis, adopting the metaphyseal and epiphyseal and inferior supporting bone densities for multivariate analyses. Implant fixation was performed in stemless implant in low bone density (SL-L, n = 10) or short stem implant in low bone density (Stem-L, n = 10) and in stemless implant in high bone density (SL-H, n = 10). Cyclic loading with 220 N, 520 N, and 820 N over 1000 cycles at 1.5 Hz was performed with a constant valley load of 25 N. Optical recording allowed for spatial implant tracking and quantification of cortical bone deformations in the medial calcar bone region. Implant micromotion was measured as rotational and translational displacement. Load-to-failure testing was performed at a rate of 1.5 mm/s with ultimate load and stiffness measured.
Results: The SL-H group demonstrated significantly reduced implant micromotion compared to both low-density groups (SL-L: $P = .014$; Stem-L: $P = .031$). The Stem-L group showed significantly reduced rotational motion and variance in the test results at the 820-N load level compared to the SL-L group (equal variance: $P = .012$). Implant micromotion and reversible bone deformation were significantly affected by increasing load ($P < .001$), metaphyseal cancellous ($P = .023$, $P = .013$), and inferior supporting bone density ($P = .016$, $P = .023$). Absolute cortical bone deformation was significantly increased with stemless implants in lower densities and percentage reversible bone deformation was significantly higher for the SL-H group (21 ± 7%) compared to the Stem-L group (12 ± 6%, $P = .017$).
Conclusion: A cortical rim-supported stemless implant maintained proximally improved dynamic bone loading in variable bone densities compared to a press-fit short stem implant. Biomechanical time-zero implant micromotion in lower bone densities was comparable between short stem and stemless implants at rehabilitation load levels (220 N, 520 N), but with higher cyclic stability and reduced variability for stemmed implantation at daily peak loads (820 N).

Anatomic total shoulder arthroplasty (aTSA) has historically demonstrated acceptable results. In an effort to preserve bone and improve revisability, the humeral component has transitioned towards short-stem and stemless designs. However, bone resorption can occur from unphysiological proximal humeral bone loading. While particularly stemmed and short stem designs have shown

Institutional review board approval was not required for this study.
Investigation performed at the Arthrex Department of Orthopedic Research, Munich, Germany.
*Corresponding author: Daniel Ritter, MSc, Arthrex GmbH Department of Orthopedic Research, Erwin-Hielscher-Strasse 9, Munich 81249, Germany.
E-mail address: publications@arthrex.com (D. Ritter).

https://doi.org/10.1016/j.jseint.2024.02.008

resorptions in the medial calcar region,[14,32,37] similar bone resorptions were found for metaphyseal impacted fin designs ,[1-3,11,19] while a hollow screw design rather reduced the cancellous bone density in the greater tuberosity region.[20,21] While the short-term clinical impact of such stress shielding is minimal,[1,20,21,23,39] potential longer term drawbacks may include survival time, long-term outcomes, bone loss affecting revision, and periprosthetic fracture.[16] The additional influence of low bone mineral density (BMD) also remains unclear in these cases. As stemless implants are increasingly used in a wider range of bone quality, there is substantial interest in objective predictions of stemless implants in aTSA using bone density evaluations in the proximal humerus.[13,22,26]

Biomechanical studies in these settings have mainly focused on primary stability and micromotion measurements, without considering effects on humeral bone loading.[3,10,17] Physiological load transfer patterns in the healthy proximal humerus are complex with respect to specific arm movements and have been shown to vary between poor and normal bone quality, highlighting the importance of cortical load absorption.[18,28,33] Finite element analyses (FEA) of stemless implants have also confirmed the importance of cortical load transfer to increase stability and mimic native humeral loads.[33,34] Cortical loading varies by implant design. For instance, a reduction of medial calcar stress shielding has been reported using a central screw design with cortical rim support that maintains bone loading similar to physiological stresses.[1,2,27] Further experimental investigation of the implant-bone interface, including micromotion and bone deformation analyses, may thus help to better understand the differences in the implant-to-bone load transfer of different implant types.

The purpose of this biomechanical study was to evaluate implant and cortical bone micromotion during cyclic loading and static compression testing of a cortical rim-supported stemless implant compared to an press-fit short stem implant. We hypothesized that a cortical rim-supported stemless design would provide similar stability compared to an impacted short stem implant in variable bone densities but with optimized bone loading in the medial proximal humerus.

Materials and methods

A biomechanical investigation was performed on 30 fresh-frozen cadaveric proximal humeri specimens (68.3 ± 11.5 years; 13 females 17 males) (Science Care Inc., Phoenix, AZ, USA). For all cadavers, there was no sign of degenerative joint disease. The specimens were assigned to low- and high-density groups based on computed tomography (CT) scans and a classification model using the thresholds trained in a previous work.[35] Ten specimens were classified as high bone density and 20 were classified as low bone density. A stemless humeral implant (Eclipse; Arthrex Inc., Naples, FL, USA) was implanted in the stemless implant in high bone density (SL-H, n = 10). The 20 low-density cadavers were randomly assigned to either receive the same stemless implant in low bone density (SL-L, n = 10), or a short stem porous coated press-fit implant (Apex OptiFit Humeral Stem; Arthrex Inc., Naples, FL, USA) (Stem-L, n = 10).

Surgical technique

Specimens were stored at −20° C and thawed overnight at room temperature before tissue preparation and testing. After identifying the humeral neck based on anatomic landmarks the humeral head was resected along the anatomic neck perpendicular to the metaphyseal axis using an oscillating saw and a cutting guide. For stemless implantation the proximal humerus was measured, and a cortical rim-supported trunnion was placed followed by compression with a hollow cage screw along the metaphyseal axis according to the manufacturer's recommendations. Cortical rim support at the medial calcar was ensured by sizing the trunnion to the outer rim of the humeral head cut. Short stem cementless press-fit implantation was performed by broaching the humeral canal according to the manufacturer's recommendations.

Bone density

Bone density parameters were adopted from a previous study, with humeral bones scanned by a standard clinical CT (Siemens SOMATOM Definition AS+; Siemens Healthcare GmbH, Erlangen, Germany) with a voxel resolution of 0.6 × 0.6 × 0.6 mm. Standard calibration according to the manufacturer's protocol using density phantoms [0; 200 mgHA/cm^3] was performed to allow conversion of gray scale values to BMD (mgHA/cm^3) as well as to ensure consistency between CT scans. All CT voxel data were imported as a 4-dimensional point cloud (ie [x, y, z, mgHA/cm^3]) and the slices were initially oriented parallel to the anatomical neck for region of interest analysis. Evaluation using a custom image processing script (MathWorks, Natick, MA, USA) allowed for the adoption of the following parameters for previously described stemless aTSA classification (Fig. 1).[35]

Biomechanical testing

Based on prior biomechanical studies, 3 load steps were applied, loading to 220 N, 520 N, and 820 N.[6,7,10,17,41] The lower load level (220 N) was applied to simulate 20% body weight (196 N) for rehabilitation arm movements measured by a telemetric shoulder implant.[6] The middle load step (520 N) simulated loads during the first 2 months of physiotherapy after shoulder arthroplasty, representing 40% body weight (392 N) during training against resistance.[6] Peak loads during "normal" use with no weight in the hand were simulated by the upper load block (820 N) as the worst case scenario during rehabilitation. Loads were applied in the coronal plane at an angle of 30° from the central axis of the implant, as demonstrated by in vivo measurements.[7,41] Loads were applied cyclically to the humeral head using a custom-made polyethylene (PE) stamp with the respectively sized PE glenoid curvature to simulate contact pressure for 1000 cycles per load block in force control mode at 1.5 Hz (Fig. 2, *A*). Loads were applied using a single axis material testing machine (ElectroPuls E3000; Instron, Norwood, MA, USA) to investigate micromotion and bone deformation at the steady states within the last cycle of each load block using an optical tracking system (Fig. 2, *B*). Additional static loading was performed at a rate of 1.5 mm/s after cyclic loading. Mechanical data were recorded continuously with a sampling rate of 500 Hz. All tests were performed at room temperature and the tissue was kept moist with physiological saline solution throughout preparation and testing.

Implant—bone interface analysis

Micromotion of the implant in reference to the bone and bone deformation was recorded using an optical tracking system (Carl Zeiss GOM Metrology GmbH, Braunschweig, Germany). Tracking points (diameter 0.8 mm) were fixed on the embedding, bone, implant, and actuator, respectively allowing for rigid body motion correction in reference to the fixed embedding. The systems' use of 2 cameras allowed for spatial point cloud tracking with a mean deviation of 5.4 ± 2.8 μm. Tracking of the point clouds attached along the cortical margin 2 mms below the resection plane allowed for measurement of the cortical superficial bone deformation. The separation in relative implant and bone motion was achieved by the application of different coordinate systems for each component applied in the optical tracking system. Images were either

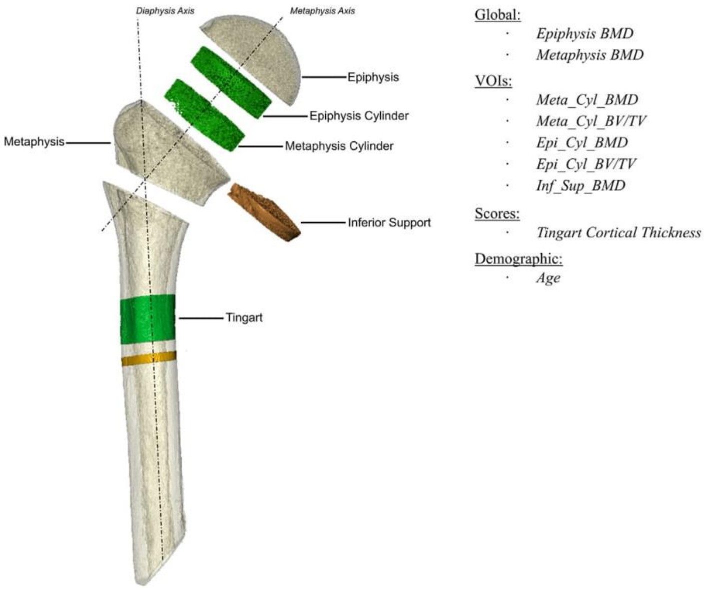

Figure 1 Adopted bone density variables from a previous work.
(Reprinted from Ritter et al[35]) © 2024 Journal of Shoulder and Elbow Surgery Board of Trustees. *BMD*, bone mineral density; *BV/TV*, bone volume/total volume.

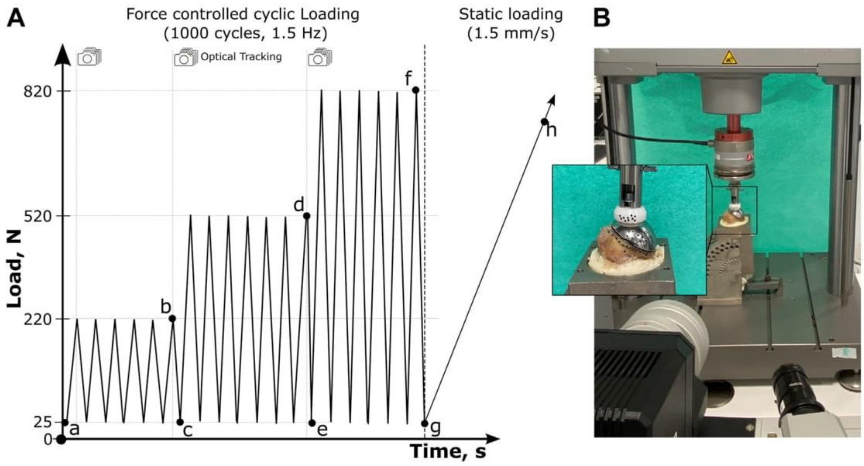

Figure 2 (**A**) Testing protocol and (**B**) experimental cyclic loading and static loading setup including the camera setup and tracking points. Points of data analysis included total cyclic deformation measurements (s_{tot}, Δab, Δad, and Δaf) at the end of each load block. During the final hysteresis in each loading block using the tracking points, micromotion (Δbs, Δde, and Δfg) was evaluated and further divided into the motion of the implant ($s_{Implant}$, $\alpha_{Implant}$) and compressive transmission caused deformation of the bone (s_{Bone}). Ultimate load and stiffness were analyzed during final static compression testing (F_{max}, D_{UF}; Δgh).

compared to the time-zero reference state or evaluated during applied load hystereses (Fig. 3). Optical measurements were taken at a sampling rate of 30 Hz.

Outcome data

Metrics for comparison included data from cyclic loading and static compression testing. Cyclic outcome variables included the total construct displacement (s_{tot}) at the end of each loading block (220 N, 520 N, and 820 N). At the same time, micromotion during one loading hysteresis (Fig. 3) additionally provided relative information about implant micromotion ($s_{Implant}$, $\alpha_{Implant}$) and compression-induced superficial deformation of the medial calcar cortical bone (s_{Bone}). To further investigate the load absorption capability of the bone, the measured superficial cortical deformation was related to the total displacement as a percentage. The

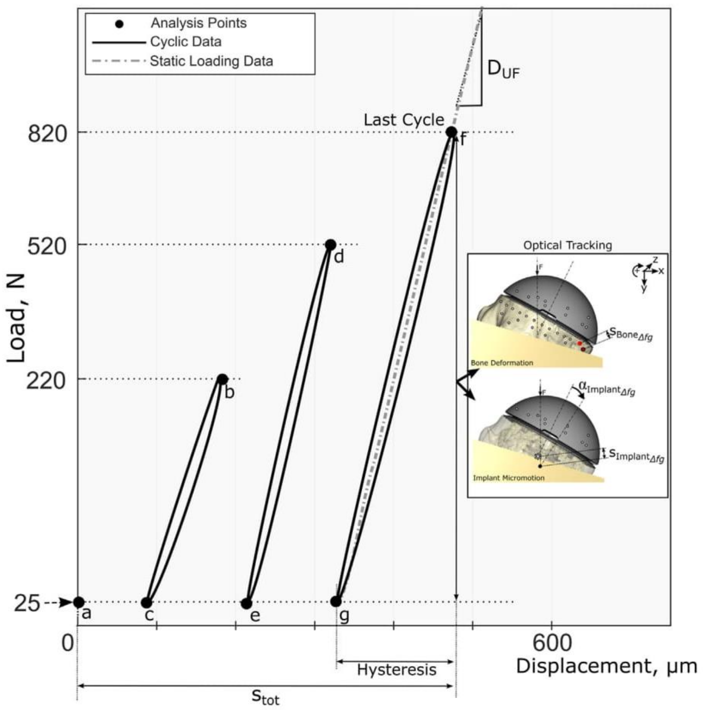

Figure 3 Schematic illustration of representative load-displacement curves at the end of each load block for total deformation measurement (s_{tot}) including optical tracking for micromotion analysis during reversible hysteresis loading dividing up in implant motion ($s_{Implant}$, $\alpha_{Implant}$) and bone deformation (s_{Bone}). Ultimate load and stiffness (D_{UF}) were analyzed during static compression testing.

ultimate load (F_{max}) was defined directly after the elastic progression where the linear stiffness (D_{UF}) was determined during the static compression test. Data analysis was performed with commercial software (Matlab version R2019a; MathWorks, Natick, MA, USA).

Statistical analysis

Biomechanical testing outcome metrics were the dependent primary outcome variables. Bone density variables were defined as secondary outcome variables and were used as covariates in multivariable regression analyses. Statistical analysis was performed using commercial software (Sigma Plot Statistics for Windows, version 13.0; Systat Software, San Jose, CA, USA).

The statistical analysis included a 1-way analysis of variance with a Holm-Sidak post hoc test performed for a significant pairwise analysis of primary outcome variables. Significance was defined as $P \leq .05$ and the desired power level was set at 0.8. Post hoc power analysis was performed to confirm adequate sample size. The Shapiro–Wilk test and Brown–Forsythe test were used to confirm each data set followed a normal distribution and equal variance, respectively. A nonparametric test (Kruskal–Wallis) was used for data sets that failed these tests. For Kruskal–Wallis tests that found significance, a post hoc test acc. to Dunn's method was conducted to further analyze the differences. The observed post hoc average power values of all 1-way analysis of variance tests were higher than the desired power level of 0.8 leading us to conclude that our sample size was sufficient.

A 1-way analysis of covariance for multivariable regression analysis including the adopted density variables [35] was performed to quantify interactions and compare the groups with each other. For analysis of covariance tests that were considered significant in an equal slope model, a Holm Sidak post hoc test was performed for pairwise analysis. Significance was defined as $P \leq .05$ and the desired power level was set at 0.8. The Shapiro–Wilk and Levene tests were used to confirm each data set followed a normal distribution and homogeneity in variance, respectively.

Results

Bone density variables are summarized in Table I.

Cyclic testing

Cyclic displacement was lowest in the SL-H group (Fig. 4). At the highest load level, the SL-L group showed significantly increased total displacement (436 ± 172 µm) compared to the Stem-L (370 ± 90 µm, $P = .003$) and SL-H (226 ± 92 µm, $P = 02$) groups, which were also significantly different ($P = .044$).

Absolute bone deformation was significantly increased for the SL-L group (520 N: 39 ± 10 µm; 820 N: 64 ± 22 µm) compared to the stemmed implant (520 N: 22 ± 13 µm; 820 N: 38 ± 23 µm) in the 520 N and 820 N load blocks (Fig. 5). The percentage of reversible bone deformation for the SL-H group (21 ± 7%, $P = .017$) was significantly higher at all load levels compared to the Stem-L group (12 ± 6%). SL-L maintained a percentual bone deformation of

Table I
Mean values with standard deviations of the density variables (BMD: Bone Mineral Density; BV/TV: Bone Volume/Total Volume) for specimens assigned to the stemless or stemmed group including statistical analysis.

	SL-L	SL-H	Stem-L	SL-L vs. SL-H	Stem-L vs. SL-H	Stem-L vs. SL-L
				P value	*P* value	*P* value
Epiphysis BMD [mgHA/cm^3]	324 ± 43	412 ± 31	332 ± 31	***<.001***	***<.001***	*.831*
Metaphysis BMD [mgHA/cm^3]	343 ± 37	410 ± 35	354 ± 34	***.003***	***.002***	*.759*
Epiphysis Cylinder BMD [mgHA/cm^3]	282 ± 24	323 ± 17	280 ± 23	***<.001***	***<.001***	*.123*
Epiphysis Cylinder BV/TV	0.38 ± 0.21	0.44 ± 0.20	0.37 ± 0.19	***.007***	***.011***	*.970*
Metaphysis Cylinder BMD [mgHA/cm^3]	260 ± 9	297 ± 14	265 ± 12	***.003***	***.002***	*.662*
Metaphysis Cylinder BV/TV	0.20 ± 0.11	0.33 ± 0.11	0.19 ± 0.11	***.001***	***.004***	*.927*
Inferior Support BMD [mgHA/cm^3]	333 ± 38	412 ± 31	351 ± 35	***<.001***	***.001***	*.480*
Tingart Cortical Thickness [mm]	3.1 ± 0.4	3.6 ± 0.4	3.1 ± 0.4	***.005***	***.009***	*.939*
Age [y]	73.1 ± 9.4	60.7 ± 9.5	72.2 ± 11.6	***.021***	***.029***	*.977*

SL-L, stemless implant in low bone density; *SL-H*, stemless implant in high bone density; *Stem-L*, short stem implant in low bone density; *BMD*, bone mineral density; *BV/TV*, bone volume/total volume.
Italic bold = significant ($P < .05$) and italic = not significant ($P > .05$).

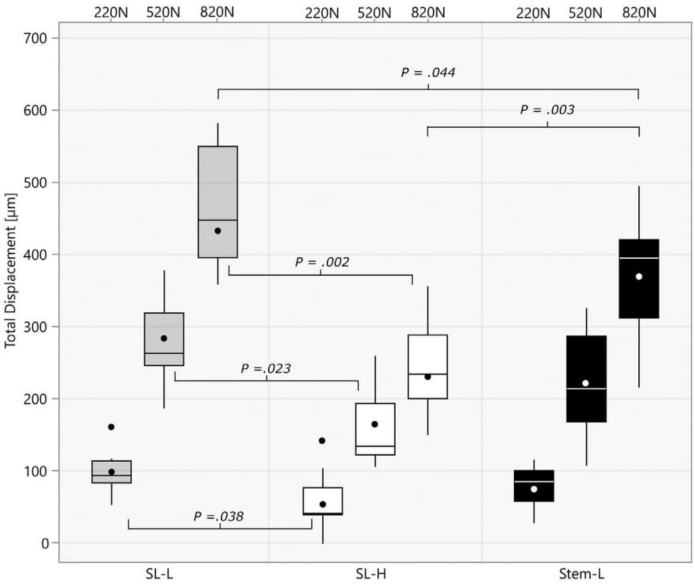

Figure 4 Boxplot with mean and median overall cyclic displacement at the end of the cyclic loading blocks (220 N, 520 N, and 820 N). *SL-L*, stemless implant in low bone density; *SL-H*, stemless implant in high bone density; *Stem-L*, short stem implant in low bone density.

19 ± 7% without significant differences to the SL-H (P = .110) and Stem-L group (P = .669).

Significantly increased implant micromotion (Fig. 6, *A*) occurred at the highest load level in the lower bone density groups (SL-L 232 µm (confidence interval [CI]95:98-341 µm), P = .015 and Stem-L 221 µm (CI95:118-244 µm), P = .038) compared to the SL-H group (122 µm (CI95:93-236 µm)). The SL-H and Stem-L groups showed significantly reduced rotational motion (Fig. 6, *B*) at the 820-N load level compared to the SL-L group (Equal variance: P = .012) with lower variance in the test results for the Stem-L group.

Covariance with bone densities

Implant micromotion interacted significantly with the increasing load (P < .001), metaphyseal cancellous bone density (P = .023), and inferior supporting bone density (P = .016). Implant micromotion was significantly reduced in the SL-H group compared to both low-density groups (SL-L: P = .014; Stem-L: P = .031), which were not significantly different (P = .274).

Bone deformation significantly interacted with increasing load (P < .001), cancellous epiphyseal (P = .019) and metaphyseal bone density (P = .013), and inferior supporting bone density (P = .023). The SL-L group showed significantly more bone deformation than the Stem-L group (P = .021).

Static loading

All constructs reached the regular test end and were statically loaded. The linear stiffness of the stem group (1328 ± 282 N/mm) was significantly decreased compared to stemless groups in high (1641 ± 285 N/mm, P = .026) and low bone densities (1623 ± 246 N/mm, P = .046), which did not differ significantly to each other (P = .680). The ultimate loads did not differ significantly between the groups (P = .330) with a mean load of 2506 ± 298 N.

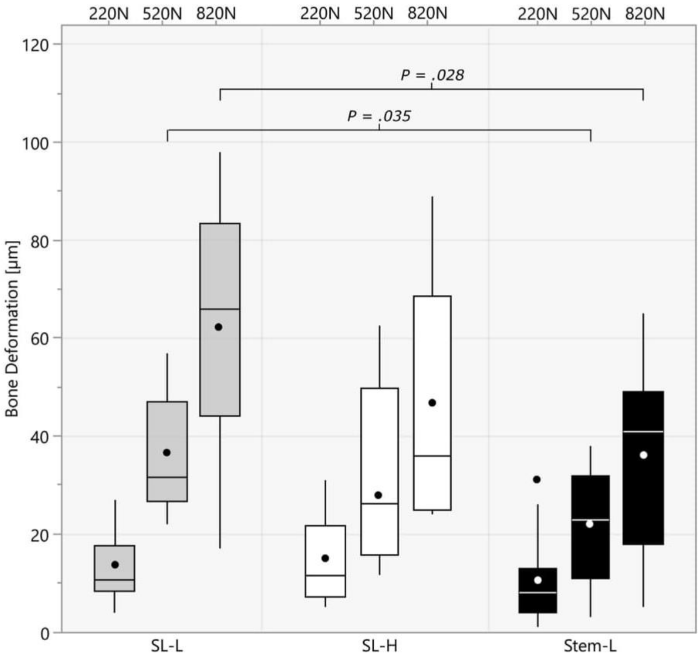

Figure 5 Boxplot with mean and median bone deformations during hysteresis loading at the end of each cyclic loading block (220 N, 520 N, and 820 N). *SL-L*, stemless implant in low bone density; *SL-H*, stemless implant in high bone density; *Stem-L*, short stem implant in low bone density.

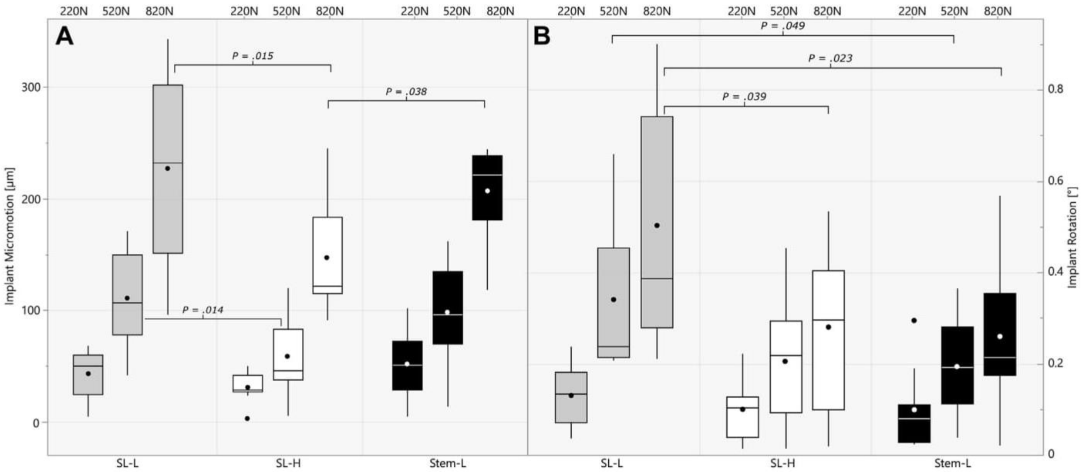

Figure 6 Boxplot of implant translational (**A**) and rotational (**B**) motion during the load hystereses at the end of each cyclic loading block (220 N, 520 N, and 820 N). *SL-L*, stemless implant in low bone density; *SL-H*, stemless implant in high bone density; *Stem-L*, short stem implant in low bone density.

Discussion

The most important finding of this study was that implant–bone compression of a cortical rim-supported stemless implant resulted in increased bone loading at the medial cortex of the proximal humerus, while the press-fit stemmed implant demonstrated improved cyclic rotational and translational stability in low bone density compared to the stemless implant. These outcomes were found to be significantly affected by the amount of loading and the bone density. Significantly increased primary implant stability was found for stemless implants in higher bone densities with the proximal humeral bone providing a reversible load absorption pattern. Various biomechanical studies of primary implant stability testing are available, but in the current study we additionally investigated humeral implant–bone loading including the assessment of systematically mapped humeral bone densities. Although the in vivo biological effects cannot be reproduced biomechanically such as the effects of bone ingrowth (secondary fixation), stress shielding, and PE wear, this study showed significant differences between current implant types affected by varying bone densities. The experimental findings resulting from investigated superficial cortical bone micromotions caused by different load transfer patterns in the humerus may bridge the gap between FEA simulations and clinical findings.

The behavior of autologous bone is closely linked to the mechanical environment in which osseointegration is intended. Differently maintained mechanical bone stimuli have been reported to have a significant effect on bone restoration, particularly during the proliferative phase of bone healing.[4,5,38] For arthroplasty, micromotions below 150 μm have been reported as the critical threshold for osseointegration with porous-coated implant surfaces.[17,29,30] Within the rehabilitation relevant load levels (220 N, 520 N) the micromotions of all implants were below 150 μm regardless of the cadaveric humeral bone density. While the stemless implant withstood the time-zero 820-N load in higher bone densities, a too-aggressive rehabilitation protocol in lower bone densities may result in significantly increased micromotions (>150 μm) that may prevent bone ingrowth.[3,10,17] Similarly, a biomechanical study using density separation at a BMD of <0.35 g/cm^2 recommended stemmed implants in poorer bone quality for improved stability, except the cortical rim supporting stemless implant may be usable in a wider range of bone densities.[10] The aforementioned stemless implant maintained a homogeneous load transfer to the metaphyseal bone in our study and provided a higher linear stiffness in low and high bone densities under static loading compared to the impacted short-stem implant, confirming a sufficient primary fixation stability and therefore implantability of the implant also in lower bone densities. However, the effect of the implant design on implant stability, implant-bone osseointegration and stress shielding after the time-zero setting can be impaired by various other biological factors influencing trabecular bone formation or resorption[14,32,36,37]

While anatomic stemless implantation is generally considered to be stable, the complication rates remain increased in patients with poor bone density.[9] Therefore, preoperative identification of a patient with low bone density may have implications for the treatment approach. The inferior supporting and metaphyseal peri-implant density parameters showed the highest interaction to affect implant stability and bone deformation patterns in this work. Preoperative bone quality assessment may pay off to offer better preoperative knowledge in the surgeons' decision process.[13,22,26,35]

The increased reversible bone deformation observed in our study suggests that a load transfer is maintained in the medial calcar region which may account for the reduced bone resorption in this area observed clinically with a cortical rim support design.[1,2] Recent FE analyses similarly showed a cortical based load transmission through the stemless trunnion supporting implant, mimicking the physiological load pattern in the native humerus.[33,34] Bone load, load frequency and incidence lead to positive bone adaptions in these cases, even though the influences of secondary anchorage due to bone osteointegration at the back of the Calcium Phosphate coated trunnion may influence these findings.[42] Humeral implants without cortical support or more distal load transmission patterns showed bony resorption in impacted stemless and stemmed TSAs respectively.[1,2,25,40] Our findings similarly indicate that the primary stability and bone loading of humeral implants are highly correlated to the design of the device and the respective load transmission at the resection plane. Even though no effects of the bony adaptions on the clinical outcome scores were determined in short-term clinical studies,[1,20,21,23,39] it may affect long-term results, rates of revision cases and periprosthetic fractures.[9,16] Improvements in stress shielding are affirmed by clinical [8,21,24,39] and FEA studies when approximating humeral bone stresses,[12,33,34] although different implant designs seem to have a relevant impact on the bone adaption process. Cortical rim support was shown to decrease the bone density in the cancellous greater tuberosity area, wherefore a cortically supporting design in short stem implants potentially would negatively affect the humeral fixation.[20] Bone loading effects in the metaphyseal cancellous bone were not investigated in this study but may be significantly affected by the use of a cancellous or cortical supporting design. Our study experimentally showed similar behavior of the investigated implants in terms of bone loading and primary implant stability compared to in-silico studies.[12,31,33] Limited activation in either cancellous greater tuberosity or cortical medial calcar areas during the proliferative phase of bone remodeling is associated with reduced mechanical bone stimuli.[15,16] The use of cortically supporting stemless designs may result in improved cortical load transmission and reduced bone resorption at the cortical medial calcar region.

Limitations

We acknowledge some limitations to the current study. Bony ingrowth, which provides secondary anchorage in clinical applications, could not be accounted for in cadaveric biomechanical testing. The stability as well as the load transfer of the investigated implants may behave differently in an in vivo setting over a longer follow-up period. Biological effects and the ability of different implant designs to promote bone ingrowth due to bone loading and implant coatings is a pertinent question that is also beyond the scope of this study. Nevertheless, the findings of this work determined the primary stability of stemless and stemmed implants before bone ingrowth and provided insight into load transfer in an experimental biomechanical study. These findings are important to understand potential causes for stress shielding and implant micromotion which influence postoperative bony integration. Axial compression load was applied in a fixed angle to simulate compressive loading of the humeral head. Bone loading resulting from variable in vivo shoulder joint loading, including rotational and shear forces, may result in different in vivo bone deformations. Thus, the current test methodology is only a rough simulation of the in vivo loading environment and the obtained functional performance could differ from clinical device behavior. Our findings are limited to a stemless cortical rim-supported with screw compression implant and short stem implant. To extend the understanding of different types of bony resorptions, further implants with differing cortical rim support should be investigated with extending the focus from cortical superficial to cancellous observations below the resection plane. Although there is no evidence of bony adaption following stemless reverse shoulder arthroplasty, this approach may also provide important information that will be crucial when testing reverse arthroplasty implant designs.

Conclusion

A cortical rim-supported stemless implant maintained proximally improved dynamic bone loading in variable bone densities compared to a press-fit short stem implant. Biomechanical time-zero implant micromotion in lower bone densities was comparable between short stem and stemless implants at rehabilitation load levels (220 N, 520 N), but with higher cyclic stability and reduced variability for stemmed implantation at daily peak loads (820 N).

Disclaimers:

Funding: Arthrex provided full support of this study.
Conflicts of interest: Daniel Ritter is an employee of Arthrex. Patrick J. Denard receives consulting fees and honoraria from Arthrex, receives support for travel to meetings for the study or other purposes from Arthrex, and receives royalties from Arthrex. Patric Raiss receives consulting fees and honoraria from Arthrex, receives support for travel to meetings for the study or other purposes from Arthrex. Coen A. Wijdicks is an employee of Arthrex. Samuel Bachmaier is an employee of Arthrex. All the other authors, their immediate families, and any research foundations with which they are affiliated have not received any financial payments or other benefits from any commercial entity related to the subject of this article.

References

1. Aibinder WR, Uddin F, Bicknell RT, Krupp R, Scheibel M, Athwal GS. Stress shielding following stemless anatomic total shoulder arthroplasty. Shoulder Elbow 2023;15:54-60. https://doi.org/10.1177/17585732211058804.
2. Alikhah A, Imiolczyk JP, Krukenberg A, Scheibel M. Screw fixation in stemless shoulder arthroplasty for the treatment of primary osteoarthritis leads to less osteolysis when compared to impaction fixation. BMC Musculoskelet Disord 2020;21:295. https://doi.org/10.1186/s12891-020-03277-3.
3. Bachmaier S, Flury M, Lichtenberg S, Schwyzer H-K, Anderl W, Denard PJ, et al. Postpreparation peri-implant humeral bone density and fixation strength vary based on design in stemless reverse shoulder arthroplasty. Semin Arthroplasty JSES 2021;31:677-87. https://doi.org/10.1053/j.sart.2021.04.005.
4. Bailón-Plaza A, Marjolein CH. Beneficial effects of moderate, early loading and adverse effects of delayed or excessive loading on bone healing. J Biomech 2003;36:1069-77. https://doi.org/10.1016/S0021-9290(03)00117-9.
5. Barcik J, Epari DR. Can optimizing the mechanical environment deliver a clinically significant reduction in fracture healing time? Biomedicines 2021;9:691. https://doi.org/10.3390/biomedicines9060691.
6. Bergmann G, Graichen F, Bender A, Kaab M, Rohlmann A, Westerhoff P. In vivo glenohumeral contact forces–measurements in the first patient 7 months postoperatively. J Biomech 2007;40:2139-49. https://doi.org/10.1016/j.jbiomech.2006.10.037.
7. Bergmann G, Graichen F, Bender A, Rohlmann A, Halder A, Beier A, et al. In vivo gleno-humeral joint loads during forward flexion and abduction. J Biomech 2011;44:1543-52. https://doi.org/10.1016/j.jbiomech.2011.02.142.
8. Berth A, Marz V, Wissel H, Awiszus F, Amthauer H, Lohmann CH. SPECT/CT demonstrates the osseointegrative response of a stemless shoulder prosthesis. J Shoulder Elbow Surg 2016;25:e96-103. https://doi.org/10.1016/j.jse.2015.09.009.
9. Casp AJ, Montgomery SRJ, Cancienne JM, Brockmeier SF, Werner BC. Osteoporosis and implant-related complications after anatomic and reverse Total Shoulder Arthroplasty. J Am Acad Orthop Surg 2020;28:121-7. https://doi.org/10.5435/jaaos-d-18-00537.
10. Chen RE, Knapp E, Qiu B, Miniaci A, Awad HA, Voloshin I. Biomechanical comparison of stemless humeral components in total shoulder arthroplasty. Semin Arthroplasty JSES 2022;32:145-53. https://doi.org/10.1053/j.sart.2021.08.003.
11. Churchill RS. Stemless shoulder arthroplasty: current status. J Shoulder Elbow Surg 2014;23:1409-14. https://doi.org/10.1016/j.jse.2014.05.005.
12. Comenda M, Quental C, Folgado J, Sarmento M, Monteiro J. Bone adaptation impact of stemless shoulder implants: a computational analysis. J Shoulder Elbow Surg 2019;28:1886-96. https://doi.org/10.1016/j.jse.2019.03.007.
13. Cronin KJ, Vaughan A, Tzeuton S, Abboud JA. Prospective assessment of osteoporosis in total shoulder arthroplasty. Semin Arthroplasty JSES 2023;33:15-21. https://doi.org/10.1053/j.sart.2022.07.015.
14. Denard PJ, Noyes MP, Walker JB, Shishani Y, Gobezie R, Romeo AA, et al. Proximal stress shielding is decreased with a short stem compared with a traditional-length stem in total shoulder arthroplasty. J Shoulder Elbow Surg 2018;27:53-8. https://doi.org/10.1016/j.jse.2017.06.042.
15. Denard PJ, Raiss P, Gobezie R, Edwards TB, Lederman E. Stress shielding of the humerus in press-fit anatomic shoulder arthroplasty: review and recommendations for evaluation. J Shoulder Elbow Surg 2018;27:1139-47. https://doi.org/10.1016/j.jse.2017.12.020.
16. DeVito P, Judd H, Malarkey A, Elson L, McNeely E, Berglund D, et al. Medial calcar bone resorption after anatomic total shoulder arthroplasty: does it affect outcomes? J Shoulder Elbow Surg 2019;28:2128-38. https://doi.org/10.1016/j.jse.2019.03.017.
17. Favre P, Seebeck J, Thistlethwaite PA, Obrist M, Steffens JG, Hopkins AR, et al. In vitro initial stability of a stemless humeral implant. Clin Biomech 2016;32:113-7. https://doi.org/10.1016/j.clinbiomech.2015.12.004.
18. Filardi V. Stress distribution in the humerus during elevation of the arm and external abduction. J Orthop 2020;19:218-22. https://doi.org/10.1016/j.jor.2020.02.003.
19. Greis M, Heubach K, Hoberg M, Irlenbusch U. Proximal humeral bone loss in stemless shoulder arthroplasty: potential factors influencing bone loss and a new classification system. Arch Orthop Trauma Surg 2022;143:3085-90. https://doi.org/10.1007/s00402-022-04493-3.
20. Habermeyer P, Lichtenberg S, Tauber M, Magosch P. Midterm results of stemless shoulder arthroplasty: a prospective study. J Shoulder Elbow Surg 2015;24:1463-72. https://doi.org/10.1016/j.jse.2015.02.023.
21. Hawi N, Magosch P, Tauber M, Lichtenberg S, Habermeyer P. Nine-year outcome after anatomic stemless shoulder prosthesis: clinical and radiologic results. J Shoulder Elbow Surg 2017;26:1609-15. https://doi.org/10.1016/j.jse.2017.02.017.
22. Hayden A, Cotter EJ, Hennick T, Hetzel S, Wollaeger J, Anderson S, et al. Bone quality in total shoulder arthroplasty: a prospective study correlating CT hounsfield units with thumb test and FRAX score. JSES Int 2023;7:628-35. https://doi.org/10.1016/j.jseint.2023.03.012.
23. Heuberer PR, Brandl G, Pauzenberger L, Laky B, Kriegleder B, Anderl W. Radiological changes do not influence clinical mid-term outcome in stemless humeral head replacements with hollow screw fixation: a prospective radiological and clinical evaluation. BMC Musculoskelet Disord 2018;19:28. https://doi.org/10.1186/s12891-018-1945-6.
24. Huguet D, DeClercq G, Rio B, Teissier J, Zipoli B, Group T. Results of a new stemless shoulder prosthesis: radiologic proof of maintained fixation and stability after a minimum of three years' follow-up. J Shoulder Elbow Surg 2010;19:847-52. https://doi.org/10.1016/j.jse.2009.12.009.
25. Imiolczyk JP, Krukenberg A, Mansat P, Bartsch S, McBirnie J, Gotterbarm T, et al. Midterm results of stemless impaction shoulder arthroplasty for primary osteoarthritis: a prospective, multicenter study. JSES Int 2023;7:1-9. https://doi.org/10.1016/j.jseint.2022.09.001.
26. Levin JM, Rodriguez K, Polascik BA, Zeng S, Warren E Jr, Rechenmacher A, et al. Simple preoperative radiographic and computed tomography measurements predict adequate bone quality for stemless total shoulder arthroplasty. J Shoulder Elbow Surg 2022;31:2481-7. https://doi.org/10.1016/j.jse.2022.05.008.
27. Magosch P, Habermeyer P, Bachmaier S, Metcalfe N. Biomechanische Grundlagen des metaphysär verankerten Humeruskopfersatzes. Obere Extremität 2012;7:11-6. https://doi.org/10.1007/s11678-011-0150-0.
28. Maldonado ZM, Seebeck J, Heller MO, Brandt D, Hepp P, Lill H, et al. Straining of the intact and fractured proximal humerus under physiological-like loading. J Biomech 2003;36:1865-73. https://doi.org/10.1016/s0021-9290(03)00212-4.
29. Peppers T. Fixation of humeral prostheses and axial micromotion. J Shoulder Elbow Surg 1998;7:414-8.
30. Pilliar RM, Lee JM, Maniatopoulos C. Observations on the effect of movement on bone ingrowth into porous-surfaced implants. Clin Orthop Relat Res 1986;208:108-13.
31. Quental C, Folgado J, Fernandes PR, Monteiro J. Bone remodelling analysis of the humerus after a shoulder arthroplasty. Med Eng Phys 2012;34:1132-8. https://doi.org/10.1016/j.medengphy.2011.12.001.
32. Raiss P, Edwards TB, Deutsch A, Shah A, Bruckner T, Loew M, et al. Radiographic changes around humeral components in shoulder arthroplasty. J Bone Joint Surg Am 2014;96:e54. https://doi.org/10.2106/JBJS.M.00378.
33. Razfar N, Reeves JM, Langohr DG, Willing R, Athwal GS, Johnson JA. Comparison of proximal humeral bone stresses between stemless, short stem, and standard stem length: a finite element analysis. J Shoulder Elbow Surg 2016;25:1076-83. https://doi.org/10.1016/j.jse.2015.11.011.
34. Reeves JM, Langohr GDG, Athwal GS, Johnson JA. The effect of stemless humeral component fixation feature design on bone stress and strain response: a finite element analysis. J Shoulder Elbow Surg 2018;27:2232-41. https://doi.org/10.1016/j.jse.2018.06.002.
35. Ritter D, Denard PJ, Raiss P, Wijdicks CA, Bachmaier S. Preoperative 3D computed tomography bone density measures provide objective bone quality classifications for stemless anatomic total shoulder arthroplasty. J Shoulder Elbow Surg 2024. https://doi.org/10.1016/j.jse.2023.11.005.
36. Sandberg OH, Aspenberg P. Inter-trabecular bone formation: a specific mechanism for healing of cancellous bone. Acta Orthop 2016;87:459-65. https://doi.org/10.1080/17453674.2016.1205172.
37. Schnetzke M, Coda S, Raiss P, Walch G, Loew M. Radiologic bone adaptations on a cementless short-stem shoulder prosthesis. J Shoulder Elbow Surg 2016;25:650-7. https://doi.org/10.1016/j.jse.2015.08.044.
38. Ulstrup AK. Biomechanical concepts of fracture healing in weight-bearing long bones. Acta Orthop Belg 2008;74:291-302.
39. Uschok S, Magosch P, Moe M, Lichtenberg S, Habermeyer P. Is the stemless humeral head replacement clinically and radiographically a secure equivalent to standard stem humeral head replacement in the long-term follow-up? A prospective randomized trial. J Shoulder Elbow Surg 2017;26:225-32. https://doi.org/10.1016/j.jse.2016.09.001.
40. Vegas A, Cannon D, Lewis S, Glener J, Mekkawy KL, Rodriguez HC, et al. Impact of humeral stem length on calcar resorption in anatomic total shoulder arthroplasty. J Shoulder Elbow Surg 2023;33:130-8. https://doi.org/10.1016/j.jse.2023.05.033.
41. Westerhoff P, Graichen F, Bender A, Halder A, Beier A, Rohlmann A, et al. In vivo measurement of shoulder joint loads during activities of daily living. J Biomech 2009;42:1840-9. https://doi.org/10.1016/j.jbiomech.2009.05.035.
42. Wolff J. Das Gesetz der Transformation der Knochen. Dtsch Med Wochenschr 1893;19:1222-4. https://doi.org/10.1055/s-0028-1144106.

CV

Daniel Ritter

University Degrees

04/2022 - today	Dr. rer. biol. hum. Klinik für Orthopädie und Unfallchirurgie, Muskuloskelettales Universitätszentrum München (MUM), Klinikum der Universität München, LMU München
03/2018 – 01/2020	Master of Science Applied Research in Engineering Sciences Hochschule München
10/2014 – 02/2018	Bachelor of Science Industrial MedTec Hochschule Furtwangen University – Campus Tuttlingen

Professional Experience

02/2021 – today	Research Engineer: Arthrex GmbH, München Orthopedic Research
09/2020 – 01/2021	Engineer for patient-specific implants: Implantcast GmbH, Buxtehude Customized-fit 3D
03/2019 – 12/2019	Master Thesis: Arthrex GmbH, München Orthopedic Research Title: Primary Fixation Stability of Reverse Stemless Shoulder Prostheses
07/2017 – 01/2018	Bachelor Thesis: Arthrex GmbH, München Research Title: Dynamic Safety Belt Concept for Internal Bracing and ACL Repair
04/2016 – 09/2016	Internship: Stryker, Freiburg Biomechanical Laboratory